

Non-perturbative renormalization on the lattice

Dissertation

zur Erlangung des akademischen Grades
doctor rerum naturalium (Dr. rer. nat.)

vorgelegt dem Rat der Physikalisch-Astronomischen Fakultät
der Friedrich-Schiller-Universität Jena

von Dipl.-Phys. Daniel Körner
geboren am 10.03.1985 in Naumburg (Saale)

Gutachter:

1. Prof. Dr. habil. Andreas Wipf,
Friedrich-Schiller-Universität Jena
2. Prof. Dr. Urs Wenger,
Universität Bern
3. Prof. Dr. habil. Gernot Münster,
Westfälische Wilhelms-Universität Münster

Tag der Disputation: 28.08.2014

Nicht-perturbative Renormierung auf dem Gitter

Zusammenfassung

Stark wechselwirkende Theorien bilden das Herz der Elementarteilchenphysik. Ihr komplexes Verhalten bestimmt unsere Welt *sui generis*. Von besonderem Interesse sind Gittersimulationen supersymmetrischer Theorien. Jede Diskretisierung der Raumzeit bricht Supersymmetrie und erlaubt so die Renormierung relevanter, susy-brechender Operatoren. Zum Verständnis des Verhaltens solcher Operatoren studieren wir den Renormierungsgruppenfluss des nichtlinearen $O(N)$ Sigma Modells (NLSM). Es wird vermutet, dass es, ähnlich zur Quantengravitation, asymptotisch sicher ist. Das Flussdiagramm wird durch eine Kombination der Dämon Methode mit Blockspin Transformationen berechnet. Essentiell ist hierbei eine gründliche Behandlung von Trunkierungsfehlern. In zwei Dimensionen bestätigen wir asymptotische Freiheit und in drei Dimensionen kann asymptotische Sicherheit demonstriert werden. Wir fahren mit einer Gittersimulation des supersymmetrischen $O(3)$ NLSM fort. Anhand einer außergewöhnlichen Diskretisierung, die nur die Feineinstellung eines einzigen Operators erfordert, argumentieren wir, dass der Kontinuumsimes des Modells erfolgreich durchgeführt werden kann. Allerdings wird die Anwendbarkeit von Monte Carlo Methoden durch ein Vorzeichenproblem in Frage gestellt. Daher ist das letzte Kapitel der Fermion-bag Methode gewidmet. Wir stellen fest, dass Fluktuationen des Vorzeichens im susy NLSM hiermit deutlich seltener auftreten. Eine ergänzende Darstellung stellt das ein-flavor Gross-Neveu Modell bereit, das ein Problem der komplexen Phase aufweist. Leider fluktuiert die Phase im Fall von Wilson Fermionen nur gering und eine endgültige Schlussfolgerung bezüglich der Wirksamkeit des Fermion-bag Ansatzes kann nicht erfolgen. Schlussendlich besteht jedoch kein Zweifel daran, dass die ständig fortschreitende Maschinerie der Gittersimulationen grundlegende Beiträge zur Untersuchung stark wechselwirkender Theorien im Allgemeinen und supersymmetrischer Theorien im Speziellen beitragen wird.

Non-perturbative renormalization on the lattice

Abstract

Strongly-interacting theories lie at the heart of elementary particle physics. Their distinct behaviour shapes our world *sui generis*. We are interested in lattice simulations of supersymmetric models, but every discretization of space-time inevitably breaks supersymmetry and allows renormalization of relevant susy-breaking operators. To understand the role of such operators, we study renormalization group trajectories of the nonlinear $O(N)$ Sigma model (NLSM). Similar to quantum gravity, it is believed to adhere to the asymptotic safety scenario. By combining the demon method with blockspin transformations, we compute the global flow diagram. In two dimensions, we reproduce asymptotic freedom and in three dimensions, asymptotic safety is demonstrated. Essential for these results is the application of a novel optimization scheme to treat truncation errors. We proceed with a lattice simulation of the supersymmetric nonlinear $O(3)$ Sigma model. Using an original discretization that requires to fine tune only a single operator, we argue that the continuum limit successfully leads to the correct continuum physics. Unfortunately, for large lattices, a sign problem challenges the applicability of Monte Carlo methods. Consequently, the last chapter of this thesis is spent on an assessment of the fermion-bag method. We find that sign fluctuations are thereby significantly reduced for the susy NLSM. The proposed discretization finally promises a direct confirmation of supersymmetry restoration in the continuum limit. For a complementary analysis, we study the one-flavor Gross-Neveu model which has a complex phase problem. However, phase fluctuations for Wilson fermions are very small and no conclusion can be drawn regarding the potency of the fermion-bag approach for this model. Nevertheless, it is clear that the ever improving machinery of lattice simulations will provide essential contributions to the study of strongly interacting theories in general and supersymmetric theories in particular.

Contents

1	Motivation	5
2	MCRG Flow of the nonlinear Sigma model	10
2.1	Wilson's renormalization group	10
2.2	Asymptotic Safety	13
2.3	The nonlinear Sigma model	14
2.4	Monte Carlo renormalization group	15
2.5	The demon method	19
2.6	Truncated effective action	20
2.7	Optimized blockspin transformation	23
2.8	$D=2$: Asymptotic Freedom	24
2.9	$D=3$: Asymptotic Safety	27
2.9.1	One-parameter effective action	28
2.9.2	Higher-order truncations	29
2.9.3	Critical exponents	33
2.10	The large N limit	36
2.11	Conclusion	39
3	Continuum limit of the supersymmetric Sigma Model	41
3.1	Supersymmetry	41
3.2	... on the lattice?	42
3.3	Supersymmetric nonlinear $O(3)$ Sigma model	44
3.4	Discretization and residual symmetries	45
3.4.1	Stereographic projection	46
3.4.2	Fine tuning of the continuum limit	49
3.5	Performance of the HMC algorithm	51
3.6	Pfaffian sign	53
3.7	$O(3)$ Symmetry	55
3.8	Chiral symmetry	56
3.9	Bosonic and fermionic mass	58
3.10	Path integral based Ward identity	59
3.11	Conclusion	61

4 Fermion-bag approach to Monte Carlo sign problems	62
4.1 Sign problems in lattice QFT	62
4.2 The fermion-bag method	63
4.3 The supersymmetric nonlinear $O(3)$ Sigma model	64
4.3.1 Derivation of the fermion-bag discretization	65
4.3.2 Quenched ensemble	68
4.3.3 Dual fermion-bag approach	69
4.3.4 The full ensemble	71
4.4 The one-flavor Gross-Neveu model	74
4.4.1 Discretization	77
4.4.2 SLAC fermions	79
4.4.3 The fermion-bag method	82
4.4.4 Wilson fermions	85
4.5 Conclusion	89
5 Summary and Outlook	91
6 Bibliography	95
A Basic symbols and conventions	112
B Lattice definitions	113

1 Motivation

Quantum field theory (QFT) combines the fundamental principles of special relativity and quantum mechanics. It is an incredibly active research field and has applications in many areas of physics. A pedagogical introduction is available in textbooks [1, 2] and reviews [3, 4]. For a basic explanation of lattice QFT, we refer to [5–7]. Lastly, a short account on conventions used here is given in the appendix.

Strongly-interacting theories play a pivotal role in high-energy physics. The Standard Model of particle physics [8] is today’s most successful theory of the fundamental forces - except gravity. It is based on a powerful unifying principle: *local gauge invariance*. The elementary building blocks of all known matter, leptons and quarks, are represented by fermionic quantum fields (see Figure 1). They

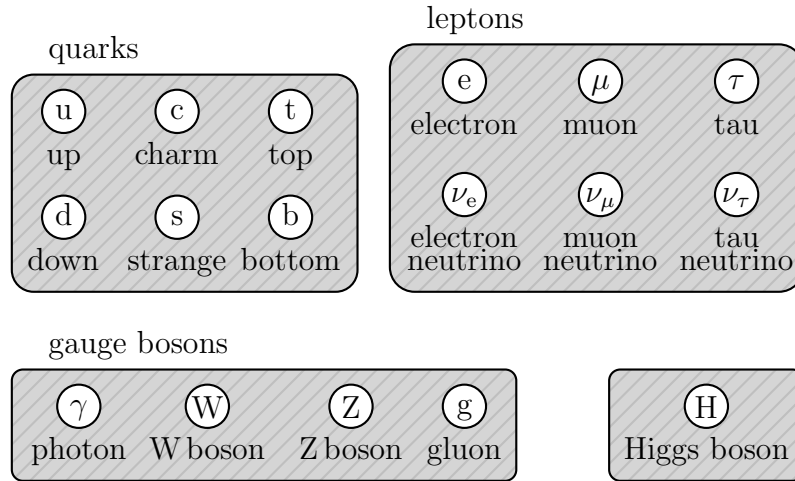


Figure 1: The Standard Model particles (not to scale) come in four groups. Quarks and leptons make up the matter sector and gauge bosons mediate the fundamental forces. The Higgs boson gives mass to elementary particles.

interact through exchange of gauge bosons: photons mediate the electromagnetic force, W and Z bosons are exchanged by the weak interaction and gluons are carriers of the strong interaction. The Standard Model’s final constituent is the recently discovered Higgs particle [9, 10], which provides a mechanism to explain the origin of mass [11].

Quantum Chromodynamics (QCD) describes only one particular aspect of the Standard Model, the strong interaction between quarks and gluons. At high

energies, it is asymptotically free [12, 13] and can be described by perturbation theory. However, the low-energy physics is characterized by a strong fermionic self-interaction that must be treated with a non-perturbative method. This behaviour has immense consequences for our world. Physicists believe [14] that shortly after the big bang, our universe was in an extremely hot and dense state, called Quark-Gluon-Plasma. As the universe expanded, it cooled down and only a fraction of a second after its birth, it underwent a transition to a new phase. This *hadronic phase* is governed by bound states of gluons and quarks: hadrons. They include proton and neutron, which form the nuclei of all known chemical elements. Without these constituents, the rich multitude of forms and structures that make up all of nature could not exist. This transition is denoted as the finite-temperature chiral transition of QCD and it is an important example of spontaneous symmetry breaking¹.

Symmetries, like e.g. local gauge invariance, are incredibly potent concepts. They constrain the limitless possibilities that quantum field theory offers to the theoretical physicist. If a symmetry of the microscopic theory is not broken by quantum effects, then it forbids all processes that would violate it, even on a macroscopic scale. Thereby, a relation is established between the smallest systems in our universe - elementary particles and their interactions - and the largest systems, like e.g. neutron stars or even whole galaxies. A particular example concerns the occurrence of antimatter. Postulated by Dirac in 1928 [15], it is used routinely in modern day particle accelerators and even medical equipment². It is believed that the Big Bang created an equal amount of matter and antimatter [16]. The laws of the Standard Model do not discriminate between particles and antiparticles if \mathcal{CP} -symmetry is valid³. For every physical process that creates or destroys matter, an equivalent process exists for antimatter. Therefore, the balance cannot change. Yet, astronomers have never observed a cosmological region that shows signs of large amounts of antimatter. Is it possible that we simply live in a large bubble of matter and similar bubbles, made of antimatter,

¹Technically this is only true for massless quarks. If the bare mass is non-zero, chiral symmetry is explicitly broken and the phase transition becomes a crossover.

²Positron emission tomography (PET) is a 3D imaging technique. A β^+ radiation source that emits positrons (anti-electrons) is placed inside the body as a tracer. A tomograph then records gamma rays that are produced by electron-positron annihilation.

³Recently, one has even succeeded to artificially produce and store anti-hydrogen [17, 18].

exist just out of our sight? Unfortunately, this is very unlikely. If two bubbles of different content come into contact, a huge portion of matter and antimatter annihilates. Thereby, radiation with a characteristic spectrum is emitted. However, none has been detected so far [19]. One is compelled to conclude that the experimental results, revealing much more matter than antimatter in our universe, cannot be explained by a theory that conforms to \mathcal{CP} -symmetry [20]. Violations of \mathcal{CP} -invariance were also measured in weak decays [21] and an attempt has been made to incorporate these results into the Standard Model. This prospect was achieved through the CKM-matrix [22]. Even so, baryogenesis calculations have revealed that this is not sufficient to explain the large discrepancy between matter and antimatter [16].

The problem of missing antiparticles is an important example for an increasing influence of cosmological observations on elementary particle physics. In order to explain them, one must recognize that a theory beyond the Standard Model is needed. An especially popular approach is *supersymmetry*. It is an extension of the Poincaré symmetry of space-time transformations, connecting states of different spin. Supersymmetric versions of the Standard Model exist and one is interested in the dynamics of these models beyond perturbation theory. However, supersymmetry poses a unique challenge to non-perturbative techniques.

The ab-initio method of choice to describe the non-perturbative dynamics of the strong interaction is Lattice QCD. It has been actively developed for over thirty years and demands immense computational resources. Lattice techniques have a wide range of applicability and allow to study some of the most interesting phenomena, like e.g. dynamic formation of condensates and bound states, dynamic generation of particle masses and spontaneous breaking of symmetry. We are interested in applying lattice methods to supersymmetric theories. However, this prospect is hindered by a fundamental obstacle. It is connected to the discretization of space-time: fields are defined on a finite grid of points and the number of degrees of freedom is restricted. Thus, infinite integrals of the continuum theory are regularized. At the same time, Poincaré symmetry is broken. Only residual symmetries remain. On a hypercubic lattice, these are for example translations by multiples of the lattice spacing or rotations by multiples of $\frac{1}{2}\pi$. In the continuum limit, i.e. sending the lattice spacing to zero, Poincaré symmetry is restored automatically. Unfortunately, this is not necessarily true for super-

symmetry. As an extension of Poincaré symmetry, it is broken by space-time discretization as well. Taking the contributions of virtual particles into account, it is possible that susy-breaking operators emerge. On the lattice, they are no longer forbidden by symmetry principles. If these operators diverge in the continuum limit, then supersymmetry is not restored and the method fails.

The topic of this thesis is to study the non-perturbative renormalization of strongly-interacting quantum field theories on the lattice. This program is represented by three projects that are compiled in the chapters [2](#), [3](#) and [4](#).

In chapter [2](#), we compute the flow diagram of the nonlinear $O(N)$ Sigma model. The flow of the effective average action plays an important role in the analysis of quantum field theories and many properties are directly related to its structure. It allows to study the behaviour of operators near a fixed point and paves the way to an understanding of divergent susy-breaking operators. The model at hand is not supersymmetric but rather shares some properties with quantum gravity. In particular, it is presumed to be asymptotically safe. We will argue that previous studies, based on the functional renormalization group as well as plain lattice simulations, do not provide a satisfactory picture of the global flow diagram. Instead, an alternative method is proposed. It is used to certify asymptotic freedom for the model in two dimensions and asymptotic safety in three dimensions.

Chapter [3](#) is devoted to a study of the supersymmetric nonlinear $O(3)$ Sigma model in two dimensions. This theory features strongly-coupled bosonic and fermionic degrees of freedom and may be regarded as a toy model for the matter sector of the Minimally Supersymmetric Standard Model. Previous studies have failed to provide a discretization that complies with analytical expectations. Therefore, we simulate a novel discretization. Based on lattice observables, we argue that the latter leads to the desired continuum limit. Only a single operator must be fine tuned in order to arrive at this conclusion.

However, the application of Markov Chain Monte Carlo methods to this problem is not straightforward, since the weight of the partition sum is not strictly positive. This is denoted as the sign problem and is particularly common in models including fermionic degrees of freedom. Chapter [4](#) is spent on an investigation of the fermion-bag method. It is an alternative approach to discretize four-fermi interactions. While sign problems can be treated using reweighting

techniques, they are exponentially hard to compute and thus prohibit the study of large lattices, which are needed in order to extrapolate to the continuum limit. No general solution has been found so far and one must study sign fluctuations on a model-by-model basis. For this purpose, we investigate the supersymmetric nonlinear $O(3)$ Sigma model and the one-flavor Gross-Neveu model.

Each chapter is closed by a short conclusion and a summary as well as an outlook on further applications is presented in chapter [5](#).

The compilation of this thesis is solely due to the author. All projects presented here were carried out in the quantum field theory research group in Jena. The MCRG study in chapter [2](#) was realized in collaboration with Björn Wellegehausen and published in [\[23\]](#). Preliminary results of this work have been reported in proceedings [\[24\]](#). Chapter [3](#) was previously published in [\[25\]](#) and in the proceedings [\[26\]](#). The calculation of the stereographically projected Lagrangian and analysis of a possible supersymmetry invariance of the discretized action is due to Raphael Flore. Comparisons to SLAC fermions are based on results by Christian Wozar. All simulation codes were written in C++ . For chapter [2](#), libraries developed by Björn Wellegehausen were used. In Chapter [3](#), the JenLaTT library was utilized. The latter is a joint project of the QFT group Jena. Nevertheless, the author has implemented more than 20.000 lines of code in order to collect the results presented in this thesis. Simulations were carried out on the Loewe-CSC at the University of Frankfurt and on the Omega HPC cluster at the University of Jena.

2 MCRG Flow of the nonlinear Sigma model

2.1 Wilson's renormalization group

Quantum field theories may be defined in different ways. A quantity that is particularly suited to theoretical investigation is the Lagrangian density \mathcal{L} . It is a sum of operators O_i , which are composed of the degrees of freedom of the respective quantum field theory, multiplied by the coupling constants g_i . The action S is the integral of the Lagrangian density over all D space-time coordinates,

$$S = \int d^D x \mathcal{L} = \int d^D x g_i O_i. \quad (2.1)$$

The *bare* parameters g_i do not possess an a priori interpretation and their relation to physical quantities that are accessible in experiments must be uncovered by the solution of the quantum field theory. This procedure includes two different scales: The quantum field theory is defined at small distances and high momenta, since it is composed of the fundamental degrees of freedom. This scale is denoted as the ultraviolet (UV) momentum scale Λ . Experiments however are conducted at macroscopic lengths and momenta, which corresponds to the infrared (IR) momentum scale λ . We can use the action formalism also at the IR scale: it becomes the effective action Γ ,

$$\Gamma = \int d^D x g_i^M O_i^M, \quad (2.2)$$

and includes the macroscopic operators O_i^M that govern the physics of the model at this scale. From the effective action, one is able to extract e.g. the masses or decay widths of physical states and compare them to the experiment. The relation between S and Γ is given by the renormalization of the quantum field theory, which includes the contribution of virtual particles. Thus, through renormalization, a connection between the system in nature that we wish to describe and our theoretical model is established.

A particular method to calculate the renormalization of quantum field theories is Wilson's renormalization group [27, 28]. It is designed to study the problem of the statistical continuum limit. A characteristic property of this problem is that

fluctuations of the involved degrees of freedom contribute equally, regardless of their wavelength. This has been identified as the root cause for many divergences that are frequently encountered in quantum field theories. It is further related to critical phenomena, since the correlation length in critical systems is infinite and fluctuations occur *on all scales*. The central idea of the renormalization group is that different energy scales are *locally coupled*. Picturing a range of momenta, one distinguishes different segments - the momentum shells - that represent fluctuations at a certain scale. The renormalization group produces a cascade: fluctuations at a chosen scale are influenced by the momentum shells directly adjacent. In order to compute the renormalized quantum field theory, one starts at the microscopic action S and integrates out momentum shells one after another, adding up their respective contribution to the effective average action Γ_k . It is scale-dependent and includes all fluctuations between the UV cutoff Λ and the momentum scale k . Once all momentum shells have been integrated out, one has calculated the full effective action $\Gamma = \Gamma_{k \rightarrow 0}$.

The renormalization group cascade may be visualized in an intuitive way. In general, the number of operators O_i is infinite. They are interpreted as directions of a *theory space*. Every possible action that we can write down is given as a point in this space and the coordinates correspond to the coupling constants g_i . The cascade induces a flow of the effective average action through theory space. Step by step, momentum shells are integrated out and Γ_k advances along a trajectory of the *renormalization group (RG) flow*. This behaviour has immediate consequences. One is the existence of scaling, i.e. each intermediate momentum shell tends to contribute identically except for a change of scale. Scaling is achieved when the effective action goes into itself and thus the RG flow has a *fixed point*. The flow is further characterized by amplification and deamplification. Consider a small change of the initial parameters: depending on the structure of the RG flow, the effective action may change significantly. This is particularly apparent in critical phenomena. Starting at the critical value for the couplings, one finds that the correlation length of the system is infinite. However, only a slight deviation is sufficient to change the correlation length to a finite value. In contrast, deamplification is encountered in the case that different initial conditions yield the same effective action. An example is readily provided by nature: different ferromagnetic materials with different atomic structure show identical critical be-

haviour [29]. This important property leads to the *universality hypothesis* [30], which states that the critical behaviour of systems depends only on very general properties, like e.g. the space-time dimension, symmetries and range of interaction, but not on the details of the microscopic action.

All of these phenomena are tightly related to the structure of the RG flow. They provide crucial insights into the physical properties of the model. Given a point in theory space $\{g_i\}$, the flow of the effective average action is generated by a renormalization group transformation R ,

$$\{g'_i\} = R(\{g_i\}). \quad (2.3)$$

The fixed points of R are given by the relation $R(\{g_i^*\}) = \{g_i^*\}$. We read off the local structure of the RG flow in the vicinity of a fixed point from the linearized transformation T_{ij} ,

$$g'_i - g_i^* = T_{ij}(g_j - g_j^*). \quad (2.4)$$

The eigenvalues λ^α and left-eigenvectors v^α are determined by $v_i^\alpha T_{ij} = \lambda^\alpha v_j^\alpha$. The directions around the fixed point are characterized by the scaling variables $u^\alpha = v_i^\alpha(g_i - g_i^*)$. They transform multiplicatively under the RG transformation,

$$(u^\alpha)' = \lambda^\alpha u^\alpha. \quad (2.5)$$

Using the notation $\lambda^\alpha = b^{\theta^\alpha}$, we define the *critical exponents* θ^α and the scale factor $b > 1$. A scaling variable that is related to a direction with $\theta > 0$ is amplified under successive application of the RG transformation. The model is transported away from the fixed point and the direction is thus denoted as a *relevant* direction. The contrasting case of deamplification corresponds to $\theta < 0$: the theory flows towards the fixed point. This behaviour corresponds to an *irrelevant* direction. The remaining case $\theta = 0$ is called *marginal* and requires the study of higher orders of the RG flow.

2.2 Asymptotic Safety

The standard approach to deal with quantum field theories is to calculate perturbative diagrams⁴. This is meaningful if the theory exists in the vicinity of the *Gaussian fixed point*, which is non-interactive. However, one frequently encounters divergent diagrams that originate from the contribution of virtual particles. By renormalization, it is possible to control some of these divergences using counterterms. Unfortunately, if a theory is deemed *perturbatively non-renormalizable*, then the number of counterterms that are required is infinite. In this case, the theory is not predictive, since it demands infinitely many parameters to be fixed by experiment. However, it might still be possible to renormalize the theory in a non-perturbative setting. One such situation is called the *asymptotic safety scenario* [32, 33]. It applies if the model has a non-Gaussian fixed point with only a finite number of relevant directions. Asymptotically safe theories are equally predictive as theories that are perturbatively renormalizable and may play an important role in the description of nature. The most prominent of these theories is general relativity. At present, all results suggest that there exists a non-trivial UV fixed point [34–36] and it is hoped that asymptotic safety leads the way to a theory of quantum gravity.

Recently, the *functional renormalization group* (FRG) [37–39] was applied to study the renormalization group flow of general relativity. It belongs to the class of *exact renormalization group equations*. However, the method is not free of approximations. In order to calculate the RG flow, one is obliged to use an ansatz for the effective average action Γ_k . It is not feasible to represent all of the infinitely many operators that are allowed in general and thus a truncation must be used. Thereby, uncontrolled systematic errors are provoked and at best a qualitative estimation may be obtained by comparing different truncations, e.g. using a derivative expansion [40].

The aim of this project is to present a renormalization group method, based on lattice simulations, that is able to improve on this situation. Different approaches were already used in previous publications to define a running coupling such as the renormalized correlation functions or the Schwinger functional [41]. However,

⁴An introduction to perturbative renormalization is available in many textbooks, for instance [2, 31].

they rely on a connection to perturbation theory, which is not applicable for our models. In an alternative recent approach one tries to directly integrate out momentum shells on the lattice by using Fourier Monte Carlo simulation [42]. Unfortunately, the results depend significantly on the specific parameters of the RG transformation. Thus, systematic errors are large and the method cannot be regarded as stable. We use the *Monte Carlo renormalization group* (MCRG) method to calculate the global flow diagram of the ubiquitous nonlinear O(N) Sigma models (NLSM). Since they share important properties with models of quantum gravity, they provide excellent toy models to test our approach.

2.3 The nonlinear Sigma model

We recall the Euclidean action of the nonlinear O(N) Sigma model with the sphere as target space,

$$S = \frac{1}{2g^2} \int d^D x \partial_\mu \phi \cdot \partial^\mu \phi, \quad (2.6)$$

where ϕ is an N-component scalar field that satisfies the constraint $\phi \cdot \phi = 1$. The coupling g has mass dimension

$$[g] = \frac{2 - D}{2}. \quad (2.7)$$

In two space-time dimensions the global O(N) symmetry cannot be broken due to Mermin-Wagner's theorem [43]. At strong coupling the theory is asymptotically free and the RG flow is dominated by the Gaussian fixed point. Thus, the model is perturbatively renormalizable. This is not surprising since the coupling is dimensionless. For higher dimensions, the coupling acquires a negative mass dimension and perturbative renormalizability is lost. However, the small- ϵ and $1/N$ -expansions both point to the existence of non-trivial fixed points [44–47]. This claim is further supported by FRG calculations based on a one-parameter truncation of the effective action [48] and higher-order truncations [49]. Additionally, lattice simulations with the discretized action

$$S = \frac{1}{2g^2} \sum_{x,\mu} \phi_x \cdot \phi_{x+\hat{\mu}}, \quad (2.8)$$

known as the *Heisenberg ferromagnet*, reveal a critical point that separates a $O(N)$ symmetric phase from a broken phase by a second-order phase transition. In the broken phase there are $N - 1$ Goldstone bosons corresponding to the directions tangential to a sphere in target space. In order to recover the continuum field theory, one uses this critical behavior to define the limit of vanishing lattice spacing. Much effort went into the study of the critical properties of the model and in particular in calculating its critical exponents. Thus, a large number of results is available, e.g. from numerical high-precision Monte Carlo methods, analytical calculations using the high-temperature expansion or renormalization group method and even experimental data from condensed matter physics [29, 48, 50–55].

We are particularly interested in the flow diagram of the three-dimensional model that is conjectured to show a non-trivial UV fixed point, a necessary requirement for the asymptotic safety scenario to be at work. However, we will also reproduce the known results for the model in two dimensions in order to test our approach.

2.4 Monte Carlo renormalization group

In the present work we make use of the MCRG method. It is based on Kadanoff's idea of blockspin transformations [56] and can be applied to a wide range of theories, including fermionic and gauge fields [57]. We study a lattice with equal temporal and spatial extent L . The physical volume is hence $(aL)^D$, where a denotes the lattice spacing. The lattice naturally introduces a UV-cutoff at an energy $\Lambda = a^{-1}$ and the lattice size aL serves as an IR-cutoff at a lower energy $\lambda = (aL)^{-1}$. In Monte Carlo simulations, one estimates the n -point functions

$$\langle \phi(x_1) \dots \phi(x_n) \rangle = \frac{\int \mathcal{D}\phi \phi(x_1) \dots \phi(x_n) e^{-S[\phi]}}{\int \mathcal{D}\phi e^{-S[\phi]}}, \quad (2.9)$$

by expectation values of lattice operators,

$$\langle \phi_{x_1} \dots \phi_{x_n} \rangle = \frac{\int \prod_x d\phi_x \phi_{x_1} \dots \phi_{x_n} e^{-S(\{\phi_x\})}}{\int \prod_x d\phi_x e^{-S(\{\phi_x\})}}, \quad (2.10)$$

from which all physical quantities, like e.g. particle masses and decay widths, can be extracted. Thereby, all quantum fluctuations with scales between the upper and lower cutoff are taken into account. The macroscopic physics is fixed by the simulation parameters. These are the lattice extent L and the coupling constants g_i of the microscopic (bare) action. The renormalization group transformation (2.3) relates the parameter set $\{g_i\}$ at the high energy scale Λ to a parameter set $\{g'_i\}$ at a lower energy scale Λ' ,

$$\{g_i\}(\Lambda) \longmapsto \{g'_i\}(\Lambda') = R_{\Lambda \mapsto \Lambda'}(\{g_i\}). \quad (2.11)$$

An important property of any such RG transformation is that it does not depend on the details of the flow in theory space. In particular the transformation must obey the semigroup properties

$$R_{\Lambda \mapsto \Lambda'} = R_{\Lambda \mapsto \Lambda''} \circ R_{\Lambda'' \mapsto \Lambda'}, \quad R_{\Lambda \mapsto \Lambda} = 1, \quad (2.12)$$

where $\Lambda > \Lambda'' > \Lambda'$. Valid transformations are given by the blockspin transformations. A blockspin transformation with scale parameter $b > 1$ relates a field configuration $\{\phi_x\}$ on the fine lattice (L, a) to an averaged configuration $\{\phi'_x\}$ on the coarser lattice $(L' = L/b, a' = ba)$. The IR-cutoff does not change and the blocked and initial configurations describe the same macroscopic physics. In contrast, the UV-cutoff $\Lambda \rightarrow \Lambda' = \Lambda/b$ is lowered and the effective parameters $\{g'_i\}$ defined at the new cutoff Λ' incorporate the effects of all quantum fluctuations with scales between Λ and Λ' . This is depicted in Figure 2. Numerical simulations on the coarse lattice with couplings $\{g'_i\}$ and on the fine lattice with couplings $\{g_i\}$ yield the same ensemble, i.e. identical n -point functions. Each set of parameters defines a point in theory space and they are connected by an RG trajectory. Real-space RG transformations are performed by successive application of blockspin transformations and thus the RG flow is established.

An infinitesimal RG transformation has a scale parameter $b = 1 + \delta b$ ($\delta b \ll 1$). The change of the couplings is described by the β -function β_i

$$g'_i = g_i + \underbrace{\frac{dg_i}{db}}_{-\beta_i(\{g_j\})} \delta b + \mathcal{O}(\delta b^2). \quad (2.13)$$

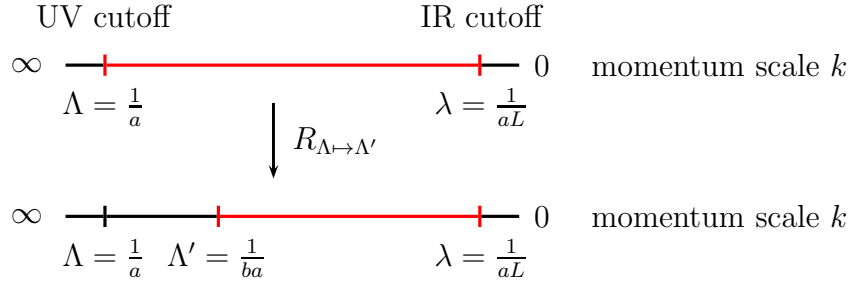


Figure 2: A lattice simulation takes all fluctuations with scales between the lower cutoff λ and the upper cutoff Λ into account (depicted in *red*). The blockspin transformation R yields a set of effective coupling parameters at the reduced cutoff Λ' , which already incorporates the contributions between Λ and Λ' . By iterating this step, a renormalization group trajectory in theory space is established.

The fixed points of the RG flow correspond to the zeros of the beta function. In the vicinity of such a fixed point, the linearized transformation (2.4) reads:

$$T_{ij}(g_j - g_j^*) = g_i - g_i^* - \left. \frac{\partial \beta_i}{\partial g_j} \right|_{g_j^*} (g_j - g_j^*) \delta b \quad \Rightarrow \quad T_{ij} = \delta_{ij} - \underbrace{\left. \frac{\partial \beta_i}{\partial g_j} \right|_{g_j^*}}_{S_{ij}} \delta b. \quad (2.14)$$

The matrix S_{ij} is called the *stability matrix*. The eigenvalues λ^α of the linearized transformation are

$$\lambda^\alpha = b^{\theta^\alpha} = (1 + \delta b)^{\theta^\alpha} = 1 + \theta^\alpha \delta b + \mathcal{O}(\delta b^2) \quad (2.15)$$

and the critical exponents θ^α thus are the negative eigenvalues of the stability matrix. They are related to the thermodynamical critical exponents, which describe the scaling of singular thermodynamic observables near a critical point. For the scenario of a single relevant direction, which is presumed in the case of the three-dimensional model, one finds $\nu = (\theta^r)^{-1}$ for the critical exponent of the correlation length ν and the eigenvalue θ^r of the relevant direction. Using the MCRG method, we compute the *lattice beta function* $\hat{\beta}_i$,

$$\hat{\beta}_i = \frac{g'_i - g_i}{1 - b} = -a \frac{g'_i(a') - g_i(a)}{a' - a} \stackrel{a' \rightarrow a}{=} -a \frac{\partial g_i}{\partial a} = \frac{\partial g_i}{\partial \log \Lambda} = -\frac{\partial g_i}{\partial b} = \beta_i \quad (2.16)$$

In the vicinity of a critical point, the correlation length is huge and the lattice

spacing goes to zero. Thus the difference $a' - a = (b - 1)a$ goes to zero as well and we expect that discretization errors are small. In order to compute the critical exponents, we measure the eigenvalues of the *lattice stability matrix* \hat{S}_{ij} ,

$$\hat{S}_{ij} = \frac{\beta_i(g_j + \delta g_j) - \beta_i(g_j - \delta g_j)}{2\delta g_j}, \quad (2.17)$$

which involves the discretization of a second derivative.

The most popular MCRG method is the so-called *matching method* [58–62]. It is based on the observation that a universal attractor for the renormalization group trajectories exists. It is called the *renormalized trajectory (RT)*. The first part of the method is concerned with the creation of a Markov chain of configurations on a fine lattice with simulation parameters $(L, \{g_i\})$. On each configuration, a number of n blockspin transformations is iterated. The blockspin expectation values characterize the macroscopic physics, e.g. the blockspin correlation length ξ . It is important that the number of blocking iterations is sufficiently large such that the renormalized trajectory is reached. The second part consists of a number of lattice simulations using the coarse lattice size L/b and different parameters $\{g'_i\}$ for each run. Its goal is to find a set of couplings such that the blockspin expectation values for the two lattices match. Please note that on the coarse lattice, only $n - 1$ blockspin transformations are needed in order to arrive at the same lattice size as for the fine lattice. The correlation length is thus $b^n \xi$ on the fine lattice and $b^{n-1} \xi$ on the coarse lattice. Therefore, a comparison of the coupling parameters yields the shift needed to change the correlation length by a factor b and one has thus computed the lattice beta function. Unfortunately, every RG step reduces the linear extent of the lattice by a factor b . Hence, exponentially large lattices are needed in order to obtain sufficiently long trajectories that get close enough to the renormalized trajectory [51]. Even worse, expensive scanning runs for the parameters on the coarse lattice are needed. Furthermore, the method is not applicable if the RT does not act as an attractor for the renormalization group trajectories, e.g. in the vicinity of the Gaussian fixed point [63]. In order to circumvent these problems, we employ the *demon method* which allows us to efficiently compute RG trajectories at a fixed lattice volume.

2.5 The demon method

The demon method [64–66] allows one to calculate couplings of an effective action $S = g_0 S_0$ such that the corresponding distribution is close to a given ensemble of lattice configurations. Given a partition function

$$Z(g_0) = \int \mathcal{D}\phi e^{-g_0 S_0[\phi]}, \quad (2.18)$$

an additional degree of freedom E_D , the *demon energy*, is introduced with the combined partition function

$$Z_D(g_0) = \int \mathcal{D}\phi \int dE_D e^{-g_0 S_0 - g_0 E_D} \quad (2.19)$$

of the canonical demon ensemble. The expectation value of the demon energy can be calculated in a simulation of the microcanonical ensemble,

$$Z_{\text{MCD}} = \int \mathcal{D}\phi \int dE_D \delta(S_0 + E_D - E_0). \quad (2.20)$$

It is a function of the coupling parameter g_0 , thus allowing to *measure* g_0 corresponding to the combined ensemble. This method can be generalized to more than one coupling constant, i.e.

$$Z_{\text{MCD}} = \int \mathcal{D}\phi \prod_i \int dE_D^i \delta(S^i + E_D^i - E_0^i). \quad (2.21)$$

Constraining the demon energy to $E_D^i \in (-E_m^i, E_m^i)$ yields

$$\langle E_D^i \rangle_D = \frac{1}{g_i} - \frac{E_m^i}{\tanh(g_i E_m^i)} \approx \langle E_D^i \rangle_{\text{MCD}} \quad (2.22)$$

where the subscript D denotes the canonical demon ensemble (2.19) and MCD the microcanonical demon ensemble (2.20). This equation can be solved by numerical means and is used to extract the coupling constants $\{g_i\}$ from the mean demon energies on the right hand side. In the microcanonical ensemble the total energy is fixed. Since we want to measure the couplings of the blocked ensemble without interference from the demon, we demand that $|E_D^i| \ll |S^i|$. Then the algorithm

for our MCRG setup reads as follows:

1. Pick a configuration distributed according to the canonical ensemble with action $S = g_1 S_1 + g_2 S_2 + \dots$ on the fine lattice.
2. Perform a blockspin transformation on this configuration.
3. Use the result as the starting configuration for a microcanonical simulation of the combined system (2.21) and measure the mean demon energies. The starting values for the demon energies are given by the mean demon energies extracted from the previous microcanonical runs.
4. Repeat step one to three until a sufficient number of configurations has been generated.
5. Calculate the couplings g'_i from the mean demon energies.

A comparison of these couplings with the initial ones yields the lattice beta function. In our setup, an RG transformation consists of the two steps illustrated in Figure 3:

1. A blockspin transformation applied to an ensemble with fixed couplings $\{g_i\}$. This step respects the semigroup properties (2.12).
2. The demon method to measure the effective couplings $\{g'_i\}$ on the blocked lattice. Since this method can only be applied to a truncated effective action, the semigroup property is violated.

The next chapter is dedicated to a discussion of the effects of truncating the effective action.

2.6 Truncated effective action

In general, more and more operators are generated by the repeated application of the blockspin transformation. Since it is impossible to keep track of all of them, we restrict our analysis to an ansatz for the effective action that only includes the most important operators. Thereby, the demon method leads to a projection of RG trajectories from general theory space down to modified trajectories in a

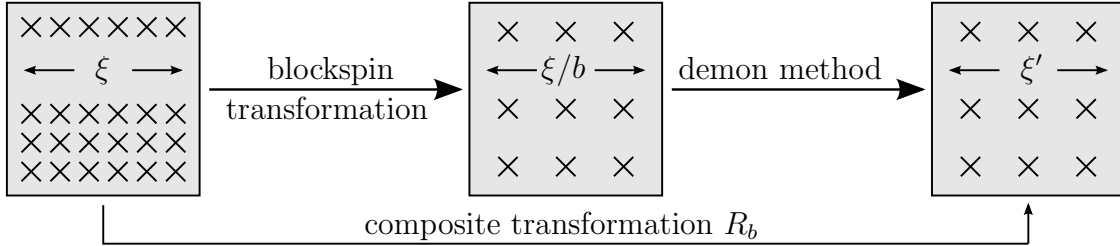


Figure 3: The composite transformation R_b relates coupling constants on a lattice with correlation length ξ to a coarser lattice with correlation length ξ' . It is obtained by using a blockspin transformation and mapping the resulting configurations onto a truncated effective action with the demon method. Simulating the truncated ensemble may not necessarily yield $\xi' = \xi/b$ due to truncation errors.

truncated theory space. It only consists of the terms contained in the effective action. Naturally, this procedure introduces additional systematic uncertainties which we will denote as truncation errors. A qualitative understanding of these errors is obtained by comparing different truncations. For this reason, we use a systematic derivative expansion of the effective action up to fourth order. In the continuum formulation it is given by

$$S[\phi] = \sum_{i=0}^3 g_i N S_i[\phi] + \mathcal{O}(\partial^6) \quad (2.23)$$

with operators

$$S_0 = - \int d^D x \phi \cdot \partial_\mu \partial^\mu \phi, \quad (2.24)$$

$$S_1 = \int d^D x \phi \cdot (\partial_\mu \partial^\mu)^2 \phi, \quad (2.25)$$

$$S_2 = \int d^D x (\phi \cdot \partial_\mu \partial^\mu \phi)^2, \quad (2.26)$$

$$S_3 = \int d^D x (\phi \cdot \partial_\mu \partial^\nu \phi)(\phi \cdot \partial^\mu \partial_\nu \phi). \quad (2.27)$$

Note that we have introduced an additional factor N in (2.23) in order to get rid of the leading N dependence of the couplings g_i . They have mass dimension

$$[g_0] = D - 2, \quad [g_i] = D - 4 \quad \text{for } i = 1, 2, 3. \quad (2.28)$$

This is a complete set of the fourth order operators that are compatible with the symmetries of the model. As a next step, we discretize the action (2.23) on a hypercubic lattice,

$$S(\{\phi_x\}) = \sum_{i=0}^3 g_i N S'_i(\{\phi_x\}), \quad (2.29)$$

where a straightforward discretization of the continuum operators is given by

$$S'_0 = 2 \sum_{x,\mu} \phi_x \cdot \phi_{x+\mu} - 2DV \quad (2.30)$$

$$S'_1 = 2 \sum_{x,\mu,\nu} \phi_x \cdot (\phi_{x+\mu+\nu} + \phi_{x+\mu-\nu}) - 4D \sum_{x,\mu} \phi_x \cdot \phi_{x+\mu} + 4D^2V \quad (2.31)$$

$$S'_2 = \sum_{x,\mu,\nu} \{(\phi_x \cdot \phi_{x+\mu})(\phi_x \cdot \phi_{x+\nu}) + (\phi_x \cdot \phi_{x-\mu})(\phi_x \cdot \phi_{x-\nu}) + 2(\phi_x \cdot \phi_{x+\mu})(\phi_x \cdot \phi_{x-\nu})\} - 8D \sum_{x,\mu} \phi_x \cdot \phi_{x+\mu} + 4D^2V \quad (2.32)$$

$$S'_3 = \sum_{x,\mu,\nu} \{(\phi_x \cdot \phi_{x+\mu})(\phi_x \cdot \phi_{x+\nu}) + (\phi_x \cdot \phi_{x-\mu})(\phi_x \cdot \phi_{x-\nu}) - 2(\phi_x \cdot \phi_{x+\mu})(\phi_x \cdot \phi_{x+\nu-\mu}) - 2(\phi_x \cdot \phi_{x-\mu})(\phi_x \cdot \phi_{x+\mu-\nu}) + (\phi_x \cdot \phi_{x+\nu-\mu})(\phi_x \cdot \phi_{x+\mu-\nu}) + 2(\phi_x \cdot \phi_{x+\mu-\nu})\} + 2D \sum_{x,\mu} (\phi_x \cdot \phi_{x+\mu})(\phi_x \cdot \phi_{x-\mu}) - 4D \sum_{x,\mu} \phi_x \cdot \phi_{x+\mu} + D^2V. \quad (2.33)$$

This set of lattice operators mixes operators of different range and field content. We expect that the nearest neighbor operator $\phi_x \cdot \phi_{x+\mu}$ corresponds to a relevant direction. In order to single this operator out, it is useful to reparametrize the action:

$$\begin{pmatrix} S'_0 \\ S'_1 \\ S'_2 \\ S'_3 \end{pmatrix} = \begin{pmatrix} 2 & 0 & 0 & 0 \\ -4D & 2 & 0 & 0 \\ -8D & 0 & 1 & 0 \\ -4D & 0 & 0 & 1 \end{pmatrix} \begin{pmatrix} \hat{S}_0 \\ \hat{S}_1 \\ \hat{S}_2 \\ \hat{S}_3 \end{pmatrix} + \begin{pmatrix} -2DV \\ 4D^2V \\ 4D^2V \\ D^2V \end{pmatrix}. \quad (2.34)$$

As an additional benefit, we find through numerical tests that the demon method converges faster. For simplicity we drop the hat over lattice quantities in the following.

2.7 Optimized blockspin transformation

In a lattice simulation we have access to observables, like e.g. the masses, which receive contributions from *all possible* lattice diagrams. This information, which is in part lost if one uses a truncated effective action, allows us to extend our analysis of truncation errors. The macro-physics is completely determined by the correlation functions and hence must agree for the original and blocked ensemble in Figure 3, since the blockspin transformation does not change the IR physics. Application of the demon method leads to a truncated ensemble. In general, the correlation functions of the blocked and truncated ensemble do not coincide. This discrepancy is solely due to the truncation of the effective action. In addition to the blocked ensemble, we also simulate the truncated ensemble and measure the difference in the correlation functions. Thus, we quantify the systematic truncation errors directly.

The correlation function difference is reduced by an appropriately adjusted blockspin transformation. The location of the renormalized trajectory in theory space depends on the chosen renormalization scheme [59]. We aim to construct a scheme for which the renormalized trajectory is closest to our truncated effective action. For this prospect, we employ a blockspin transformation where one draws the averaged fields according to a normalized probability distribution,

$$\mathcal{P}(\phi'_x) \propto \exp\left\{C \phi'_x \cdot \Phi_x(\{\phi_y\})\right\}, \quad (2.35)$$

where

$$\Phi_x(\{\phi_y\}) = \frac{1}{|\square|} \sum_{y \in \square_x} \phi_y \quad (2.36)$$

is the sum over all degrees of freedom within a hypercube of the fine lattice. In our computations, we choose the smallest cube of size $b^D = 2^D$. The positive function C determines how strongly the blocked fields fluctuate away from the original degrees of freedom. We shall use a function which minimizes the systematic errors induced by the unavoidable truncation of the effective action. In general, the optimal value depends on the coupling constants, lattice size, target space and number of RG steps. Only in the ideal case without truncation we expect our results to be independent of the RG scheme and thus of the optimization function C .

In order to tune C in the improved blockspin transformation, we compare the correlation lengths extracted from the two-point-functions on the fine and coarse lattice. For simplicity, all higher correlation functions are ignored. Blockspin transformations reduce the lattice correlation length ξ exactly by a factor b . Thus we demand the correlation length ξ' in the truncated ensemble to be equal to ξ/b in order to minimize truncation errors,

$$\xi' = \frac{\xi}{b}. \quad (2.37)$$

The optimization function is chosen to depend linearly on the couplings,

$$C(g) = \sum_i c_i g_i, \quad c_i = \text{const.} \quad (2.38)$$

It is clear from the structure of (2.35) that the choice $C = 0$ leads to a complete loss of information. It is hence necessary to choose $c_i > 0$. In the following computations, we find that in the vicinity of the non-Gaussian fixed point, the higher couplings g_i are small compared to g_0 . Thus, C is governed by the $c_0 g_0$ contribution and it is sufficient to keep the c_i constant while only tuning the first parameter c_0 in order to match the condition (2.37).

Finally, we remark that the lattice itself together with the blockspin transformation correspond to the regulator function used in the FRG framework. Our optimization scheme corresponds to the choice of an optimal regulator which minimizes the flow time (RG steps) from the UV to the IR. Please note however that we take into account information from all lattice operators without truncation.

2.8 $D = 2$: Asymptotic Freedom

In order to test our method, we reproduce the beta function for the two dimensional model. It has already been computed using the MCRG matching method for $N = 3$ [58] and $N \rightarrow \infty$ [59, 63]. The MCRG demon method has been used to determine the running coupling for $N = 3$ [67]. The coupling constant g_0 of the Heisenberg ferromagnet $S = g_0 S_0 N$ is dimensionless and the theory is asymptotically free. We expect that the flow diagram contains two trivial fixed points, one in the IR at vanishing coupling and the other in the UV at infinite coupling

[51]. However, for numerical simulations only finite lattices are accessible. It is known that the theory possesses a transition from a symmetric regime at low coupling (large physical volume) to an ordered regime at strong coupling (small physical volume). We measure the alignment of spins by the absolute value of the lattice-averaged field,

$$\varphi = \left| \frac{1}{V} \sum_x \phi_x \right|. \quad (2.39)$$

It is shown in Figure 4 (left panel) as a function of the coupling for different lattice sizes. With increasing volume the transition shifts to larger values of the

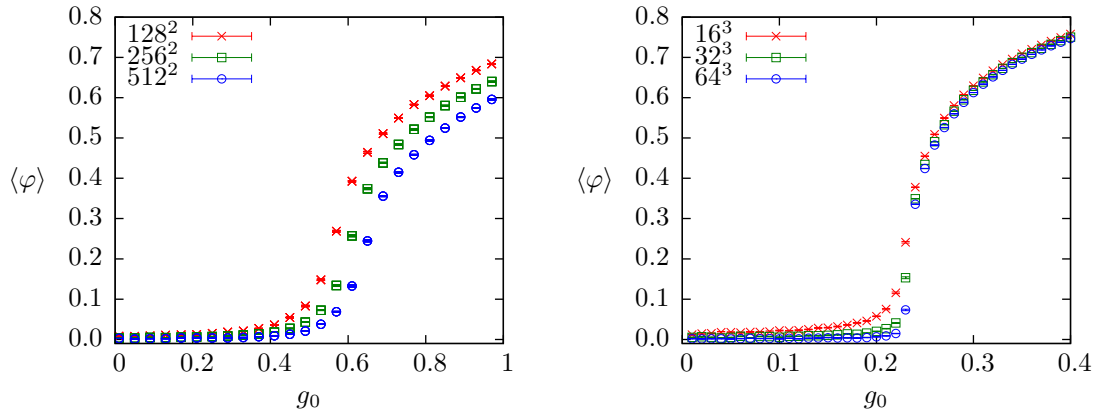


Figure 4: The expectation value of the absolute lattice-averaged spins for the Heisenberg ferromagnet is shown as a function of g_0 for different lattice sizes. The left panel depicts the behaviour in two dimensions and the right panel corresponds to three dimensions.

coupling. In the infinite volume limit, the theory is in the symmetric regime for every finite value of the coupling, as predicted by the Mermin-Wagner theorem. It is also evident that finite volume effects must not be neglected for large coupling. In particular, the observed behaviour might mimic an additional fixed point of the RG flow. In Figure 5 (left panel) we show the β -function for the coupling g_0 in the simplest truncation using only the operator S_0 . We observe that it is independent of the lattice volume. It depends however on the parameter c_0 of the RG transformation. For all values of c_0 , we find an IR fixed point at vanishing coupling, which corresponds to a state of absolute disorder. The spins are randomly aligned and it is thus called the *high-temperature fixed point*. There exists an analogous fixed point at infinite coupling, where the spins are aligned

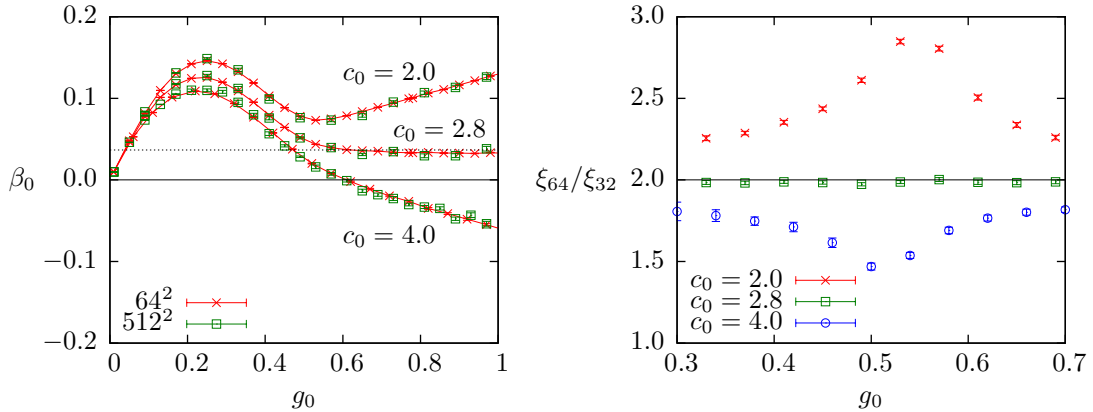


Figure 5: The beta function (left panel) for the simplest possible truncation and $N = 3$ is almost independent of the lattice volume. For $c_0 < 2.8$ it possesses only one fixed point at vanishing coupling. For $c_0 = 2.8$ it becomes constant for $g \rightarrow \infty$. The dotted line represents the analytical result for $N \rightarrow \infty$ and $g \rightarrow \infty$. For $c_0 > 2.8$ we find an additional fixed point at finite coupling which is an artifact of the truncation. The ratio of the correlation length for a 64^2 and 32^2 lattice is shown in the right panel for different parameters of the RG transformation.

uniformly. It is the *low-temperature fixed point* and depicts absolute order. For $c_0 = 2$, the β function stays positive even for large coupling. Increasing c_0 , it develops a second zero crossing at finite coupling. However, this additional zero is an artifact of the truncation. In Figure 5 (right panel), we show the ratio of correlation lengths of the original ensemble on the 64^2 lattice compared to the truncated ensemble on the 32^2 lattice. Truncation errors are assumed to be minimal if $\xi_{64}/\xi_{32} = 2$. Significant deviations are visible for $c_0 = 2$ and $c_0 = 4$. We find that $c_0 = 2.8$ provides a good matching for a large range of couplings. The corresponding beta function does not show an additional zero crossing, as expected. For large g_0 it approaches a constant value, which lies near the large N result $\beta(N \rightarrow \infty, g \rightarrow \infty) = \ln(2)/(6\pi)$ [63].

These findings emphasize that the optimization scheme is of critical importance. Without a means to decide on the specific value for c_0 , the physical information is concealed behind systematic uncertainties.

In order to further improve on our truncation, we add the operator S_1 to the ansatz and the resulting flow diagram for fixed $c_0 = 3.0$ is shown in Figure 6. The flow is no longer independent of the volume and for the small lattice, which is 16^2 , no clear picture of the RG flow can be read off. For g_0 and g_1 large, an

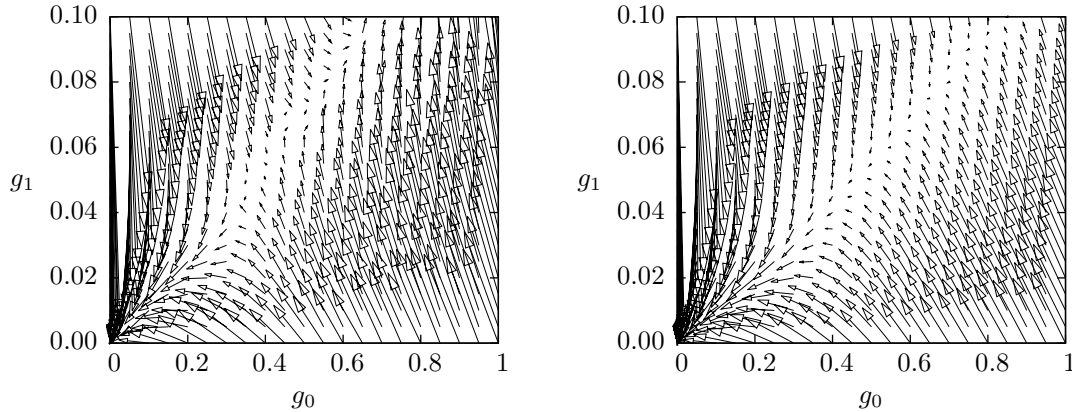


Figure 6: Shown is the flow diagram for $c_0 = 3$ and $N = 3$ in the two operator truncation on a 16^2 (left panel) and 64^2 (right panel) lattice.

additional fixed point seems to emerge. However, going to larger lattice volumes, this behaviour goes away. In the infinite volume limit, no additional fixed point exists.

The renormalized trajectory is the single trajectory that connects the trivial fixed points at the origin and at infinite coupling. The arrows plotted in Figure 6 point towards the IR. Therefore, the high-temperature fixed point is IR-attractive, while the low-temperature fixed point is IR-repulsive. The flow diagram perfectly reflects the idea of deamplification: all renormalization group trajectories flow into the high-temperature fixed point, regardless of the starting point. The structure of the flow diagram fully matches the prediction from asymptotic freedom. All known results for the flow diagram are very well reproduced with our method and we proceed with the case in three space-time dimensions.

2.9 $D = 3$: Asymptotic Safety

As in two dimensions, we first investigate the $O(3)$ model. The order parameter (2.39) for $O(3)$ symmetry is shown in Figure 4 (right panel). In contrast to two dimensions, the symmetry is broken spontaneously: for couplings above the critical coupling, φ does not vanish even on large lattices. The critical coupling in the infinite volume limit is given by $g_0^c = 0.2287462(7)$ [29].

2.9.1 One-parameter effective action

We begin with the simplest truncation possible by using the one-parameter action $S = g_0 N S_0$. We denote this scheme as $1 \rightarrow 1$ truncation, indicating the use of the one-parameter action in both ensemble creation and effective action ansatz. Similar to the $D=2$ results, we find that the dimensionless β function, depicted in Figure 7 (left panel), is almost independent of the lattice size. In contrast to the two dimensional case, β_0 shows a zero crossing at finite coupling for every value of c_0 . This clearly indicates a non-trivial fixed point [44–48]. It is directly related to a second-order phase transition and points to the non-perturbative renormalizability of the O(3) model. In order to determine the optimization

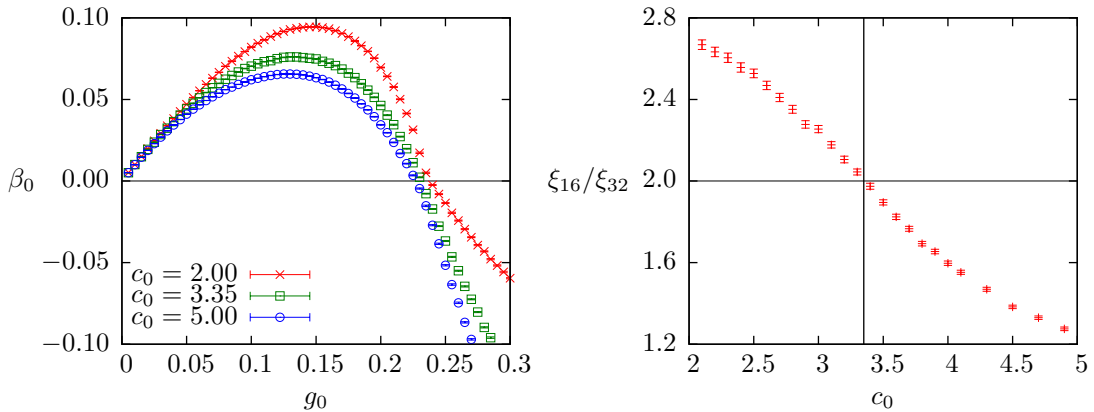


Figure 7: The β function for the $1 \rightarrow 1$ truncation on a 32^3 lattice and $N = 3$ is shown in the left panel for different values of c_0 . In the right panel, the ratio of correlation lengths, obtained by blocking a 32^3 lattice down to 16^3 , is shown for $N=3$ depending on the optimization constant. One expects that $\xi_{16}/\xi_{32} = 2$ minimizes truncation errors. We read off the optimal value $c_0^{\text{opt}} = 3.35$.

constant c_0 , we again consider the correlation length of the two-point function. A perturbative calculation [59] yields $c_0^{\text{pert}} = 2.3$ for arbitrary N and a large number of subsequent RG steps. Computing the ratio of correlation lengths however, we find the optimal choice to be $c_0^{\text{opt}} = 3.35$ (see Figure 7, right panel). Both values deviate significantly, indicating that a non-perturbative optimization scheme is indeed needed.

For the optimal choice c_0^{opt} , we obtain the fixed point coupling $g_0^* = 0.2310(5)$. Systems with bare coupling $g_0 < g_0^*$ flow to the disordered phase in the IR. It is controlled by the high temperature fixed point at $g_0 = 0$. Analogously, systems

with bare coupling $g_0 > g_0^*$ flow to the completely ordered phase, described by the low-temperature fixed point at $g_0 = \infty$. The critical hypersurface is reduced to a single point g_0^* and the operator S_0 corresponds to a *relevant* direction of the RG flow.

The critical coupling g_0^c is characterized as the point where the correlation length of the system diverges at infinite volume. Its location can be determined from thermodynamical observables like e.g. the susceptibility of the order parameter. It is the point of intersection between the critical hypersurface and the line where $g_i = 0$ except g_0 . A lattice simulation starting at g_0^c will flow along the critical line into the non-trivial fixed point. In general, one would expect that the fixed point value g_0^* is identical to g_0^c . However, taking truncation errors into account, this does not need to be true.

While a non-trivial fixed point could be identified, it is still important to know the total number of relevant directions. Therefore, we proceed to discuss higher-order truncations.

2.9.2 Higher-order truncations

Using different lattice sizes, it is evident that results from 8^3 and 16^3 lattices already agree within their statistical error bars. We are therefore confident that simulations on lattices with 32^3 points do not suffer from large finite size effects. Figure 8 shows the global flow diagram for the truncation $S = g_0 N S_0 + g_1 N S_1$. It is used both for ensemble generation as well as in the demon method ($2 \rightarrow 2$ truncation). The blockspin transformation is optimized in a similar fashion as for the action with a single parameter. Using the parametrization $C = c_0 g_0 + c_1 g_1$, a set of parameters c_0 and c_1 is sought-after such that the correlation length ratio is around 2 in the vicinity of the fixed point. Of course, our choice is not unique since we only tune the correlation length. In general, we have to consider higher correlation functions as well. Here, we use the values $c_0 = 3.1$ and $c_1 = 2.5$.

The high-temperature fixed point (HT FP) is located at zero coupling in the lower left corner of the flow diagram. Outside of the printed area, at infinite coupling, lies the low temperature fixed point (LT FP). Additionally, a non-Gaussian fixed point (NG FP) in the center of the flow diagram is clearly visible. Its position is at $g_0^* = 0.119(1)$ and $g_1^* = 0.0164(2)$. As expected, the length of

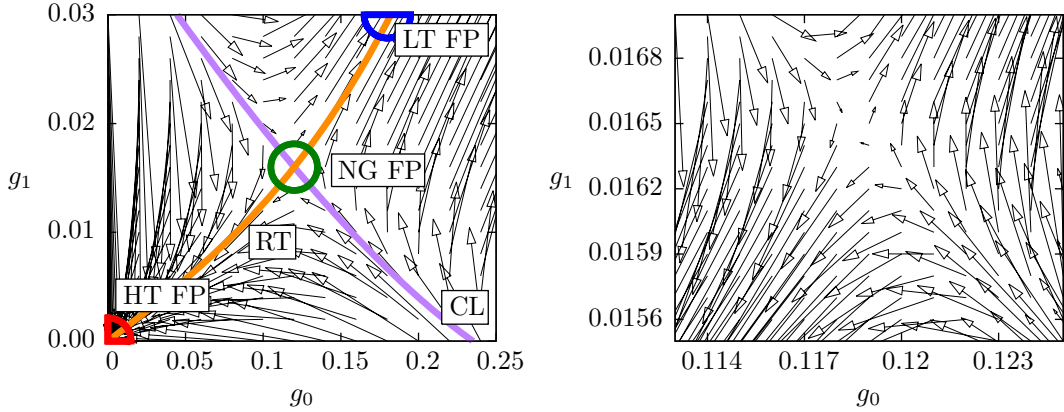


Figure 8: The flow diagram using the $2 \rightarrow 2$ truncation on a 32^3 lattice and $N=3$ clearly shows a non-Gaussian fixed point (NG FP) in the center of the plot (left panel). The critical line (CL) and renormalized trajectory (RT) intersect at the NG FP. The right panel shows a detailed plot of the vicinity of the NG FP.

a trajectory gets small in the fixed point regime. According to equation (2.16), the thickness of the momentum shell that is integrated out is proportional to the lattice spacing. In the vicinity of the fixed point, a goes to zero and the blockspin transformation approaches an infinitesimal RG transformation. Thus, the lattice beta function approaches the continuum beta function. The position of the fixed point is not universal and thus depends on the renormalization scheme. In the two parameter truncation, it depends only weakly on the lattice volume, but varies with the optimization constants. The dominant contribution is given by c_0 since the coupling g_0 exceeds g_1 by an order of magnitude. The flow diagram is split by a separatrix which defines the critical line (CL). It extends from the lower right to the upper left corner. The CL is the intersection of the critical hypersurface in general theory space with the g_0 - g_1 plane that constitutes our truncation. Trajectories that lie above this line will flow into the low temperature fixed point, while trajectories below flow into the high temperature fixed point. This behaviour corresponds to the amplification property of the renormalization group flow. Thereby, a relevant direction is indicated analogous to the simple one-parameter truncation of the preceding section. The second direction though is an irrelevant one. The single trajectory that is identical with the critical line flows into the non-Gaussian fixed point. From the traditional lattice perspective, the CL corresponds to a fine tuned set of bare parameters (g_0, g_1) at different

UV cutoffs. Starting a simulation on the critical line results in a measurement of the critical physics at the non-trivial fixed point. Since the lattice spacing in units of the correlation length becomes small as the critical point is approached, this behaviour is usually used to take the continuum limit.

The renormalized trajectory (RT) connects all three fixed points and acts as an attractor for the RG trajectories. It singles out a unique theory that is both IR and UV complete: the microscopic physics is given by the non-trivial fixed point and the effective average action flows either into the high-temperature or low-temperature fixed point, depending on the starting condition. As expected, the RT does not attract the trajectories in the vicinity of the high temperature fixed point.

Starting on the g_0 axis, which corresponds to the usual lattice action of the Heisenberg ferromagnet, and integrating out all fluctuations, one can only reach either one of the trivial fixed points or the non-trivial fixed point. In this sense, all of them are considered infrared fixed points. From universality arguments, one expects that the NG FP corresponds to the well-known Wilson-Fisher fixed point of the linear Sigma model, since it shares the same $O(3)$ symmetry. Indeed, a similar structure to our results emerges in this model [68]. However, the Heisenberg ferromagnet is an effective theory that is well defined only for a finite UV cutoff. In contrast, *asymptotically safe theories* are defined on all scales. Thus, the fundamental field theory corresponds to the renormalized trajectory. The direction of the RG flow indicates that the non-trivial fixed point governs the ultraviolet physics of this theory. Hence, we clearly identify this non-trivial fixed point as an *ultraviolet fixed point* of the RG flow.

As the next step, the flow diagram for the $3 \rightarrow 3$ and $4 \rightarrow 4$ truncation is computed. Thereby, the operators $\{S_0, S_1, S_2\}$, $\{S_0, S_1, S_3\}$ or $\{S_0, S_1, S_2, S_3\}$ are included respectively. An overview of the flow diagram for the operators $\{S_0, S_1, S_2\}$ is presented in Figure 9. It is evident that only an irrelevant direction is added to the truncation. The global structure of the flow diagram is similar to the $2 \rightarrow 2$ truncation. It shows two trivial IR fixed points and a non-trivial UV fixed point. The latter is located at

$$g_0^* = 0.13(1), \quad g_1^* = 0.016(1) \quad \text{and} \quad g_2^* = -0.0015(5). \quad (2.40)$$

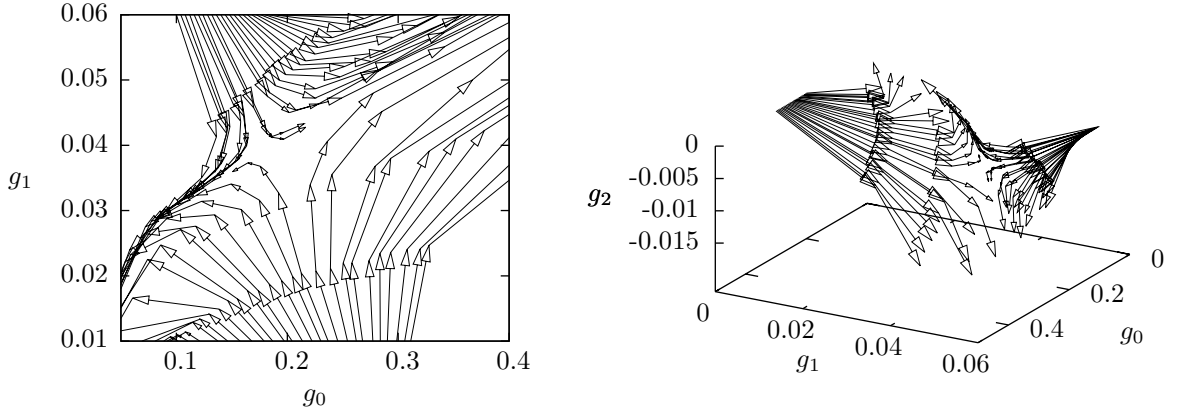


Figure 9: Using a shooting technique, the RG trajectories for the $3 \rightarrow 3$ truncation with operators S_0 , S_1 and S_2 on a 32^3 lattice with $N = 3$ reveal an analogous structure to the $2 \rightarrow 2$ case. The projection on the g_0 - g_1 axis in the left panel indicates only a single relevant direction at the non-Gaussian fixed point. The right panel shows that the trajectories first approach the fixed point regime and afterwards flow along the renormalized trajectory to the respective IR fixed point.

For the operators $\{S_0, S_1, S_3\}$, the resulting flow diagram is very similar. In fact, even the position of the fixed point is identical to (2.40) within error bars. Finally, Figure 10 shows the $4 \rightarrow 4$ truncation. A further irrelevant direction is added and the fixed point structure remains unchanged. The position of the NG FP is at

$$g_0^* = 0.13(1), \quad g_1^* = 0.016(1), \quad g_2^* = -0.0015(5) \quad \text{and} \quad g_3^* = -0.0015(5). \quad (2.41)$$

The fixed point couplings g_0^* , g_1^* and g_2^* do not change compared to (2.40) and the value for g_3^* is two orders of magnitude below g_0^* . In conclusion, the fixed point structure does not change if further operators are added. The non-Gaussian fixed point is always characterized by a single relevant direction. In addition, the position of the NG FP is stable against the inclusion of higher derivative operators. Thus, the asymptotic safety scenario clearly applies to the $O(3)$ nonlinear Sigma model in three dimensions.

The present work is mainly concerned with the flow diagram and fixed point structure of nonlinear $O(N)$ models. However, it is further possible to measure the critical exponents θ^α (2.15). Of course, the MCRG demon method is not to be seen as a replacement of dedicated high-precision Monte Carlo methods that

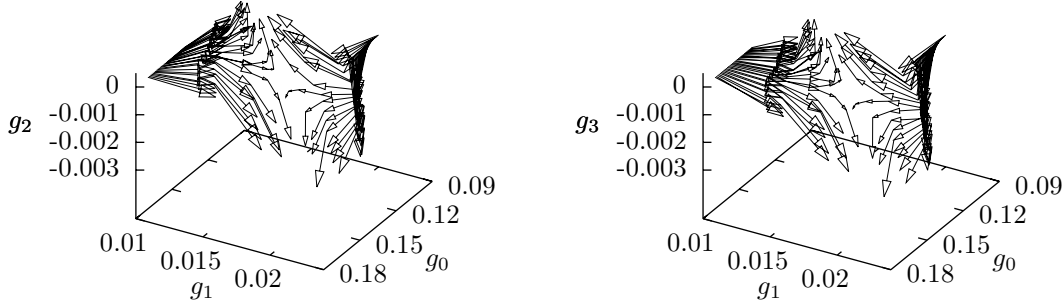


Figure 10: The $\{S_0, S_1, S_2\}$ and $\{S_0, S_1, S_3\}$ projections of the flow diagram in the vicinity of the non-Gaussian fixed point for the $4 \rightarrow 4$ truncation on a 32^3 lattice with $N=3$ are shown. The NG FP is characterized by one relevant and three irrelevant directions.

focus solely on the determination of critical exponents. Rather, the objective of the next section is to provide a reasonable estimate such that the universality class can be confirmed. We expect it to be of Wilson-Fisher type.

2.9.3 Critical exponents

It is generally assumed that the linear and nonlinear $O(N)$ models are in the same universality class since they have the same range of interaction and symmetries. This assumption is supported by several computations based on very different approximations [5, 50, 69–71]. In contrast to the position of the fixed point, critical exponents are universal. Thus, a verification of our results independent of the renormalization scheme is possible. Here, we restrict ourselves to the scaling properties of the correlation length, described by the thermodynamical critical exponent ν . It is directly related to the critical exponent θ^r by $\nu = 1/\theta^r$.

Using the simple $1 \rightarrow 1$ truncation, ν^{-1} corresponds to the negative slope of the lattice beta function in the vicinity of a fixed point. We find the trivial exponent $\nu \approx -1$ for the high-temperature and $\nu \approx 1$ for the low-temperature fixed point. These values do not depend on the optimization parameter. In contrast, the critical exponent at the NG FP varies with c_0 (see Figure 11). Since ν is not scheme-dependent, the variation w.r.t the optimization constant

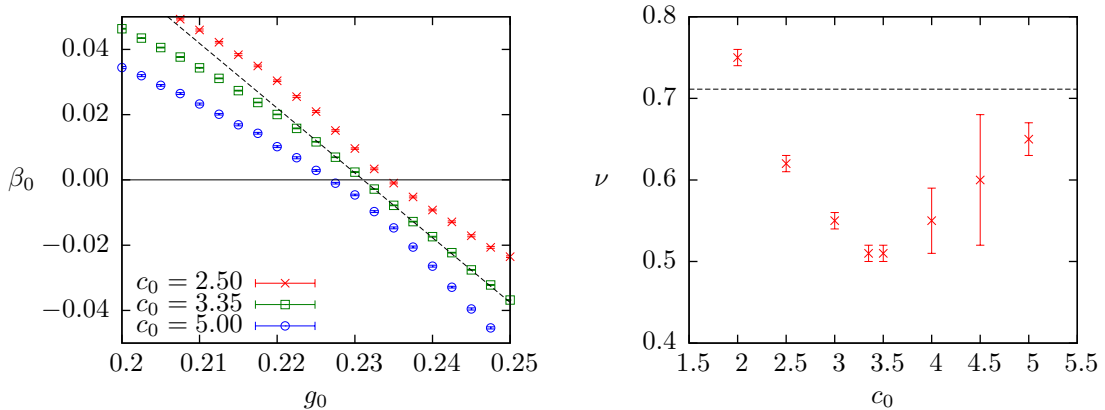


Figure 11: The left panel shows the $1 \rightarrow 1$ beta function in the vicinity of the NG FP on a 32^3 lattice for $N = 3$. The slope of β_0 corresponds to the critical exponent ν (right panel) and depends on the optimization constant.

is entirely due to systematic uncertainties that originate from truncation. By a careful optimization of the blockspin transformation, these errors are minimized. Using the optimal constant $c_0 = 3.35$, we read off

$$\nu(1 \rightarrow 1) = 0.51(1) \quad (2.42)$$

for $N = 3$. This is to be compared with the value $0.7112(5)$ [29]. Of course we cannot expect to obtain high precision results with the simplest possible ansatz for the effective action. An improvement is gained by allowing a second operator. The critical exponent θ^r for the $2 \rightarrow 2$ truncation is depicted in Figure 12 (left panel). Again, it takes trivial values $\theta^r \approx -1$ for vanishing coupling (high-temperature fixed point). For infinite coupling, it is evident that $\theta^r \approx 1$. While the plot shows local fluctuations of θ^r in the upper left and lower right corner of the parameter space, it becomes flat in the vicinity of the non-trivial fixed point. The value

$$\nu(2 \rightarrow 2) = 0.62(3) \quad (2.43)$$

is computed by averaging over the fixed point regime. It deviates less than 15% from the literature value and is considerably closer than $\nu(1 \rightarrow 1)$. The error is estimated by the standard deviation of the averaging procedure. It is further possible to extract the critical exponent corresponding to the irrelevant direction of the flow (see Figure 12, right panel). It takes the value $\theta^{\text{ir}} \approx -1$ at the

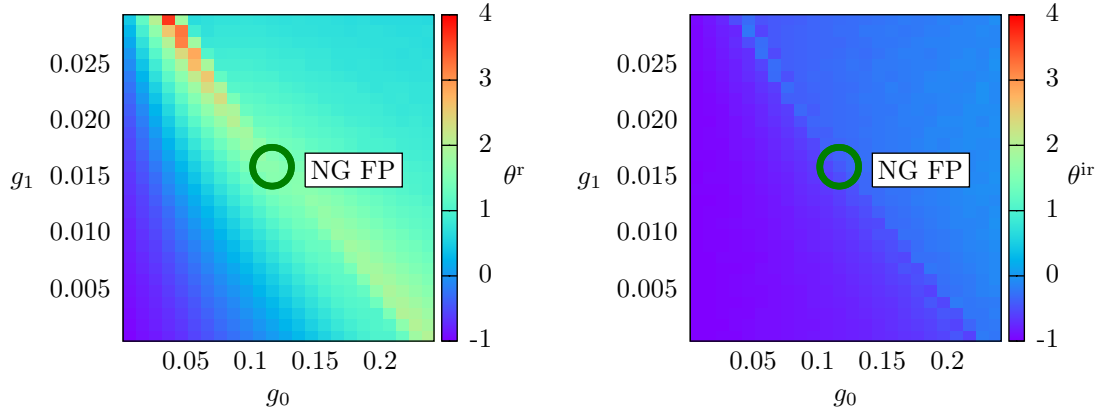


Figure 12: The critical exponent ν is related to the eigenvalue θ^r (left panel) of the stability matrix corresponding to the relevant direction. The critical exponent of the irrelevant direction (left panel) is negative at the high temperature and non-Gaussian fixed point. The RG parameters for this flow diagram are $c_0 = 3.1$ and $c_1 = 2.5$.

high-temperature fixed point and $\theta^{\text{ir}} \approx 0$ at the low-temperature fixed point. As expected, it is negative at the non-Gaussian fixed point: $\theta^{\text{ir}} \approx -0.44$. The critical line is clearly visible as a separatrix that divides the trivial fixed point regimes. For the $3 \rightarrow 3$ truncation, it is sufficient to choose $c_2 = 0$, while the other optimization constants are $c_0 = 3.1$ and $c_1 = 2.5$. The exponent of the correlation length is

$$\nu(3 \rightarrow 3) = 0.64(3) \quad (2.44)$$

and the irrelevant directions yield

$$\theta^{\text{ir},1} = -0.52 + 0.05i \quad \text{and} \quad \theta^{\text{ir},2} = -0.86 - 0.05i. \quad (2.45)$$

The imaginary part is very small and still consistent with zero due to statistical uncertainties. Going to even higher truncations, the computation of critical exponents becomes very time consuming. One is obliged to perform parameter scans in every direction of theory space in order to determine the fixed point location and stability matrix (2.14). Since the latter is a second order derivative, small stepsizes are needed for the scans such that discretization errors are small. Furthermore, the optimization of the blockspin transformation becomes increasingly difficult as the number of parameters grows. Therefore, we regard the $3 \rightarrow 3$

truncation as our best estimate for the present analysis.

In conclusion, the high temperature fixed point shows only irrelevant directions, i.e. all critical exponents are negative. Those corresponding to the operators S_0 and S_1 take the value $\theta^0 = \theta^1 = -1$. Just as expected from the detailed evaluation of the flow diagram, the non-Gaussian fixed point is characterized by a positive critical exponent corresponding to S_0 . The remaining θ are negative. Therefore, the asymptotic safety scenario is verified once again. Table [1](#) summarizes the results for the critical exponents. With increasing truncation order,

Method	ν	$(\nu - \nu_{MC})/\nu_{MC}$
1 \rightarrow 1 trunc.	0.51(1)	0.28
2 \rightarrow 2 trunc.	0.62(3)	0.13
3 \rightarrow 3 trunc.	0.64(3)	0.10
MC	0.7112(5)	0.00
HT	0.715(3)	0.01

Table 1: Results for the critical exponent ν of the $N = 3$ model for different truncations. The comparative data originate from Monte Carlo simulations with an adapted high-temperature expansion (MC) [\[29\]](#) and plain high-temperature expansions (HT) [\[50\]](#).

the critical exponent approaches comparative data, indicating that the derivative expansion converges. Although the best estimate for ν still deviates by 10% from the literature value, we are confident that our results correctly attribute the non-Gaussian UV fixed point to the Wilson-Fisher universality class. In the next section, this investigation is extended to large N .

2.10 The large N limit

For large values of N , we can compare our results with the analytical large N expansion [\[72\]](#). Hence, we repeat the computation of the critical exponent ν in the simple 1 \rightarrow 1 truncation for N up to 10. For every value of N , a non-trivial fixed point exists and the results are shown in Figure [13](#) (left panel). Starting from $N = 2$, where the estimate deviates from the comparative data by 40%, we see an improvement for intermediate $N < 8$. However, going to even larger N , the behaviour changes and our results significantly underestimate the literature

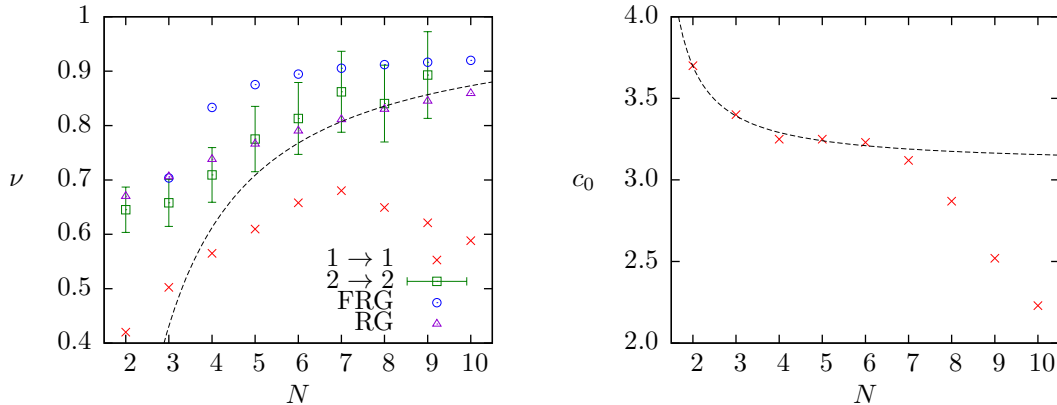


Figure 13: The critical exponent ν (left panel) is shown for the $1 \rightarrow 1$ and $2 \rightarrow 2$ truncation depending on N . We compare our data to results using the functional RG [49] and RG expansions [52]. the dashed line corresponds to the large N expansion up to second order [72]. In the $N \rightarrow \infty$ limit, $\nu = 1$ is expected. The right panel depicts the optimization function $c_0(N)$ for the $1 \rightarrow 1$ truncation. The dashed line is a fit to the asymptotic behaviour (2.46) for $N \leq 6$.

values. It is evident that we do not reproduce the analytically known result of $\nu = 1$ for $N \rightarrow \infty$.

This change of behaviour is not limited to the critical exponent. In this section, the optimization “constant” c_0 is determined separately for each N and thus becomes a function of the target space. From the perturbative analysis [59], it is known that the asymptotic behaviour is given by

$$c_0(N) \sim \frac{N}{N-1}, \quad (2.46)$$

i.e. we expect $c_0(N)$ to become constant for large N . Indeed, Figure 13 (right panel) shows a plateau for intermediate N . Unfortunately, going to $N > 7$, the optimization function decreases rapidly. We interpret this unexpected behaviour as a breakdown of the simple one-parameter truncation. The optimization scheme becomes *pointless* if the ansatz for the effective action no longer captures the important physics. In this case, one cannot expect to find reliable values for the critical exponents. Although it is still achievable to tune the ratio of two-point functions, this is no longer sufficient. Considering higher correlation functions, one should realize that it is not possible to simultaneously tune all of them to the desired value. The only way to improve the situation is by including higher-order

operators. For the $2 \rightarrow 2$ truncation, we have computed the critical exponents up to $N=9$. Indeed, the results are much closer to the comparative data (see Figure 13, left panel). Following a pragmatic approach, we have fitted the asymptotic behaviour (2.46) to the optimized parameters $c_0(N)$ for $N \leq 6$. The “plateau values” given by the fit were used as optimization constants for $N > 6$. The ratio of correlation lengths is close to the optimal value if we further choose $c_1 = 1.0$ for all N . While the general structure of the flow diagram persists for different N (see Figure 14), the non-universal location of the non-Gaussian fixed point varies. However, even in the $2 \rightarrow 2$ case, it is evident that the truncation

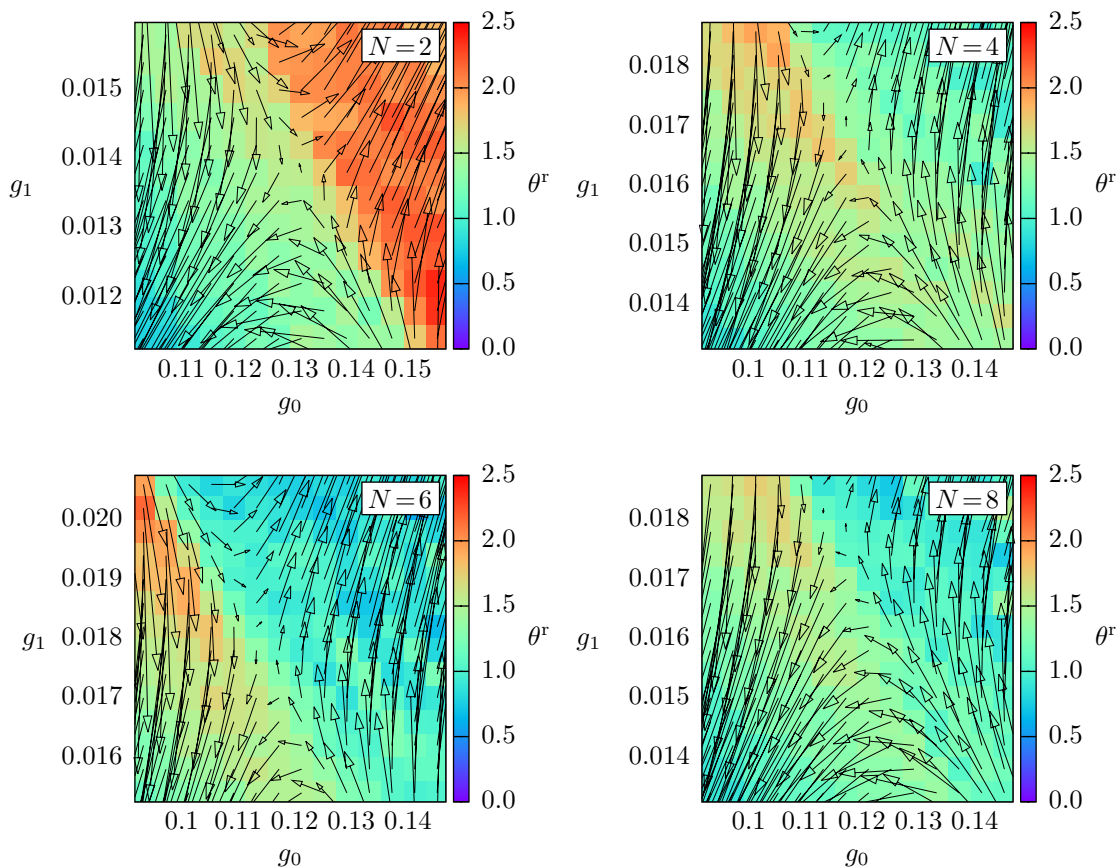


Figure 14: The flow diagram of the $O(2)$, $O(4)$, $O(6)$ and $O(8)$ model is shown in the $2 \rightarrow 2$ truncation on a 32^3 lattice. The global structure is identical to the $O(3)$ model. The background color depicts the critical exponent θ^r .

breaks down for $N > 9$. Again, additional operators are needed to obtain reliable results for the critical exponents. Furthermore, tuning of the RG parameter and the computation of critical exponents becomes increasingly difficult for large N .

This is in part due to the scaling of the simulation time with N . Our final results are compiled in Table 2.

N	2	3	4	5	6	8
1 \rightarrow 1 trunc.	0.42	0.51	0.57	0.63	0.65	0.65
2 \rightarrow 2 trunc.	0.64(4)	0.66(4)	0.71(5)	0.78(6)	0.81(6)	0.84(7)
FRG	-	0.704	0.833	-	0.895	0.912
RG exp.	0.607	0.706	0.738	0.766	0.790	0.830

Table 2: Results for the critical exponent ν for different N . The comparative data is obtained from functional renormalization group calculations (FRG) [49] and renormalization group expansions (RG) [52].

2.11 Conclusion

We have discussed and applied a method that allows to compute the global flow diagram from numerical simulations. In contrast to the well-known MCRG matching technique, the MCRG demon method does not need exponentially large lattices and works even if the renormalized trajectory does not act as an attractor for the RG flow. However, systematic uncertainties from a truncation of the effective action greatly affect predictions from the renormalization group. In order to complete the method, it was absolutely necessary to construct a non-perturbative optimization scheme. In the present work, such a scheme was put forward and shown to efficiently mitigate truncation errors.

The nonlinear $O(N)$ Sigma model is asymptotically free in two dimensions. We have reproduced the beta function, showing two trivial fixed points corresponding to very low and very high temperature. Using a two-operator truncation, the role of finite volume effects on the flow diagram was clarified. In particular, an additional non-trivial fixed point was identified as a lattice artifact.

It has long been known that the three-dimensional $O(3)$ model exhibits a second-order phase transition. We have shown that it corresponds to an ultraviolet fixed point with a *single* relevant direction. Our largest truncation included all possible operators up to fourth order in the momentum. The theory that corresponds to the renormalized trajectory is IR- and UV-complete. We conclude that the asymptotic safety scenario is fulfilled. Thus, the model is renormalizable in a non-perturbative setting.

While the general structure of the flow diagram is independent of the specific RG transformation, the critical exponents differ. This does not contradict their universality. It is simply the consequence of the dependence of systematic errors on the RG transformation. These errors are mitigated by the optimization scheme. We are able to predict the critical exponents within a reasonable accuracy but can not compete with designated high precision MC-techniques that are free of truncation errors. While the estimate for the critical exponents improves for larger truncations, it is troublesome that the exact $N \rightarrow \infty$ limit is not reproduced for a fixed truncation. Rather, more and more operators seem to be necessary. However, a similar behaviour was noticed previously in functional renormalization group calculations [49]. The structure of the flow diagram is identical. Yet, the MCRG method proves to be more stable and leads to more robust results for different truncations. In particular, the FRG encountered a sudden disappearance of the non-trivial fixed point for a truncation including the operator S_2 (2.32). This was not the case for the MCRG demon method. Nevertheless, results from the FRG fail to match the $N \rightarrow \infty$ limit as well. It is thus concluded that, contrary to naive intuition, the analytically known large N results are accessible only to a complicated effective action, including operators of increasing orders of derivatives.

With regard to functional methods, we stress that lattice techniques provide the opportunity to obtain additional information beyond the chosen truncation by a direct measurement of correlation functions. We have actively used this knowledge to determine the optimal constants in the improved RG transformation.

3 Continuum limit of the supersymmetric Sigma Model

3.1 Supersymmetry

High energy experiments at particle colliders like the LHC at CERN⁵ are accurately described by the Standard Model of particle physics (SM) [8]. It is based on the principle of local gauge invariance, incorporating the idea of *symmetries*. They play a pivotal role in modern elementary particle physics. If a symmetry is recognized from experiments, strict constraints can be deduced for the corresponding theoretical model. For example, this approach has led to the postulation of quarks [73]. They are described by quantum Chromodynamics (QCD), the theory of strong interaction.

However, the Standard Model still faces serious problems with regard to cosmological observations. One has recognized that the balance of observed matter on the one hand and gravitational attraction on the other hand is uneven [74]. A popular loophole is found by the postulation of yet undiscovered sources of gravitation, the so-called *dark matter* [75]. Since the Standard Model does not include any dark matter, *beyond the Standard Model (BSM)* theories are needed. Another interesting question concerns the existence of far more matter than antimatter in our universe. This fact is connected to the *strong CP problem* [76]. Lastly, the *hierarchy problem* [77] is connected to the Higgs sector of the SM. Through renormalization, bare parameters are related to the experimental values. The mass of the Higgs boson receives large quantum corrections from all virtual particles coupling to the Higgs field. Thus, the bare mass must be chosen extremely careful in order to reproduce the experiment. This raises a question of naturalness: is such a fine tuning acceptable of a fundamental theory? To address these open issues, many BSM theories have been proposed. Among them are the supersymmetrically extended versions [78], in particular the Minimal Supersymmetric Standard Model (MSSM).

In fact, *supersymmetry (susy)* is the only possible extension of the Poincaré symmetry [79]. It relates bosonic and fermionic degrees of freedom, leading to profound implications for the spectrum of supersymmetric theories. For each par-

⁵See <http://home.web.cern.ch/> for recent updates on the CERN laboratory.

ticle, a superpartner exists with equal mass and quantum numbers, but different spin. This is a direct consequence of the supersymmetry algebra

$$\{Q_\alpha^I, \bar{Q}_\beta^J\} = 2\delta^{IJ}\gamma_{\alpha\beta}^\mu P_\mu, \quad I, J = 1, \dots, \mathcal{N}, \quad (3.1)$$

where Q^I are the supercharges. However, none such superpartners have been found in nature so far. Thus, supersymmetry must be broken. In this case, the masses of the corresponding superpartners can be considerably larger. Besides, they provide excellent candidates for dark matter. For additional details, the reader is directed to the reviews on supersymmetry in [80, 81] and the textbooks [82, 83].

In the past, two-dimensional nonlinear Sigma models have been applied successfully to model non-perturbative properties of four-dimensional strongly coupled pure gauge theories [84]. Similarly, one may employ the supersymmetrized version of the nonlinear Sigma model to effectively describe super-Yang-Mills theories with a strongly interacting fermionic sector. It is of great interest to examine the non-perturbative properties of these theories. However, the utilization of the only ab initio method for this purpose, namely a lattice simulation, is notoriously difficult.

3.2 ... on the lattice?

Supersymmetry is an extension of the Poincaré symmetry. Hence, any discretization of space-time that breaks the latter also breaks supersymmetry. This can be traced back to the failure of the Leibniz rule on the lattice [85]. However, whereas the Poincaré symmetry is restored in the continuum limit from the residual lattice symmetries, e.g. finite translations by multiples of the lattice spacing, this is usually not true for supersymmetry. The discretized model is not supersymmetric and the renormalization of susy-breaking operators is thus not forbidden. If these operators are relevant, they will carry the effective action away from a possible supersymmetric fixed point and supersymmetry is not restored in the continuum.

In general, one must introduce appropriate counterterms for each relevant susy-breaking operator and fine tune them such that the desired continuum theory is approached [86, 87]. Depending on the number of parameters this becomes

practically impossible due to limited computer time. In addition, much information about the theory is needed prior to numerical investigations. Therefore, alternative approaches have been proposed in order to reduce the number of fine tuning parameters or even render the fine tuning procedure obsolete [88]. One approach for theories with extended supersymmetry aims at the construction of a nilpotent charge. The latter is composed of the supercharges such that both the continuum as well as the discretized model are invariant under this charge. It is then expected that, by preserving a part of the symmetry, invariance under full supersymmetry is restored automatically in the continuum limit, without fine tuning. The residual supersymmetry protects the theory from the renormalization of susy-breaking operators.

This procedure had been applied to the supersymmetric nonlinear $O(3)$ model [89, 90] and the authors conclude that supersymmetric Ward identities are indeed fulfilled in the continuum limit, indicating the restoration of full supersymmetry. However, the lattice discretization constructed this way breaks the $O(3)$ symmetry of the target space explicitly at finite lattice spacing. No attempt was made to show that it is restored in the continuum limit. In fact, it was proven [25] that this is not the case and the proposed discretization must be rejected. Using the SLAC derivative, an alternative $O(3)$ invariant discretization was investigated. Though the discrete model breaks supersymmetry on the lattice, it is restored in the continuum limit. Unfortunately, since the sign of the configuration weight fluctuates strongly, these results were confined to small lattices.

In this chapter, we will present simulations using Wilson fermions and another $O(3)$ invariant discretization. They offer the possibility to explore larger lattices and may provide complementary results regarding the continuum limit. This chapter is organized as follows: First, we introduce the supersymmetric version of the nonlinear $O(3)$ model and discuss previous attempts of discretization schemes. After an outline of our approach, which uses a stereographic projection to handle the constraints, extensive numerical investigations are presented. Particular emphasis is drawn to the symmetries of the theory. We conclude with an answer to the question whether supersymmetry is restored in the continuum limit.

3.3 Supersymmetric nonlinear O(3) Sigma model

A first construction of the supersymmetric nonlinear Sigma model with O(N) target manifold is due to E. Witten [91] and P. Di Vecchia and S. Ferrara [92]. Subsequent papers established analytical properties like asymptotic freedom, spontaneous breaking of chiral symmetry and dynamical generation of particle masses [93, 94]. The classical theory has no intrinsic mass scale, but there is a relation between mass gap and bare coupling by dimensional transmutation. In the $\overline{\text{MS}}$ scheme it is possible to compute the mass gap in relation to $\Lambda_{\overline{\text{MS}}}$ [95, 96]. Further studies are particularly concerned with the special case of the O(3) model, since it admits an extended $\mathcal{N}=2$ supersymmetry algebra.

The supersymmetric extension of the two-dimensional nonlinear O(N) sigma model in Euclidean space-time can be formulated in terms of a real superfield⁶,

$$\Phi = \mathbf{n} + i\bar{\theta}\psi + \frac{i}{2}\bar{\theta}\theta\mathbf{f} \quad (3.2)$$

subject to the constraint $\Phi\Phi = 1$. Here, θ^α is a Grassmann number, \mathbf{n} and \mathbf{f} denote N -tuples of real scalar fields and ψ is an N -tuple of Majorana fields. We shall refer to the elements of a tuple as ‘‘flavors’’. The constraint in superspace entails the constraints,

$$\mathbf{n}^2 = 1, \quad \mathbf{n}\psi = 0 \quad \text{and} \quad \mathbf{n}\mathbf{f} = \frac{i}{2}\bar{\psi}\psi. \quad (3.3)$$

for the component fields \mathbf{n} , ψ and \mathbf{f} . The O(N) invariant Lagrangian density is defined in terms of the covariant derivatives

$$D_\alpha = \partial_{\bar{\theta}^\alpha} + i(\gamma^\mu\theta)_\alpha\partial_\mu \quad \text{and} \quad \bar{D}_\alpha = -\partial_{\theta^\alpha} - i(\bar{\theta}\gamma^\mu)_\alpha\partial_\mu. \quad (3.4)$$

It reads:

$$\mathcal{L} = \frac{1}{2g^2} \overline{D\Phi} D\Phi|_{\bar{\theta}\theta} = \frac{1}{2g^2} (\partial_\mu\mathbf{n}\partial^\mu\mathbf{n} + i\bar{\psi}\not{\partial}\psi - \mathbf{f}^2). \quad (3.5)$$

⁶We choose the Majorana representation $\gamma_0 = \sigma_3$, $\gamma_1 = -\sigma_1$, $\gamma_* = i\gamma_0\gamma_1 = \sigma_2$, $C = -i\sigma_2$, and the conjugate spinor is defined as $\bar{\chi} = \chi^T C$. We employ the Fierz relation $\psi\bar{\chi} = -\frac{1}{2}\bar{\chi}\psi - \frac{1}{2}(\bar{\chi}\gamma^\mu\psi)\gamma_\mu - \frac{1}{2}(\bar{\chi}\gamma_*\psi)\gamma_*$. Due to the symmetry properties $\bar{\chi}\psi = \bar{\psi}\chi$, $\bar{\chi}\gamma^\mu\psi = -\bar{\psi}\gamma^\mu\chi$ and $\bar{\chi}\gamma_*\psi = -\bar{\psi}\gamma_*\chi$ the two last terms vanish for $\chi = \psi$ such that $\psi\bar{\psi} = -\frac{1}{2}\bar{\psi}\psi\mathbb{1}$.

Thus, the partition function is given by

$$\mathcal{Z} = \int \mathcal{D}\mathbf{n} \mathcal{D}\boldsymbol{\psi} \mathcal{D}\mathbf{f} \delta(\mathbf{n}^2 - 1) \delta(\mathbf{n}\boldsymbol{\psi}) \delta(\mathbf{n}\mathbf{f} - \frac{i}{2} \bar{\boldsymbol{\psi}}\boldsymbol{\psi}) e^{-S[\mathbf{n}, \boldsymbol{\psi}, \mathbf{f}]} \quad (3.6)$$

with $S[\mathbf{n}, \boldsymbol{\psi}, \mathbf{f}] = \int d^2x \mathcal{L}[\mathbf{n}, \boldsymbol{\psi}, \mathbf{f}]$. The equation of motion for the auxiliary field \mathbf{f} implies that \mathbf{f} and \mathbf{n} are parallel, $\mathbf{f} = \frac{i}{2}(\bar{\boldsymbol{\psi}}\boldsymbol{\psi})\mathbf{n}$, and the resulting on-shell Lagrangian density,

$$\mathcal{L} = \frac{1}{2g^2} (\partial_\mu \mathbf{n} \partial^\mu \mathbf{n} + i \bar{\boldsymbol{\psi}} \not{\partial} \boldsymbol{\psi} + \frac{1}{4} (\bar{\boldsymbol{\psi}}\boldsymbol{\psi})^2), \quad (3.7)$$

contains a four-fermi term. The action and the constraints are both invariant under global $O(N)$ ‘‘flavor’’ transformations. By construction, they are also invariant under the $\mathcal{N}=1$ supersymmetry transformations

$$\delta \mathbf{n} = i \bar{\boldsymbol{\psi}} \boldsymbol{\psi}, \quad \delta \boldsymbol{\psi} = (\not{\partial} + \frac{i}{2} \bar{\boldsymbol{\psi}}\boldsymbol{\psi}) \mathbf{n} \boldsymbol{\epsilon}. \quad (3.8)$$

Besides flavor symmetry and supersymmetry, the classical theory admits a further \mathbb{Z}_2 -symmetry, generated by the chiral transformation $\boldsymbol{\psi} \rightarrow i\gamma_* \boldsymbol{\psi}$. However, quantum fluctuations dynamically generate a mass term and hence induce spontaneous breaking of the chiral \mathbb{Z}_2 -symmetry.

The special case $N = 3$ allows for an extended $\mathcal{N}=2$ supersymmetry since its target manifold is Kähler [97]. One finds the simple transformations

$$\begin{aligned} \delta \mathbf{n} &= \mathbf{a} \times \bar{\boldsymbol{\psi}} \boldsymbol{\psi} \\ \delta \boldsymbol{\psi} &= -\mathbf{n} \times \partial_\mu \mathbf{n} \gamma^\mu \boldsymbol{\epsilon} - i \bar{\boldsymbol{\psi}} \boldsymbol{\psi} \times \boldsymbol{\psi}, \end{aligned} \quad (3.9)$$

where $\mathbf{a} \times \mathbf{b}$ denotes the vector product of \mathbf{a} and \mathbf{b} . The two on-shell supersymmetries (3.8, 3.9) are generated by the supercharges

$$\mathcal{Q}_I = i \int \gamma^\mu \gamma^0 \partial_\mu \mathbf{n} \boldsymbol{\psi} \quad , \quad \mathcal{Q}_{II} = -i \int \gamma^\mu \gamma^0 (\mathbf{n} \times \partial_\mu \mathbf{n}) \boldsymbol{\psi}. \quad (3.10)$$

3.4 Discretization and residual symmetries

So far, $O(N)$ Sigma models in the continuum have been considered. In order to investigate the corresponding lattice models, one should try to discretize it

such that as many symmetries of the continuum theory as possible are preserved. Maintaining supersymmetry is difficult to realize, but also the flavor symmetry must be treated with care. We start with a formulation in terms of constrained fields, whose discretization is manifestly $O(N)$ invariant:

$$S[\mathbf{n}, \boldsymbol{\psi}] = \frac{1}{2g^2} \sum_{x,y} \left(\mathbf{n}_x^\top K_{xy} \mathbf{n}_y + i \bar{\boldsymbol{\psi}}_x^\alpha M_{xy}^{\alpha\beta} \boldsymbol{\psi}_y^\beta + \frac{1}{4} (\bar{\boldsymbol{\psi}}_x \delta_{xy} \boldsymbol{\psi}_y)^2 \right). \quad (3.11)$$

The subscripts x, y denote lattice sites, while α, β indicate spinor indices. The lattice derivatives K_{xy} and $M_{xy}^{\alpha\beta}$ are proportional to the identity in flavor space. The constraints $\mathbf{n}_x \mathbf{n}_x = 1$ and $\mathbf{n}_x \boldsymbol{\psi}_x = 0$ must be fulfilled at each lattice point x . They are implemented as delta-functions in the path integral measure. This causes some difficulties in numerical simulations. One can cope with this problem by applying the stereographic projection, which is discussed in the next chapter.

3.4.1 Stereographic projection

It is useful to construct a formulation of the model in terms of an unconstrained real superfield $\mathbf{U}(x, \theta) = \mathbf{u}(x) + i\bar{\theta}\boldsymbol{\lambda}(x) + \frac{1}{2}\bar{\theta}\theta\mathbf{g}(x)$, which forming an $(N-1)$ -tuple. It is related to the superfield $\boldsymbol{\Phi}$ by a stereographic projection in superspace:

$$\begin{pmatrix} \Phi_1 \\ \boldsymbol{\Phi}_\perp \end{pmatrix} = \frac{1}{1 + \mathbf{U}^2} \begin{pmatrix} 1 - \mathbf{U}^2 \\ 2\mathbf{U} \end{pmatrix}. \quad (3.12)$$

The decomposition of the projection into bosonic and fermionic fields reads:

$$\mathbf{n}_\perp = 2\rho \mathbf{u}, \quad \boldsymbol{\psi}_\perp = 2\rho\boldsymbol{\lambda} - 4\rho^2 (\mathbf{u}\boldsymbol{\lambda})\mathbf{u} \quad \text{with} \quad \rho = \frac{1}{1 + \mathbf{u}^2}. \quad (3.13)$$

The expressions for the remaining components n_1 and ψ_1 can be determined either from (3.12) or from (3.13) via the constraints $\mathbf{n}^2 = 1$ and $\mathbf{n}\boldsymbol{\psi} = 0$. The inverse transformation in superspace reads $\mathbf{U} = \boldsymbol{\Phi}_\perp / (1 + \Phi_1)$ and leads to

$$\mathbf{u} = \frac{1}{2\rho} \mathbf{n}_\perp, \quad \boldsymbol{\lambda} = \frac{1}{2\rho} \boldsymbol{\psi}_\perp - \frac{1}{4\rho^2} \psi_1 \mathbf{n}_\perp \quad \text{with} \quad \rho = \frac{1 + n_1}{2}. \quad (3.14)$$

Applying the stereographic projection (3.13), the on-shell Lagrangian density can be written in terms of the unconstrained fields as

$$\mathcal{L} = \frac{2}{g^2} \rho^2 (\partial_\mu \mathbf{u} \partial^\mu \mathbf{u} + i \bar{\lambda} \not{\partial} \lambda + 4i\rho (\bar{\lambda} \mathbf{u}) \gamma^\mu (\partial_\mu \mathbf{u} \lambda) + \rho^2 (\bar{\lambda} \lambda)^2). \quad (3.15)$$

The action is now invariant under the supersymmetry transformations

$$\delta \mathbf{u} = i \bar{\epsilon} \lambda, \quad \delta \lambda = (\not{\partial} + i\rho \bar{\lambda} \lambda) \mathbf{u} \epsilon - 2i\rho (\bar{\lambda} \mathbf{u}) \lambda \epsilon. \quad (3.16)$$

The stereographic projection (3.13) resolves both constraints and leads to an unconstrained but yet O(N) -symmetric lattice formulation. The discretized action takes the form $S(\{\mathbf{u}_x, \lambda_x\}) = S_B + S_{2F} + S_{4F}$ with

$$S_B = \frac{1}{2g^2} \sum_{x,y} 4\rho_x \mathbf{u}_x^T K_{xy} \mathbf{u}_y \rho_y + \rho_x (1 - \mathbf{u}_x^2) K_{xy} (1 - \mathbf{u}_y^2) \rho_y, \quad (3.17)$$

$$S_{2F} = \frac{2i}{g^2} \sum_{x,y;\alpha,\beta} \bar{\lambda}_x^\alpha \left[(\rho - 2\rho^2 \mathbf{u} \mathbf{u}^T)_x M_{xy}^{\alpha\beta} (\rho - 2\rho^2 \mathbf{u} \mathbf{u}^T)_y + 4 (\rho^2 \mathbf{u})_x M_{xy}^{\alpha\beta} (\rho^2 \mathbf{u}^T)_y \right] \lambda_y^\beta, \quad (3.18)$$

$$S_{4F} = \frac{2}{g^2} \sum_x \rho_x^4 (\bar{\lambda}_x \lambda_x)^2. \quad (3.19)$$

The transformation from the constrained fields $(\mathbf{n}, \boldsymbol{\psi})$ to the unconstrained fields (\mathbf{u}, λ) yields a non-trivial Jacobian:

$$\prod_{x,\alpha} d\mathbf{n}_x d\boldsymbol{\psi}_x^\alpha \delta(\mathbf{n}_x^2 - 1) \delta(\mathbf{n} \boldsymbol{\psi}^\alpha) \longrightarrow \prod_{x,\alpha} d\mathbf{u}_x d\lambda_x^\alpha (1 + \mathbf{u}_x^2)^{N-1}. \quad (3.20)$$

The four-fermion interaction can be eliminated by employing the usual Hubbard-Stratonovich transformation [98], introducing an auxiliary bosonic field σ :

$$S(\{\mathbf{u}_x, \lambda_x, \sigma_x\}) = S_B + S_{2F} + \frac{1}{2g^2} \sum_x (\sigma_x^2 + 4i\sigma_x \rho_x^2 \bar{\lambda}_x \lambda_x). \quad (3.21)$$

An integration over Grassmann variables leads to the bosonic path integral

$$\mathcal{Z} = \int \prod_x d\mathbf{u}_x d\sigma_x \text{sgn Pf } Q e^{-S_{\text{eff}}}. \quad (3.22)$$

Here, the effective bosonic action is defined as

$$S_{\text{eff}}(\{\mathbf{u}_x, \sigma_x\}) = S_B + \sum_x \left(\frac{1}{2g^2} \sigma_x^2 - (N-1) \log(1 + \mathbf{u}_x^2) \right) - \log |\text{Pf } Q|, \quad (3.23)$$

where Q is the fermion matrix

$$Q_{xy,ij}^{\alpha\beta} = 4\rho_x (\delta_{ik} - 2u_{x,i}u_{x,k}\rho_x) M_{xy}^{\alpha\beta} (\delta_{kj} - 2u_{y,k}u_{y,j}\rho_y) \rho_y \\ + 16\rho_x^2 u_{x,i} M_{xy}^{\alpha\beta} u_{y,j} \rho_y^2 + 4\beta \rho_x^2 \sigma_x \delta_{xy} \delta_{ij} \delta^{\alpha\beta}. \quad (3.24)$$

In practical simulations, the effective fermionic action is rewritten according to $\log |\text{Pf } Q| = \frac{1}{2} \log \det Q$ and the hybrid Monte Carlo algorithm is used. A detailed discussion of the Pfaffian sign is given in chapter [3.6](#).

We are particularly interested in the chiral condensate, which is an order parameter for spontaneous chiral symmetry breaking, and the masses of the bosonic and fermionic fields. The fermionic correlator for the different flavor components is constructed as

$$\langle i\bar{\psi}_{x,\perp} \psi_{y,\perp} \rangle = \langle 4\rho_x i\bar{\lambda}_x \lambda_y \rho_y - 8\rho_x (\mathbf{u}_x i\bar{\lambda}_x) (\lambda_y \mathbf{u}_y) \rho_y^2 - 8\rho_x^2 (\mathbf{u}_x i\bar{\lambda}_x) (\lambda_y \mathbf{u}_y) \rho_y \\ + 16\rho_x^2 (\mathbf{u}_x i\bar{\lambda}_x) (\mathbf{u}_x \mathbf{u}_y) (\lambda_y \mathbf{u}_y) \rho_y^2 \rangle, \\ \langle i\bar{\psi}_{x,1} \psi_{y,1} \rangle = \langle 16\rho_x^2 (\mathbf{u}_x i\bar{\lambda}_x) (\lambda_y \mathbf{u}_y) \rho_y^2 \rangle. \quad (3.25)$$

If the $O(N)$ symmetry is intact, all correlators lie on top of each other and we do not need to discriminate flavor. The corresponding timeslice correlator is given by $C_F(t) = N_s^{-2} \sum_{xy} \langle i\bar{\psi}_{(t,x)} \psi_{(0,y)} \rangle$. Using these definitions, the fermionic masses are obtained by a cosh fit to the correlator over the range $t \in]0, N_t[$. In a similar fashion, the bosonic masses are extracted by calculating the stereographically projected correlators

$$\langle \mathbf{n}_{x,\perp} \mathbf{n}_{y,\perp} \rangle = 4 \langle \rho_x \mathbf{u}_x \mathbf{u}_y \rho_y \rangle, \\ \langle n_{x,1} n_{y,1} \rangle = \langle \rho_x (1 - \mathbf{u}_x^2) (1 - \mathbf{u}_y^2) \rho_y \rangle. \quad (3.26)$$

The chiral condensate is given in terms of unconstrained fields as well. It is obtained by using the trace of the correlator given in equation [\(3.25\)](#). The quadratic

fermion operator is replaced by the inverse of the fermion matrix,

$$\langle \dots i\bar{\lambda}_{x,i}\lambda_{y,j} \dots \rangle = \langle \dots Q_{xy,ij}^{-1} \dots \rangle_{\text{eff}} \quad (3.27)$$

and the lattice condensate $a\Xi_i$ is then written as

$$\begin{aligned} \langle a\Xi_i \rangle = \frac{1}{V} \sum_x \langle & 4\rho_x^2 Q_{xx,ii}^{-1} - 8\rho_x^3 u_{x,i} u_{x,j} Q_{xx,ij}^{-1} \\ & - 8\rho_x^3 u_{x,i} u_{x,j} Q_{xx,ji}^{-1} + 16\rho_x^4 u_{x,i} u_{x,i} u_{x,k} u_{x,l} Q_{xx,kl}^{-1} \rangle_{\text{eff}} \end{aligned} \quad (3.28)$$

for $i = 1 \dots N - 1$, where

$$\langle a\Xi_0 \rangle = \frac{1}{V} \sum_x \langle 16\rho_x^4 u_{x,k} u_{x,l} Q_{xx,kl}^{-1} \rangle_{\text{eff}}. \quad (3.29)$$

3.4.2 Fine tuning of the continuum limit

The continuum model is invariant under a discrete chiral symmetry. It is spontaneously broken in the infinite volume limit and the supersymmetric ground states correspond to the two ground states of this broken symmetry [99]. Using SLAC fermions, chiral symmetry is maintained on the lattice by the cost of having a non-local derivative. However, the applicability of the SLAC derivative to the present model is confined to small lattice volumes due to strong sign fluctuations [25]. Wilson fermions might offer the possibility to explore larger lattice volumes. It is an ultralocal derivative, where pseudofermion algorithms can be accelerated by preconditioning schemes. However, we expect that lattice artifacts are larger for the Wilson derivative compared to the SLAC case.

Following Wilson's idea, we introduce an additional momentum-dependent mass term that vanishes in the naive continuum limit,

$$M_{xy}^{\alpha\beta} = \gamma_{\mu}^{\alpha\beta} (\partial_{\mu}^{\text{sym}})_{xy} + \delta^{\alpha\beta} \frac{ra}{2} \Delta_{xy}, \quad (3.30)$$

where $\partial_{\mu}^{\text{sym}}$ is the symmetric lattice derivative, a the lattice spacing and Δ_{xy} the lattice Laplacian. We choose the bosonic derivative in the particular form

$$K_{xy} = - \sum_{\mu} (\partial_{\mu}^{\text{sym}})_{xy}^2 + \left(\frac{ra}{2} \Delta_{xy} \right)^2 \quad (3.31)$$

that has demonstrated superior results in Wess-Zumino models [100]. Using this formulation, we compute the masses of bosons and fermions in figure 15. The

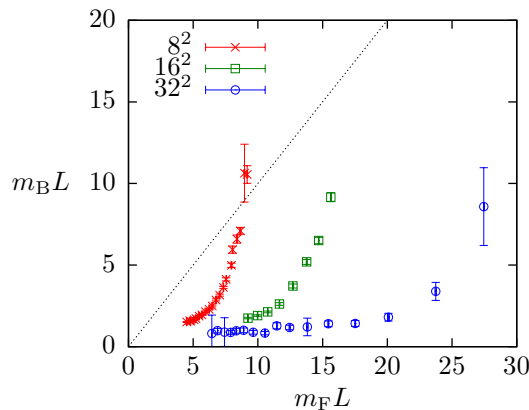


Figure 15: Comparison of the bosonic and fermionic mass in units of the box size for three different lattice sizes using Wilson fermions. The dotted line denotes the case $m_F = m_B$.

continuum limit is approached by keeping the physical box size (in units of the bosonic or fermionic mass) fixed, e.g. $m_B L = 5$, and going to larger lattice volumes. We obtain a significant discrepancy between the masses. This gap increases for larger lattices and there is no indication of convergent behaviour. In the continuum limit, the masses will not be degenerate, so that supersymmetry is apparently not restored. This is not too surprising, though, since Wilson fermions may break supersymmetry in a way that is not dissolved in the continuum limit. In particular, the Wilson prescription breaks chiral symmetry explicitly and the aforementioned behaviour indicates the renormalization of a relevant susy-breaking operator.

Since it is not possible to construct a discretized action which simultaneously respects at least one exact supersymmetry as well as the $O(3)$ symmetry, we must rely on adding fine tuning terms as a compensation for the renormalized couplings that arise from symmetry breaking terms on the lattice. For $\mathcal{N}=1$ Super Yang-Mills theories [101] it is known that the correct continuum limit may be achieved by a fine tuning term that resembles an explicit fermionic mass. One tunes the simulation such that the renormalized gluino mass is zero [102, 103]. Therefore we deform the fermionic derivative in a similar way using a fine tuning

mass m ,

$$M_{xy}^{\alpha\beta} = \gamma_{\mu}^{\alpha\beta} (\partial_{\mu}^{sym})_{xy} + \delta^{\alpha\beta} \frac{ra}{2} \Delta_{xy} + \delta^{\alpha\beta} m \delta_{xy}, \quad (3.32)$$

which enters the Hopping parameter $\kappa = (4 + 2m)^{-1}$. The chiral condensate is an order parameter for spontaneous chiral symmetry breaking. In the broken phase, the effective potential shows two minima, corresponding to the two supersymmetric ground states of the theory. In a finite volume, the tunneling probability is nonzero and both ground states contribute equally to the ensemble. Going to the infinite volume limit, tunneling is suppressed and only one of the ground states is present. For the Wilson derivative we expect that one of the ground state energies is raised due to the explicit breaking of chiral symmetry. Switching on the mass m , we aim to fine tune the effective potential such that none of the ground states is favored over the other. We will accomplish this by running parameter scans of κ and measuring the constraint effective potential of the chiral condensate for each run.

3.5 Performance of the HMC algorithm

Additional degrees of freedom in the fine tuning procedure increase the numerical effort considerably. With the sign problem and large condition numbers lurking, a Hybrid Monte Carlo algorithm with exact evaluation of the fermion determinant and the inverse fermion matrix is used. On small lattice volumes up to 16^2 , it provides a solid ground for the implementation of more sophisticated pseudofermion algorithms. They become necessary at large volumes due to the poor scaling behaviour of the LU decomposition used to solve for the inverse fermion matrix. We choose the RHMC algorithm [104]. Thereby, the spectrum of the Dirac operator is approximated by rational functions. It is of considerable importance to tune the many technical parameters of the RHMC in the right way in order to keep the algorithm exact and efficient. Therefore, we have monitored the sign of the Pfaffian determinant and the spectrum of the Dirac operator throughout our simulations. Table 3 shows average condition numbers c obtained from the exact matrix norm $c = \|Q\| \cdot \|Q^{-1}\|$ as well as typical iteration numbers of a conjugate gradient solver for three different choices of the fermion matrix: 1. the original fermion matrix (3.24), 2. the reduced fermion matrix, where a factor ρ , whose

	condition number	cg solver steps
original	$1.6(6) \times 10^{19}$	454(10)
reduced	$1.3(6) \times 10^8$	152(1)
even-odd	$1.4(7) \times 10^3$	48(1)

Table 3: Average condition numbers and CG solver steps for three different choices of the fermion matrix.

determinant can be evaluated analytically, is separated on both sides,

$$Q_{xy,ij}^{\alpha\beta} = 4(\delta_{ik} - 2u_{x,i}u_{x,k}\rho_x)M_{xy}^{\alpha\beta}(\delta_{kj} - 2u_{y,k}u_{y,j}\rho_y) + 16\rho_x u_{x,i}M_{xy}^{\alpha\beta}u_{y,j}\rho_y + 4\beta\sigma_x\delta_{xy}\delta_{ij}\delta^{\alpha\beta}, \quad (3.33)$$

and 3. the preconditioned reduced fermion matrix using the well-known even-odd preconditioning scheme [105]. The latter is a special case of incomplete LU preconditioning [106, 107]. One rewrites the fermion matrix as $1 - L - U$, where 1 is the identity matrix and L (U) is a lower (upper) triangular matrix. The critical step of the iterative cg solver is the application of the inverse of $Q^T Q$ to some random (pseudofermion) vector, $Y = (Q^T Q)^{-1}X$. We see a significant improvement in the number of solver steps and in the condition numbers for the reduced fermion matrix. This can directly be verified by looking at the eigenvalue spectrum depicted in figure 16. The original and the reduced matrix are real

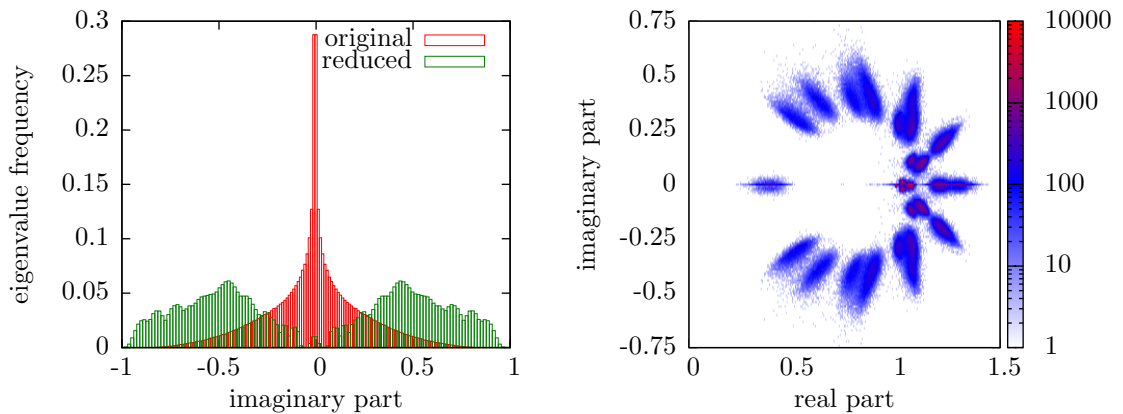


Figure 16: Eigenvalue frequency of the original and reduced fermion matrix (left panel, normalized such that both the largest eigenvalue and the integrated surface equal one) and for the even-odd preconditioned matrix (right panel, no normalization, logarithmic scale) from a sample of 2000 configurations on a 12^2 lattice.

and antisymmetric and thus all eigenvalues are purely imaginary and come in complex conjugate pairs. The original fermion matrix exhibits a large number of eigenvalues very close to zero, as expected according to the Banks-Casher-relation. For the reduced matrix we find that this is not the case and the condition numbers hence decrease drastically. A further improvement is achieved by even-odd preconditioning. The preconditioned matrix is no longer antisymmetric and the majority of eigenvalues lies close to 1.

3.6 Pfaffian sign

Given a generic partition sum of the form

$$Z = \int \prod_x \mathcal{D}\Phi_x e^{-S(\{\Phi\})}, \quad (3.34)$$

we are interested in the n-point functions

$$\langle \Phi_{x_1} \dots \Phi_{x_n} \rangle = Z^{-1} \int \prod_x \mathcal{D}\Phi_x \Phi_{x_1} \dots \Phi_{x_n} e^{-S}. \quad (3.35)$$

This high-dimensional integral is treated using stochastically distributed support points that are generated by Markov processes (Markov Chain Monte Carlo). The configuration space is sampled around the minima of the configuration weight

$$w(\{\Phi_x\}) = e^{-S(\{\Phi_x\})}, \quad (3.36)$$

where configurations with large action S are exponentially suppressed. This is the fundamental property that ascertains the great efficiency of the MCMC simulation. Of course, we have assumed that the weight $w(\{\Phi_x\})$ is semi-positive in order to interpret it as a probability weight. In the case

$$w'(\{\Phi_x\}) = e^{i\phi(\{\Phi_x\})} w(\{\Phi_x\}), \quad (3.37)$$

this is no longer true. Nevertheless, we may still use the reweighting trick and associate the complex phase with the measurement process rather than the con-

figuration weight:

$$\langle \Phi_{x_1} \dots \Phi_{x_n} \rangle_{w'} = \frac{\langle e^{i\phi} \Phi_{x_1} \dots \Phi_{x_n} \rangle_w}{\langle e^{i\phi} \rangle_w} \quad (3.38)$$

$$= \frac{Z_w^{-1} \int \prod_x \mathcal{D}\Phi_x e^{i\phi} \Phi_{x_1} \dots \Phi_{x_n} e^{-S(\{\Phi_x\})}}{Z_w^{-1} \int \prod_x \mathcal{D}\Phi_x e^{i\phi} e^{-S(\{\Phi_x\})}}. \quad (3.39)$$

However, this is only well defined if $\langle e^{i\phi} \rangle_w$ is not zero. In particular, due to the change of the configuration weight, we no longer sample the configurations that yield the largest contribution according to w' , but rather according to w . Since configurations are suppressed exponentially, the efficiency of our method depends crucially on the difference between the two weights. If the phase is fluctuating strongly, the number of configurations needed to perform the continuum limit is exponentially large. In fact, it was shown that the complexity of the *sign problem* is NP-hard [108]. This problem invalidates the MCMC method for scenarios that include frequent phase or sign changes.

The average Pfaffian sign for the Wilson derivative is depicted in figure 17. We see that for small values of the fine tuning parameter κ , changes in the

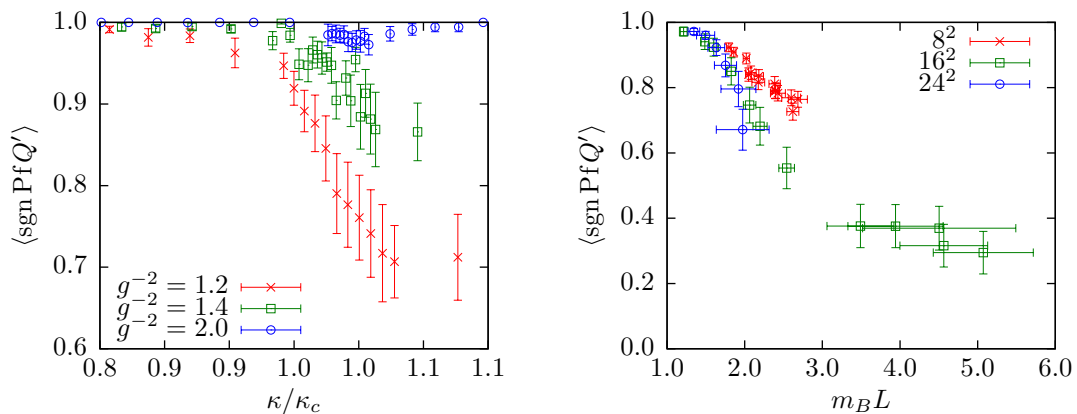


Figure 17: Left Panel: Sign of the Pfaffian on a $N = 16^2$ lattice for different couplings g^{-2} and normalized fine tuning parameter κ/κ_c . Right Panel: Average Pfaffian sign for different box sizes at $\kappa = \kappa_c$.

Pfaffian sign are suppressed and it is possible to evaluate expectation values directly without reweighting. In the vicinity of $\kappa \approx \kappa_c$ however, this behaviour changes from a mild correction for large coupling $g^{-2} = 2$ up to a significant correction for smaller coupling $g^{-2} = 1.2$. In the fine tuned ensemble at $\kappa = \kappa_c$,

a considerable sign problem is visible for large box sizes. Using the performance advances of even-odd preconditioning, we are able to account for the sign problem on lattice sizes of up to 24^2 , which is significantly larger than for the SLAC derivative, where only lattices up to 11^2 were feasible. All results presented in the next sections are obtained using the reweighting procedure.

3.7 $O(3)$ Symmetry

The previous studies have stressed the importance of an $O(3)$ invariant formulation of the theory. Our discretization respects the global flavor symmetry and in order to check whether the corresponding algorithms respect it as well we record the expectation value of the \mathbf{n} field. Using the stereographically projected fields \mathbf{u} , we generate $O(3)$ symmetric configurations, i.e. $\langle \mathbf{n} \rangle \approx 0$. However, we observe large autocorrelation times for observables which depend on the field component corresponding to the projection axis. We find that this problem arises from the interplay between stereographic projection and molecular dynamics steps. The Hybrid Monte Carlo algorithm uses a pseudo-Hamiltonian and corresponding pseudo-momenta for the \mathbf{u} fields to generate test configurations. Computing the pseudo-momenta for the constrained variables \mathbf{n} , we see that the momentum corresponding to the projection axis used in the HMC algorithm takes values roughly one half of the other momenta.

For the unconstrained variables, evolution of configurations is glued to a hyperplane of constant \mathbf{u}^2 , illustrated in figure [18](#) (left panel), where \mathbf{u}^2 , \mathbf{v}^2 and \mathbf{w}^2 correspond to the three canonical projection axes. Of course, the actual projection axis of the HMC algorithm is fixed in this plot. To circumvent this effect, the projection axis in the molecular dynamics step is changed repeatedly between successive trial and acceptance steps. While it is in principle possible to choose random projection axes for every update, we rotate through the three canonical axes, saving only every third configuration which corresponds to a fixed projection axis. A Metropolis acceptance step is yet needed after each change. The right panel of figure [18](#) shows how this improved update scheme restores the balance between the projection axes. The configuration space is traversed quickly and the expectation values $\langle n_i \rangle$ go to zero with ongoing MC time.

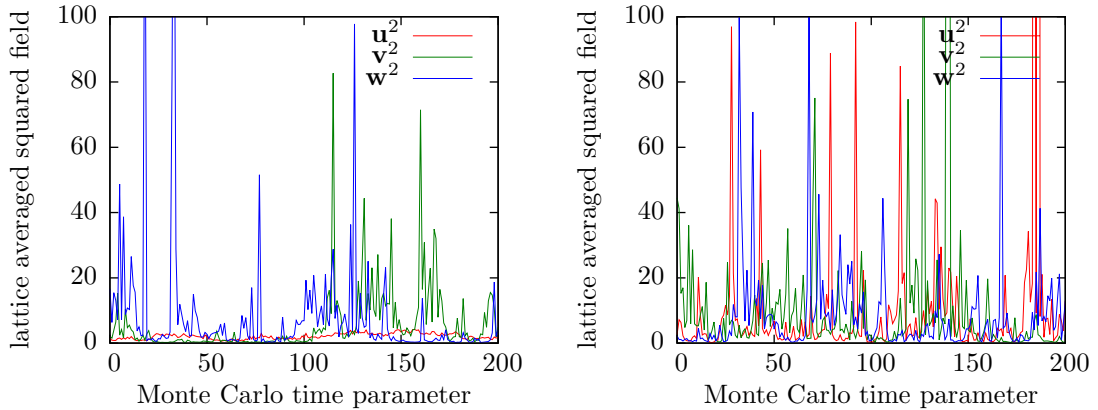


Figure 18: MC-histories for the lattice averages of \mathbf{u}^2 , \mathbf{v}^2 and \mathbf{w}^2 using the three different projection axes in the usual HMC algorithm (left panel) and the improved algorithm (right panel). Note that fluctuations for \mathbf{u}^2 , corresponding to the projection axis chosen in the HMC algorithm, are severely suppressed in the left panel.

3.8 Chiral symmetry

The lattice condensate is extracted from the trace of the projected correlator, while the sign of the Pfaffian is taken into account by a reweighting procedure,

$$\langle a\Xi \rangle = \frac{\langle \text{sgn Pf } Q a\Xi \rangle_q}{\langle \text{sgn Pf } Q \rangle_q}. \quad (3.40)$$

Here, $\langle \dots \rangle_q$ denotes the sign-quenched ensemble. We utilize histograms of the chiral condensate to measure the distribution function $\rho(X)$, which is formally obtained by introducing a delta function into the partition sum,

$$\rho(X) = \int \prod_x d\mathbf{u}_x d\sigma_x \delta(X - a\Xi) \text{sgn Pf } Q e^{-S_{\text{eff}}}. \quad (3.41)$$

Now, it is possible to express the expectation value for the condensate using this quantity as

$$\langle a\Xi \rangle = \frac{\int dX X \rho(X)}{\int dX \rho(X)}. \quad (3.42)$$

However, the distribution function (3.41) cannot be interpreted as a probability distribution, since $\text{sgn Pf } Q$ could be negative. Simulating the sign-quenched

ensemble, we need to use the reweighted distribution function

$$\rho(X) = \int \prod_x d\mathbf{u}_x d\sigma_x \delta\left(X - a\Xi \frac{\text{sgn Pf } Q}{\langle \text{sgn Pf } Q \rangle_q}\right) e^{-S_{\text{eff}}}. \quad (3.43)$$

However, this definition yields the correct result only if the chiral \mathbb{Z}_2 symmetry is intact. For Wilson fermions, we get an additive renormalization and the chiral condensate in the two ground states is not related by a simple sign-flip. To avoid this problem, we will omit the sign information when considering histograms, seeing that the Wilson ensemble shows frequent sign fluctuations only in the direct vicinity of the critical Hopping parameter. This allows for an extrapolation from a region where omitting the sign is safe. Expectation values are however *always* determined using the reweighting procedure and are hence not affected by this approximation. By an appropriate choice of the tuning parameter we obtain the spontaneously broken signature that is expected in the continuum limit (see figure [19](#), right panel), modified by the additive renormalization. The point of

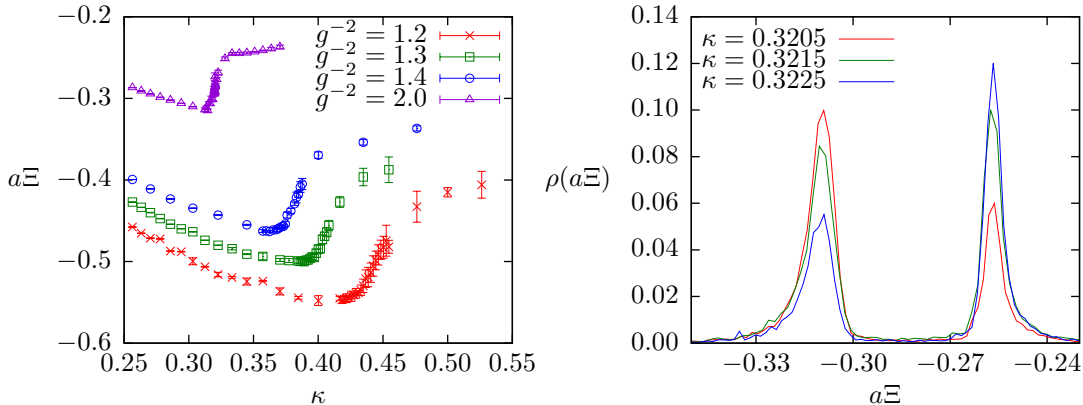


Figure 19: Left Panel: Expectation value of the chiral condensate $a\Xi$ for a lattice volume of 16^2 and different couplings g^{-2} . A jump corresponding to a first order transition is visible. Right Panel: Histograms of the chiral condensate $a\Xi$ for different values of the Hopping parameter ($N = 24^2$, $g^{-2} = 2$).

step increase in the curves shown in figure [19](#) (left panel) approaches a jump in the infinite volume limit. Thus, it is identified as a first order phase transition, analogous to the case of Super-Yang-Mills theories. Using this signature, we have determined the critical value of the fine tuning parameter κ_c for lattice sizes 8^2 , 16^2 and 24^2 and coupling $g^{-2} = 1 \dots 2$, see figure [20](#).

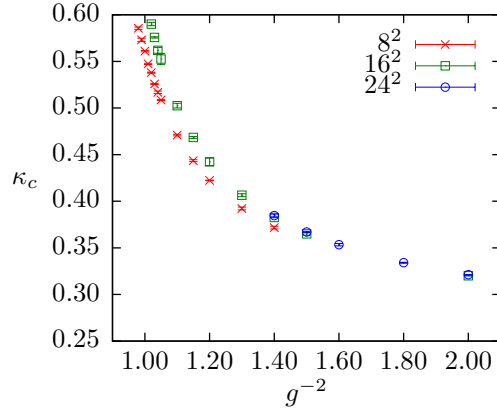


Figure 20: Critical value of the Hopping parameter for several lattice sizes.

3.9 Bosonic and fermionic mass

The masses of the elementary excitations are depicted in figure 21, left panel. We see that the bosonic mass is not affected by the fine tuning procedure and

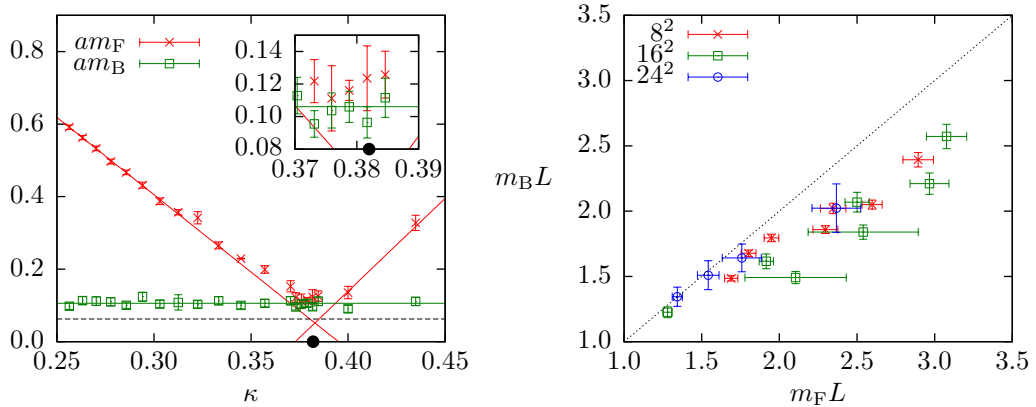


Figure 21: Left panel: scaling behaviour of the bosonic and fermionic mass for a 16^2 lattice and $g^{-2} = 1.4$ with $\kappa_c = 0.382(1)$, marked by the black dot. The dashed line denotes the lattice cutoff of $1/16$. Right panel: comparison of bosonic and fermionic masses in units of the box size for three different lattice sizes at $\kappa = \kappa_c$.

takes a constant value within error bars. We will hence use the bosonic mass to fix the physical box size $m_B L$ for our investigations. For the fermionic mass, we observe linear scaling behaviour for $\kappa < \kappa_c$ and $\kappa > \kappa_c$, however in the vicinity of $\kappa \approx \kappa_c$, the scaling breaks down. In contrast to e.g. $\mathcal{N}=1$ Super Yang-Mills [102], simulations at the critical point are feasible since the theory inhibits a finite mass

gap even in the continuum. In the vicinity of the phase transition, mixing between the two ground states occurs and the fermionic correlator must be projected onto one of them. Without loss of generality, we project onto the sector with $\Xi > 0$. This can be achieved by flipping the sign of σ for configurations with $\Xi < 0$.

We observe a great improvement regarding the degeneracy of the masses (see figure 21, right panel). In particular, the fermionic masses no longer “run away” if the volume is increased: This hints at a proper cancellation of the divergent operator causing these problems (compare to figure 15). Nevertheless, a true proof of this conjecture may only be provided by a study of all divergent operators based on lattice perturbation theory and is not pursued here. For finite box sizes of $m_B L > 2$ a thermal mass-splitting seems to emerge. A similar behaviour was encountered in studies using the SLAC derivative as well as for the $\mathcal{N} = 2$ Wess-Zumino model with spontaneously broken \mathbb{Z}_2 symmetry and one exact supersymmetry [100]. Analogously, we expect this thermal effect to disappear for large box sizes $m_B L \rightarrow \infty$. To explore this region, further large volume simulations would be needed in order to suppress possible lattice artifacts.

3.10 Path integral based Ward identity

Starting from the partition function (3.6), a twisted supercharge Q is used to construct a Q -exact action [90],

$$S = \frac{1}{2g^2} Q\Lambda \quad \text{with} \quad Q^2 = 0. \quad (3.44)$$

This implies the continuum Ward identity

$$\frac{\partial \ln \mathcal{Z}}{\partial(g^{-2})} = \langle -\frac{1}{2} Q\Lambda \rangle = 0, \quad (3.45)$$

since action and measure are invariant under the symmetry transformation generated by Q . A similar relation can be deduced for the partition function (3.22),

$$\frac{\partial \ln \mathcal{Z}}{\partial(g^{-2})} = -\frac{Vg^2}{2} - g^2 \langle S_\sigma \rangle + g^2 \frac{\dim Q}{2} \quad (3.46)$$

with V as number of lattice sites, $\dim Q$ the dimension of the fermion matrix in terms of flavor and spinor components as well as lattices sites and

$$S_\sigma = \frac{1}{2} \sum_{x,y} (4\rho_x \mathbf{u}_x^T K_{xy} \mathbf{u}_y \rho_y + \rho_x (1 - \mathbf{u}_x^2) K_{xy} (1 - \mathbf{u}_y^2) \rho_y) + \frac{1}{2} \sum_x \sigma_x^2. \quad (3.47)$$

Please note that an additional factor g^V from stereographic projection is important in order to arrive at this result. It is irrelevant for the computation of expectation values and usually dropped. In our case the Ward identity reads

$$\langle S_\sigma \rangle = \frac{3}{2} V. \quad (3.48)$$

In order to see a possible restoration of supersymmetry in the continuum limit, the bosonic action S_σ has been calculated in the fine tuned ensemble at $\kappa = \kappa_c$ (see figure [22](#)). We observe the Ward identity to approach the desired value from

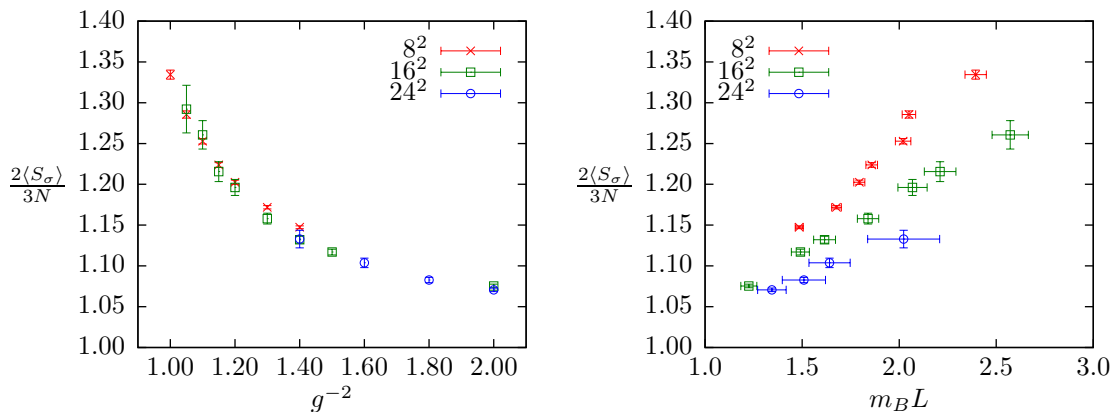


Figure 22: Expectation value of the bosonic action S_σ at $\kappa = \kappa_c$ for different g^{-2} (left panel) and different box sizes (right panel). $\frac{2\langle S_\sigma \rangle}{3N} = 1$ is expected in the supersymmetric continuum limit.

above, with a discrepancy of 7% for fine lattice spacing ($g^{-2} = 2$) and up to 14% for a coarser lattice spacing ($g^{-2} = 1.4$) on the 24^2 lattice. Overall, the slope of the Ward identity clearly points to a restoration of supersymmetry in the continuum limit.

3.11 Conclusion

In this project, a discretization of the supersymmetric nonlinear $O(3)$ Sigma model was investigated. The constraints of the original theory are resolved by a stereographic projection and this leads to an $O(3)$ symmetric simulation algorithm. The ultra-local Wilson derivative is employed together with an even-odd preconditioning scheme. For small lattices, we find that the simulation time is thereby reduced by an order of magnitude and even stronger reductions are achieved for larger lattices. This preconditioning scheme is not applicable for the SLAC derivative, since it is nonlocal.

Regarding sign fluctuations, we find that they reappear if the simulation is tuned to the critical Hopping parameter. This corresponds to a tuning to the spontaneously broken chiral symmetry that is expected in the continuum limit. However, the sign problem at fixed lattice volume is weaker compared to SLAC fermions and the cheaper simulations allow us to simulate lattices of up to 24^2 . This is a considerable improvement to earlier SLAC-based studies.

Our results verify $O(3)$ symmetry and chiral symmetry. While the former is respected on the lattice, the latter is broken spontaneously and the supersymmetric ground states are visible as minima of the constraint effective potential of the chiral condensate. Regarding supersymmetry, we find that bosonic and fermionic masses agree well. In particular, it does not seem to be necessary to tune counterterms other than the fermionic mass, which is used to correct for the explicit chiral symmetry breaking of the Wilson derivative. For intermediate box sizes, a thermal contribution to the mass gap is visible and the degeneracy is superseded. We expect this residual discrepancy to vanish for large box sizes. This is supported by measurements of a Ward identity, which unambiguously goes towards the supersymmetric value if the simulation is tuned to the continuum limit.

However, in order to actually see a restoration of supersymmetry, even larger lattices are needed. For these simulations, the sign problem can no longer be treated by computational power alone, but should be handled systematically. In the next chapter, we discuss the fermion-bag approach. It has shown promising results in the special case of four-fermi interactions and might improve the sign problem for the supersymmetric nonlinear $O(3)$ Sigma model as well.

4 Fermion-bag approach to Monte Carlo sign problems

4.1 Sign problems in lattice QFT

Lattice quantum field theory has progressed significantly throughout the past decades and the recent advances can be attributed not only to faster computers but more importantly to more efficient algorithms [109].

The study of the QCD phase diagram in the regime of finite temperature and chemical potential has been an active topic in recent years [110–113]. It is particularly interesting for the study of dense matter in the early universe, in neutron stars and in heavy ion collisions at future experiments like e.g. RHIC, FAIR and NICA⁷ [114]. In order to generate MCMC configurations, the Hybrid Monte Carlo algorithm has been established and current research focuses on accelerating the most costly part, which is the computation of the pseudo-Hamiltonian force e.g. using a Conjugate-Gradient type solver, by use of efficient preconditioning schemes [115]. It is clear that the fermionic contribution to the partition sum - the fermion determinant and the various ways to estimate it - provides the dominant contribution to the execution time of lattice QFT simulations.

However, the application of Monte Carlo methods to QCD at finite chemical potential is hindered by a fundamental problem: the weight of the path integral configurations becomes complex and can thus no longer be interpreted as a probability distribution [116]. This is denoted as the *complex phase problem* or *sign problem* and it is not limited to QCD. Sign problems appear in many theories, e.g. frustrated quantum systems that model condensed matter [117–120] or theories where spontaneous breaking of supersymmetry is possible, i.e. the Witten index vanishes [121–125]. A technical description of the sign problem in the supersymmetric nonlinear Sigma model was given in chapter 3.6. In order to overcome this problem, countless techniques have been studied, including the use of imaginary chemical potential [126–128], Taylor expansion [129], fugacity-expansion [130–132], reweighting techniques [133, 134] and the density-of-states

⁷See <http://www.bnl.gov/rhic/> for information regarding Brookhaven’s Relativistic Heavy Ion Collider, <http://www.fair-center.de> for the Facility for Antiproton and Ion Research at GSI Darmstadt and <http://nica.jinr.ru/> for the Nuclotron-based Ion Collider fAcility at JINR, Dubna.

method [135–138]. However, each of these has only a limited domain of applicability and one is interested in a solution that addresses the core problem itself – the complex weight. Considerable progress has been reported for the application of the complex Langevin equation [139–141] to this problem as well as regarding the use of dual variables [142–146]. In the following chapters however, we will use the *fermion-bag method*. It was presented first in [147] and was shown to be particularly suited to four-fermi interactions, where the sign problem was softened or even eliminated.

4.2 The fermion-bag method

The conventional approach to four-fermi theories rests on the application of the Hubbard-Stratonovich transformation, which converts a model of interacting fermions into a model of fermions that propagate freely in an auxiliary background potential. It is thus also denoted as the auxiliary field approach. In a series of recent articles [148–152], it was argued that in some cases the partial bosonization of fermions introduces additional sign fluctuations to the configuration weight. A contrasting approach called the *fermion-bag method* was shown to eliminate sign fluctuations in models of staggered fermions with Gross-Neveu or Thirring interaction. As a general conclusion, it was denoted that the fermion-bag approach is successful whenever a suitable pairing mechanism is available for the fermions. Of course, this depends on the model at hand and it is clear that the fermion-bag method is no solution to the sign problem in a strict sense [108]. It is simply a resummation of degrees of freedom and the models that are free of sign fluctuations in the fermion-bag formulation actually never suffered from a sign problem: it was artificially introduced by using the conventional approach. True sign problems still exist, e.g. in lattice QED with Wilson fermions, for which the fermion-bag method failed [153]. Nevertheless, it may help to uncover hidden pairing mechanisms and an application to four-fermion models is worthwhile. For some theories, the fermion-bag method leads to the computation of fermionants [154], which can be exponentially hard to calculate [155] in contrast to determinants, for which polynomial time algorithms exist. In this case, the fermion-bag method is not useful. An example is the $D = 3$ Gross-Neveu model with four-component spinors and Wilson fermions. To circumvent this problem,

one might use staggered fermions which diagonalize the spinor degrees of freedom [156] or use a non-standard interaction term like e.g. a six-fermi or even higher term. We choose to investigate the Gross-Neveu model using the irreducible representation of the gamma matrices, i.e. with two-component spinors, where the fermion-bag method is applicable as well. Furthermore, we will investigate the supersymmetric nonlinear $O(3)$ Sigma model once again with a special emphasis on the sign problem.

We start with the supersymmetric NLSM and derive the fermion-bag formulation. In a first approach, we study the quenched approximation. It will serve to map out our expectations for the full model, which is studied in detail afterwards. We report our findings and proceed with the one-flavor Gross-Neveu model. Instead of sign fluctuations, we have to deal with a complex phase here. Therefore, we begin with a short investigation of the model using the SLAC derivative, uncovering the basic properties. The next step consists of a derivation of the fermion-bag discretization, which uses the Wilson derivative. After we have presented our results, we conclude the chapter and compare the payoff of the fermion-bag method for both models.

4.3 The supersymmetric nonlinear $O(3)$ Sigma model

The two-dimensional supersymmetric nonlinear $O(3)$ sigma model was studied extensively in chapter 3. In order to arrive at a discretized action that is suitable for MCMC simulations, we treated the four-fermi interaction term by a Hubbard-Stratonovich transformation, which results in a Yukawa-like interaction for the Majorana fermions and an auxiliary field σ , which does not propagate. After integrating out the fermions, the effective action for the bosonic degrees of freedom contains the Pfaffian of the fermion matrix, which now depends on the σ field. We have demonstrated in chapter 3.6 that the sign of the Pfaffian determinant is not constant but rather fluctuates. In particular, going to the continuum limit, fluctuations become more pronounced and the cost of generating configurations rises exponentially. This is a major problem and prevents further progress regarding this model.

In order to advance on the sign problem, the idea of dual variables was applied to the model recently by separate groups. Progress was reported in a proceeding

[157] and a bachelor thesis [158]. The latter was supervised by the author. Alas, the preliminary results point to a residual sign problem for $N \geq 3$. We have thus chosen an alternative approach - the fermion-bag method.

4.3.1 Derivation of the fermion-bag discretization

The fermionic action of the model is written as

$$S_F = S_{2F} + S_{4F} = \frac{2}{g^2} \sum_{x,y} \boldsymbol{\lambda}_x^\top i Q_{xy} \boldsymbol{\lambda}_y + \frac{2}{g^2} \sum_x \rho_x^4 (\boldsymbol{\lambda}_x^\top C \boldsymbol{\lambda}_x)^2, \quad (4.1)$$

where the fermion matrix Q is given by

$$Q_{xy}^{\alpha\beta} = 4\rho_x (\delta_{ik} - 2u_{x,i}u_{x,k}\rho_x) M_{xy}^{\alpha\beta} (\delta_{kj} - 2u_{y,k}u_{y,j}\rho_y) \rho_y + 16\rho_x^2 u_{x,i} M_{xy}^{\alpha\beta} u_{y,j} \rho_y^2 \quad (4.2)$$

and $M_{xy}^{\alpha\beta}$ is the Wilson derivative, see equation (3.30). It is evident that fermionic fields at separate lattice points do not mix in the four-fermi interaction⁸,

$$S_{4F} = \frac{2}{g^2} \sum_x \rho_x^4 (\lambda_{x,i}^\alpha C^{\alpha\beta} \lambda_{x,i}^\beta)^2 = \frac{16}{g^2} \sum_x \rho_x^4 \lambda_{x,0}^0 \lambda_{x,0}^1 \lambda_{x,1}^0 \lambda_{x,1}^1. \quad (4.3)$$

Instead of the usual bosonization of the four-fermi interaction, we separate the term and expand the exponential $e^{-S_{4F}}$ in the fermionic part of the partition sum:

$$Z_F = \int \prod_{z,l} d\lambda_{z,l}^0 d\lambda_{z,l}^1 \left(1 - \frac{16}{g^2} \rho_z^4 \lambda_{z,0}^0 \lambda_{z,0}^1 \lambda_{z,1}^0 \lambda_{z,1}^1 \right) e^{-\frac{1}{2} \sum_{x,y} \boldsymbol{\lambda}_x^\top i Q_{xy} \boldsymbol{\lambda}_y}. \quad (4.4)$$

We introduce a new field k that takes the values $k_z \in \{0, 1\}$ and maps all possible factors of the product in (4.4) to configurations $\{k\}$. The remaining exponential function is expanded in an analogous way:

$$Z_F = \sum_{\{k\}} \int \prod_{z,l} d\lambda_{z,l}^0 d\lambda_{z,l}^1 \left(\frac{16}{g^2} \rho_z^4 \lambda_{z,0}^0 \lambda_{z,0}^1 \lambda_{z,1}^0 \lambda_{z,1}^1 \right)^{k_z} \prod_x e^{-\frac{1}{2} \boldsymbol{\lambda}_x^\top \sum_y i Q_{xy} \boldsymbol{\lambda}_y}. \quad (4.5)$$

⁸We use the explicit representation of the gamma-matrices: $\gamma_0 = \sigma_3$, $\gamma_1 = -\sigma_1$, $\gamma_* = i\gamma_0\gamma_1 = \sigma_2$, $C = -i\sigma_2$. In general, x and y correspond to lattice indices, i and j to flavor indices and α and β to spinor indices.

The integrand corresponds to a sum of products analogous to a high-temperature expansion. In order to provide a contribution to the partition sum, the Grassmann integral must include every fermionic degree of freedom exactly once, lest it vanishes due to the Grassmann nature of the fermions. Please note that for a given configuration $\{k\}$, the Grassmann integration is completely saturated at the lattice point z by setting $k_z = 1$. Therefore, all addends that include factors $\frac{1}{2}\boldsymbol{\lambda}_x^\top iQ_{xy}\boldsymbol{\lambda}_y$ with $x = z$ or $y = z$ vanish. Only factors with indices from the set

$$\left\{ (x, i, \alpha) \mid x \in \{0, \dots, V-1\}, i \in \{0, 1\}, \alpha \in \{0, 1\}, k_x = 0 \right\}, \quad (4.6)$$

are allowed. Let $P[k]$ be a partition of these indices into pairs $\{(x, i, \alpha), (y, j, \beta)\}$ without respect to ordering. The partition sum is thereby rewritten as

$$Z_F = \sum_{\{k\}} \int \prod_{z,l} d\lambda_{z,l}^0 d\lambda_{z,l}^1 \left(-\frac{16}{g^2} \rho_z^4 \lambda_{z,0}^0 \lambda_{z,0}^1 \lambda_{z,1}^0 \lambda_{z,1}^1 \right)^{k_z} \sum_{P[k]} \prod_{\{(x,i,\alpha),(y,j,\beta)\}} \lambda_{x,i}^\alpha iQ_{xy,ij}^{\alpha\beta} \lambda_{y,j}^\beta, \quad (4.7)$$

where a factor 2^{-k_z} was accounted for by the overcounting of the sum in equation (4.5) in comparison to the sum over all partitions $\sum_{P[k]}$. We proceed by integrating out all fermionic degrees of freedom which gives the usual Pfaffian of the fermion matrix. However, due to the introduction of the k field, only those rows and columns are present for which $k_x = 0$:

$$\begin{aligned} Z_F &= \sum_{\{k\}} \int \prod_{z,l} d\lambda_{z,l}^0 d\lambda_{z,l}^1 \lambda_{0,0}^0 \dots \lambda_{V-1,1}^1 \left(-\frac{16}{g^2} \rho_z^4 \right)^{k_z} \sum_{P[k]} \text{sgn } P[k] \prod_{\{(x,i,\alpha),(y,j,\beta)\}} iQ_{xy,ij}^{\alpha\beta}, \\ &= \sum_{\{k\}} \prod_z \left(-\frac{16}{g^2} \rho_z^4 \right)^{k_z} \text{Pf } iQ[k] = \sum_{\{k\}} \prod_z \left(\frac{16}{g^2} \rho_z^4 \right)^{k_z} \text{Pf } Q[k]. \end{aligned} \quad (4.8)$$

Analogous to chapter 3.5, we split the ρ factors from the fermion matrix, which results in the final formulation:

$$Z_F = \sum_{\{k\}} \prod_z \rho_z^4 \left(\frac{16}{g^2} \right)^{k_z} \text{Pf } Q'[k], \quad (4.9)$$

with the fermion matrix

$$Q'_{xy,ij} = 4(\delta_{ik} - 2u_{x,i}u_{x,k}\rho_x)CM_{xy}(\delta_{kj} - 2u_{y,k}u_{y,j}\rho_y) + 16\rho_x u_{x,i}CM_{xy}u_{y,j}\rho_y. \quad (4.10)$$

The discretization of the bosonic part proceeds as depicted in chapter [3.4.1](#) and the partition function for the full model reads

$$Z = \sum_{\{k\}} \int \prod_x d\mathbf{u}_x \left(\frac{16}{g^2}\right)^{k_x} e^{-S_{\text{eff}}(\{\mathbf{u},k\})}, \quad (4.11)$$

where the effective action is

$$S_{\text{eff}}(\{\mathbf{u},k\}) = \frac{1}{2g^2} \sum_{x,y} (4\rho_x \mathbf{u}_x K_{xy} \mathbf{u}_y \rho_y + \rho_x (1 - \mathbf{u}_x^2) K_{xy} (1 - \mathbf{u}_y^2) \rho_y) - 2 \sum_x \log \rho_x - \log \text{Pf } Q'[k]. \quad (4.12)$$

For the fermionic derivative, we use the Wilson operator which includes only nearest-neighbor interactions. We emphasize that this leads to a simplification of the Pfaffian. Given a configuration $\{k\}$, we locate the connected clusters B_i of lattice sites x for which $k_x = 0$. If two or more such clusters exist, then the fermion matrix can be rearranged such that the Pfaffian is given by the product of the Pfaffian determinants for each cluster,

$$\text{Pf } Q'[k] = \prod_i \text{Pf } Q'[B_i]. \quad (4.13)$$

These clusters are called *fermion-bags*. A reduction of the matrix size translates into a large decrease of the simulation time. A simple algorithm for the computation of the determinant, like e.g. the LU decomposition, scales according to n^3 , where $n = 2NV$ is the size of the fermion-matrix for the supersymmetric non-linear O(N) Sigma model. Furthermore, whereas the size of the fermion matrix naturally grows with the lattice volume V , this is not necessarily true for the size of the fermion-bags $|B_i|$. The simulation time is thus governed by the largest fermion bag B_+ ,

$$\tau \propto |B_+|^3. \quad (4.14)$$

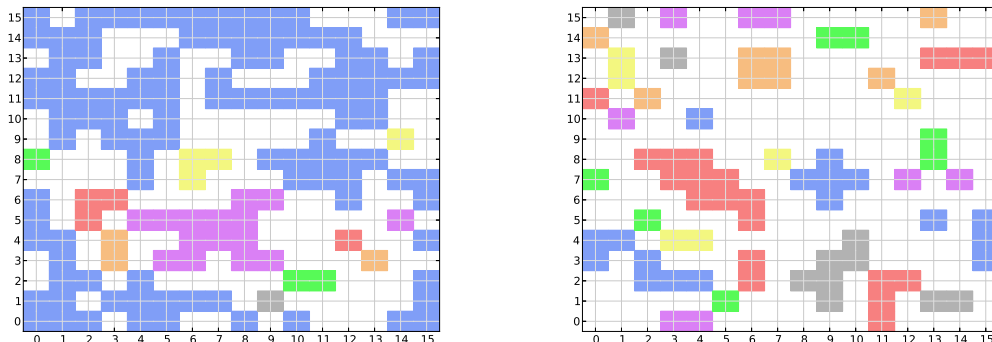


Figure 23: Visualization of typical fermion-bags - the connected clusters of lattice sites x for which $k_x = 0$ - in the quenched ensemble for $g^{-2} = 0.05$ (left panel) and $g^{-2} = 0.2$ (right panel). Although different colors correspond to different fermion-bags, some colors are used several times.

In order to picture possible expectations of the fermion-bag approach, we first concern ourselves with the quenched approximation, i.e. we ignore the contribution of the Pfaffian determinant.

4.3.2 Quenched ensemble

The k and \mathbf{u} field interact only through the Pfaffian determinant. If we ignore it, then the expectation values of the k field no longer depend on the bosonic field and we can investigate the simplified partition function

$$Z_q = \sum_{\{k\}} \prod_x \left(\frac{16}{g^2} \right)^{k_x}. \quad (4.15)$$

The mean number of fermion-bags $\langle n_B \rangle_q$ and the average size of the largest bag $\langle |B_+| \rangle_q$ are depicted in figure 24. In the $g^{-2} \rightarrow \infty$ limit, configurations with $k_x = 1$ are favored and a formation of fermion-bags does not occur. In particular, we find that for a fixed coupling with $g^{-2} > 0.03$ the size of the largest fermion-bag does not scale with the lattice volume. This is a much desired property for the full model. The strong coupling limit, $g^{-2} \rightarrow 0$, is dominated by configurations with $k_x = 0$ and the fermion-bags grow to their maximum size. The fermions propagate freely, which is expected from asymptotic freedom, but the simulation

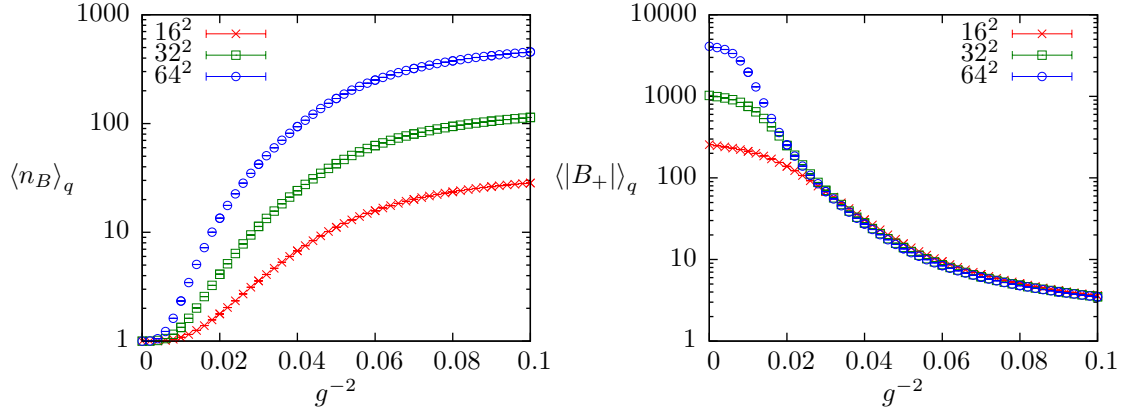


Figure 24: Shown is the number of fermion-bags (left panel) and the size of the largest bag (right panel) in dependence of the coupling constant for the quenched ensemble Z_q .

time is large. Since this limit is easily described by perturbation theory, it seems contradictory that the numerical effort grows to its maximum. Fortunately, we can use an alternative derivation of the fermion-bag method that is efficient in the strong coupling limit. It is called the *dual fermion-bag approach*.

4.3.3 Dual fermion-bag approach

The dual fermion-bag method is related to the diagrammatic Monte Carlo method [159, 160]. We will derive the formulation starting from equation 4.5. One recognizes that the field insertions $\lambda_{z,0}^0 \lambda_{z,0}^1 \lambda_{z,1}^0 \lambda_{z,1}^1$, which stem from the expansion of the four-fermi interaction term, can be created by functional derivation of a generating functional:

$$\frac{\partial}{\partial \eta_{z,0}^0} \frac{\partial}{\partial \eta_{z,0}^1} \frac{\partial}{\partial \eta_{z,1}^0} \frac{\partial}{\partial \eta_{z,1}^1} Z_F[\eta] \Big|_{\eta=0} = \int \prod_{z,l} d\lambda_{z,l}^0 d\lambda_{z,l}^1 \lambda_{z,0}^0 \lambda_{z,0}^1 \lambda_{z,1}^0 \lambda_{z,1}^1 e^{-\frac{1}{2} \sum_{x,y} \lambda_x^\top i Q_{xy} \lambda_y}, \quad (4.16)$$

with

$$Z_F[\eta] = \int \prod_{z,l} d\lambda_{z,l}^0 d\lambda_{z,l}^1 e^{-\frac{1}{2} \sum_{x,y} \lambda_x^\top i Q_{xy} \lambda_y + \sum_x \eta_x^\top \lambda_x}. \quad (4.17)$$

Using Wick's theorem, the expression evaluates to the Pfaffian of the propagator matrix. It consists of all propagators between the lattice sites z with $k_z = 1$,

$$Q'^{-1}[k] = \begin{pmatrix} \ddots & & & \\ & (Q'^{-1})_{xy,ij}^{\alpha\beta} & & \\ & & \ddots & \\ & & & \ddots \end{pmatrix} \quad \text{with } k_x = k_y = 1. \quad (4.18)$$

The partition function thus takes the form:

$$Z_F = \sum_{\{k\}} \prod_z \rho_z^4 \left(\frac{16}{g^2} \right)^{k_z} \text{Pf } Q'^{-1}[k] \text{Pf } Q'. \quad (4.19)$$

Comparing equations (4.19) and (4.9), we find the *duality relation*

$$\text{Pf } Q'[k] = \text{Pf } Q'^{-1}[k] \text{Pf } Q'. \quad (4.20)$$

The collection of sites with $k = 1$ is called the *dual fermion-bag*. In general, the propagator matrix is dense and a splitting of the Pfaffian akin to the regular fermion-bags is not possible. Therefore, it is not meaningful to define disconnected dual fermion-bags. The effective action for the full model using the dual fermion-bag approach reads

$$S_{\text{eff}} = \frac{1}{2g^2} \sum_{x,y} 4\rho_x \mathbf{u}_x K_{xy} \mathbf{u}_y \rho_y + \rho_x (1 - \mathbf{u}_x^2) K_{xy} (1 - \mathbf{u}_y^2) \rho_y - 2 \sum_x \log \rho_x - \log \text{Pf } Q'^{-1}[k] - \log \text{Pf } Q', \quad (4.21)$$

where the partition sum is given by equation (4.11). The Pfaffian of the fermion matrix $\text{Pf } Q'$ does not depend on $\{k\}$ and can be ignored in an update of the fermion-bag configuration. One is left with the computation of the propagator matrix and its Pfaffian determinant. Please note that for each update, the inverse of the full fermion matrix needs to be computed and only afterwards, lines and columns corresponding $k = 0$ are dropped.

We have laid out both fermion-bag methods and proceed with results for the full model without resorting to the quenched approximation.

4.3.4 The full ensemble

Dynamical variables of the full model include stereographically projected bosonic fields \mathbf{u} and fermion-bags k . The ensemble is defined by partition function (4.11) and effective action (4.12) or (4.21) depending on whether the regular or dual fermion-bag approach is used. In order to construct a Markov Chain of configurations, \mathbf{u} and k are updated separately. The former is treated by the O(3) improved HMC algorithm that was outlined in chapter 3.7. However, instead of a rational approximation, the Pfaffian is calculated explicitly using the method in [161]. Though this leads to larger simulation times, it is in part compensated by using the more efficient fermion-bag formulation. The fermion-bags are updated by a local Metropolis step. For each lattice site x , we propose to update the fermion-bag variable $k_x \rightarrow k'_x \in \{0, 1\}$. The acceptance probability is given by

$$p_{\text{acc}} = \left(\frac{16}{g^2}\right)^{k'_x - k_x} \frac{\prod_i \text{Pf } Q'[B'_i]}{\prod_j \text{Pf } Q'[B_j]} \quad (4.22)$$

for the regular fermion-bag update or

$$p_{\text{acc}} = \left(\frac{16}{g^2}\right)^{k'_x - k_x} \frac{\text{Pf } Q'^{-1}[k']}{\text{Pf } Q'^{-1}[k]} \quad (4.23)$$

for the dual fermion-bag update. We have calculated the mean number of bags and the size of the largest bag for different couplings and Hopping parameters in figure 25. Both observables vary strongly with κ and it is evident that a precise fine tuning is needed. We have verified the values for the critical Hopping parameter κ_c that were determined in chapter 3.8 by computing the constraint effective potential of the chiral condensate again, using the fermion-bag approach. There is a technical difference between both formulations. In the bosonized discretization, the interaction is implemented by the background field. For the fermion-bags, it is generated by dropping certain rows and columns from the fermion matrix. Of course, regarding the resulting expectation values, we find good agreement. It is quite interesting that $\langle n_B \rangle$ and $\langle |B_+| \rangle$ have an extremum in the vicinity of the critical Hopping parameter.

The mean number of bags and size of the largest fermion bag in the fine tuned ensemble are shown in figure 26. Comparing with the quenched results in figure

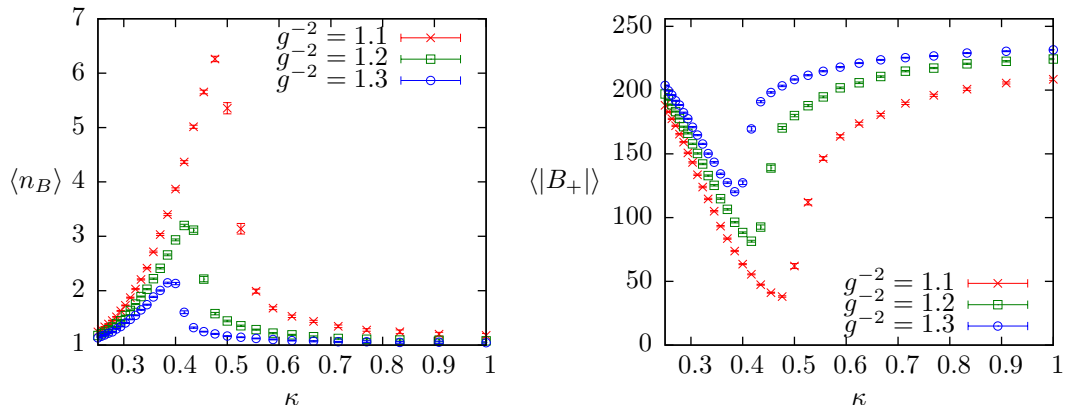


Figure 25: We show the number of fermion-bags (left panel) and the size of the largest bag (right panel) in dependence of the Hopping parameter for different coupling constants on a 16^2 lattice.

[24], we see that the behaviour of the observables has changed significantly. The size of the bags grows towards the continuum limit, i.e. $g^{-2} \rightarrow \infty$. Furthermore, for sufficiently small coupling, we see a clear scaling of the fermion-bag size with the lattice volume.

Following our previous discussion for the quenched model, it might be beneficial to use the dual fermion-bag approach in the small coupling regime since it offers increased performance in the case of large bag sizes. However, in order to evaluate the acceptance probability (4.23), one needs to compute the Pfaffian of the propagator matrix $Q^{-1}[k]$. Since we compute the Pfaffian exactly, knowledge of all elements of Q^{-1} is required. Alas, the fermion matrix depends on the bosonic degrees of freedom and the full inverse needs to be computed at every step of the HMC integration, which renders the dual fermion-bag algorithm too expensive to be applicable for this model. A faster approach might be given by discarding the Pfaffian sign and using the identity $\text{Pf}^2 M = \det M$ for a skew-symmetric matrix M . It is then possible to rewrite the contribution to the effective action,

$$e^{\log |\text{Pf} M|} = e^{\frac{1}{2} \log \det M} = e^{\frac{1}{2} \text{tr} \log M}. \quad (4.24)$$

It was shown in [162] that $\text{tr} \log M$ may be computed efficiently using stochastic estimator and Padé approximation techniques. However, since the sign of the Pfaffian fluctuates, it must be computed separately, which diminishes the

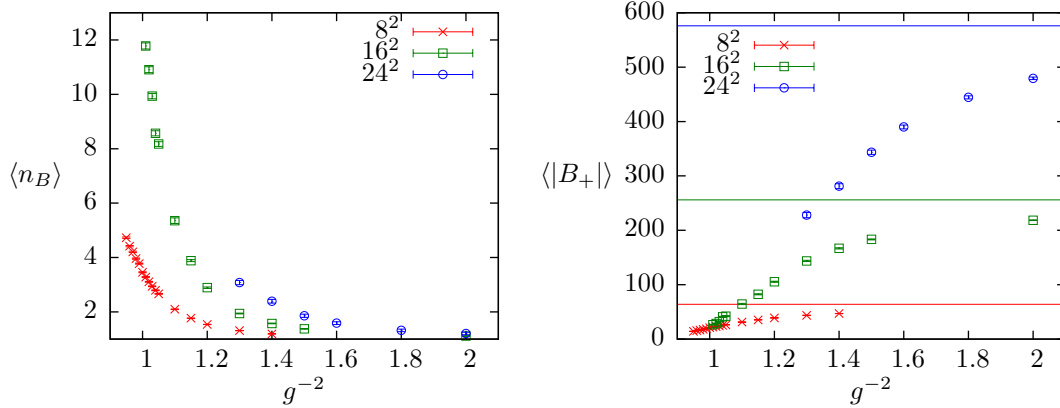


Figure 26: Shown is the number of fermion-bags (left panel) and the size of the largest bag (right panel) in dependence of the coupling constant for the full model. The solid lines denote the maximum bag size $|B_{\max}| = V$.

efficiency of the approach. Therefore, we have not pursued this method and continue to use the regular fermion-bag method.

In order to investigate the continuum limit, we use the bosonic two-point function in equation 3.26 to extract the bosonic mass $m_B a$. Again, values for the bosonized and fermion-bag formulation agree within error bars and we show $\langle n_B \rangle$ and $\langle |B_+| \rangle$ for different box sizes $m_B L$ in figure 27. The continuum limit is

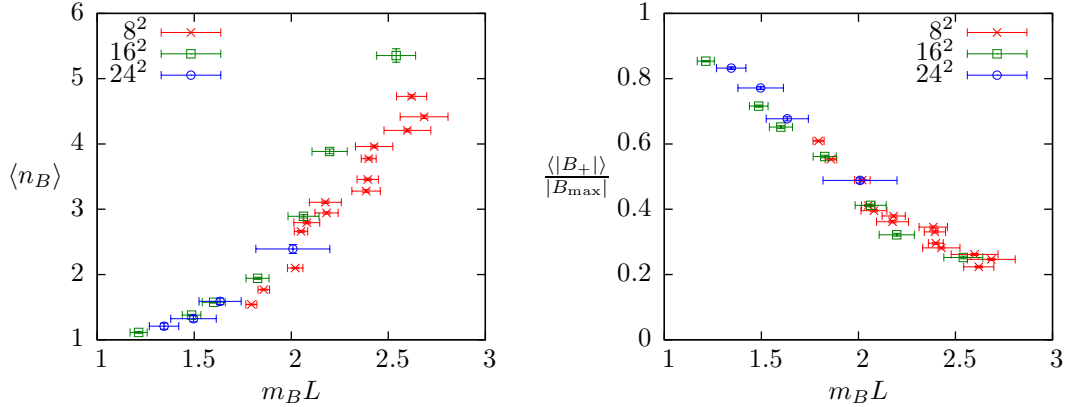


Figure 27: The number of fermion-bags (left panel) and the relative size of the largest bag (right panel) are shown. For fixed physical box size $m_B L = \text{const.}$, the relative bag size does not depend on the lattice volume.

approached by keeping the box size $m_B L$ fixed and increasing the lattice volume. We immediately see that the relative size of the largest bag $\langle |B_+| \rangle / |B_{\max}|$ does not change towards the continuum limit. The size of the largest bag thus scales

linearly with the lattice volume,

$$\langle |B_+| \rangle \propto |B_{\max}| = V. \quad (4.25)$$

Consequently, the scaling of the simulation time τ is equivalent to the behaviour for the bosonized formulation. We must conclude that the fermion-bag method does not show an advantage in this respect.

It is still important to evaluate the fluctuations of the Pfaffian sign since it directly affects the applicability of the MCMC method. In figure 28, we compare the average sign for the fermion-bag method (left panel) and the bosonized formulation (right panel) depending on the coupling constant. It is evident that while

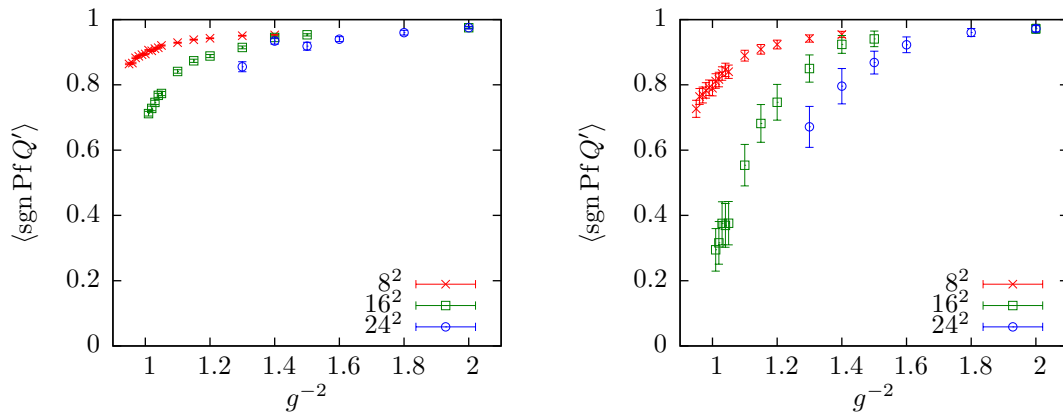


Figure 28: The expectation value of the Pfaffian sign is shown for the fermion-bag method (left panel) and the auxiliary field method (right panel). We see that sign fluctuations are significantly reduced for the fermion-bag approach.

sign fluctuations still occur, they are significantly smaller than for the bosonized formulation. This conclusion is valid even in the continuum limit, which is shown in figure 29. Alas, keeping the box size fixed, we still find that the sign problem gets slightly worse for larger volumes. However, the notable reduction in sign fluctuations is going to allow the study of lattice sizes considerably larger than possible up to now.

4.4 The one-flavor Gross-Neveu model

The Gross-Neveu model in three space-time dimensions is often formulated using a reducible representation of the gamma matrices. In this case, the model is

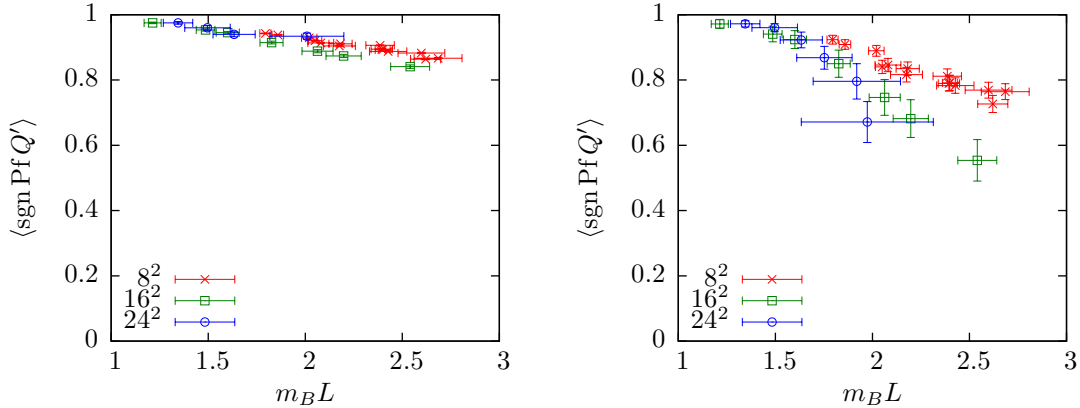


Figure 29: We show the behaviour of the average sign towards the continuum limit for the fermion-bag method (left panel) and the bosonized model (right panel). For fixed box size, the sign problem gets worse for larger lattice volumes.

invariant under a continuous chiral symmetry. Furthermore, it is γ_5 -hermitean and the fermion determinant is real. In this chapter however, we will construct the model with the irreducible representation and γ_5 -hermiticity is lost. Our aim is to evaluate the complex phase of the fermion determinant in both the conventional discretization and the fermion-bag approach.

For N_f flavors of Dirac-spinors ψ_i , $i \in \{0, \dots, N_f - 1\}$, the action of the massless Gross-Neveu model takes the form

$$S = \int d^3x \left\{ \bar{\psi}_i \not{\partial} \psi_i - U (\bar{\psi}_i \psi_i)^2 \right\}, \quad (4.26)$$

where U is the four-fermi coupling constant. The model exhibits a $U(N_f)$ flavor symmetry,

$$\psi_i \rightarrow U_{ij} \psi_j, \quad \bar{\psi}_i \rightarrow \bar{\psi}_j U_{ji}^\dagger, \quad U_{ij} \in U(N_f). \quad (4.27)$$

The irreducible representation of the gamma matrices in three space-time dimensions may be explicitly written out using the Pauli matrices,

$$\gamma_0 = \sigma_1, \quad \gamma_1 = \sigma_2, \quad \gamma_2 = \pm \sigma_3. \quad (4.28)$$

Since there is no γ_5 matrix, it is not possible to define a chiral symmetry. However, the model is invariant under a parity transformation that results in a \mathbb{Z}_2 -

symmetry akin to a discrete chiral symmetry,

$$\psi_i(x) \rightarrow \psi_i(-x), \quad \bar{\psi}_i(x) \rightarrow -\bar{\psi}_i(-x). \quad (4.29)$$

In particular, the parity symmetry is broken explicitly by the parity condensate $\bar{\psi}_i(x)\psi_i(x)$. The model is not renormalizable in a loop expansion, which is already evident from a simple power counting analysis. However, in the large- N limit it is renormalizable to every finite order in $1/N$ and the model exists at a non-Gaussian fixed point [163, 164]. This fixed point corresponds to a second-order phase transition that divides a symmetric phase with order parameter $\langle \bar{\psi}\psi \rangle = 0$ from a phase with spontaneously broken symmetry, $\langle \bar{\psi}\psi \rangle \neq 0$. Using the functional renormalization group, this behaviour was established also for the $N = 1$ model [165]. Starting in the broken phase, there is a transition at high temperatures where the parity symmetry is restored, see figure 30 (left panel). This transition has been analyzed using the large- N expansion and analytical methods because of its similarity with the finite temperature chiral transition in two-flavor massless QCD and the critical behaviour was found to belong to the universality class of the 2d Ising model [164].

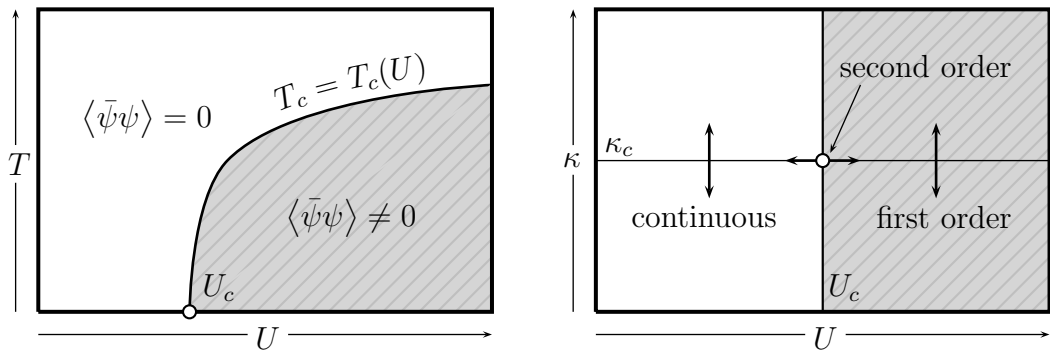


Figure 30: Presumed phasediagram of the continuum Gross-Neveu model for finite temperature (left panel) and of the discrete model at zero temperature (right panel).

4.4.1 Discretization

In the following sections, we will discretize the model using the SLAC and the Wilson derivative. In the latter case we introduce an additional fermion mass parameter analogous to the study of the supersymmetric nonlinear Sigma model, which is used to fine tune the model to the continuum limit. However, since the additional fine tuning increases the numerical expense of the simulation, we conduct a first investigation using the SLAC derivative. This study will serve to support our basic expectations of the model.

At zero temperature, we expect a phase transition at κ_c for couplings $U > U_c$ and a continuous transition for couplings $U \leq U_c$ (see figure 30, right panel). In the broken phase, the two ground states give rise to a latent heat for the transition around κ_c , which is thus of first order. This behaviour is used to construct the continuum limit. We start in the broken phase $U > U_c$ and evaluate the effective potential of the parity condensate $\bar{\psi}\psi$. By adjusting the Hopping parameter, we tune the ensemble such that the minima of the effective potential are of equal height. For $\kappa = \kappa_c$, the energies of both ground states are degenerate. This procedure is repeated for different $U > U_c$. As U approaches U_c , the lattice spacing goes to zero and the continuum limit is reached. The critical point, which corresponds to a second order phase transition, is characterized by a vanishing curvature of the effective potential.

The discretization of the model is usually constructed by a partial bosonization of the four-fermi term using the Hubbard-Stratonovich transformation. This formulation will be used to compare to the fermion-bag approach and is therefore given here in short. Starting from the continuum action (4.26), we derive the discretized form for the $N_f=1$ model

$$S = \sum_{x,y} \bar{\psi}_x M_{xy} \psi_y - U \sum_x (\bar{\psi}_x \psi_x)^2, \quad (4.30)$$

where M_{xy} corresponds to either the SLAC derivative or the Wilson derivative. We introduce an additional scalar field σ such that

$$\int d\sigma e^{\sigma \bar{\psi}\psi + \frac{1}{4U} \sigma^2} \propto e^{-U(\bar{\psi}\psi)^2} \quad (4.31)$$

and the partition sum takes the form:

$$\begin{aligned}
 Z &= \int \prod_z d\sigma_z d\bar{\psi}_z d\psi_z \exp \left\{ - \sum_{x,y} \bar{\psi}_x \underbrace{(M_{xy} + \sigma_x \delta_{xy})}_{\equiv M_{xy}(\sigma)} \psi_y + \frac{1}{4U} \sum_x \sigma_x^2 \right\}, \\
 &= \int \prod_z d\sigma_z \det M(\sigma) \exp \left\{ - \frac{1}{4U} \sum_x \sigma_x^2 \right\}, \\
 &= \int \prod_z d\sigma_z \exp \{ -S_{\text{eff}} \}
 \end{aligned} \tag{4.32}$$

with the effective action

$$S_{\text{eff}} = \frac{1}{4U} \sum_x \sigma_x^2 - \log \det M(\sigma). \tag{4.33}$$

The determinant of the fermion-matrix may obtain a complex phase,

$$\det M(\sigma) = e^{i\phi(\sigma)} |\det M(\sigma)|. \tag{4.34}$$

We simulate the phase-quenched ensemble using a global Hybrid Monte Carlo algorithm and include the phase by a reweighting procedure. The partition sum of the phase quenched ensemble reads

$$Z_\phi = \int \prod_z d\sigma_z \exp \left\{ - \frac{1}{4U} \sum_x \sigma_x^2 - \log |\det M(\sigma)| \right\} \tag{4.35}$$

and expectation values are defined as

$$\langle \mathcal{O} \rangle = \frac{\langle \mathcal{O} e^{i\phi} \rangle_\phi}{\langle e^{i\phi} \rangle_\phi} = \frac{Z_\phi^{-1} \int \prod_z d\sigma_z \mathcal{O} e^{i\phi} \exp \left\{ - \frac{1}{4U} \sum_x \sigma_x^2 - \log |\det M(\sigma)| \right\}}{Z_\phi^{-1} \int \prod_z d\sigma_z e^{i\phi} \exp \left\{ - \frac{1}{4U} \sum_x \sigma_x^2 - \log |\det M(\sigma)| \right\}}. \tag{4.36}$$

We will now analyze the basic features of the model using the non-local SLAC derivative.

4.4.2 SLAC fermions

On a one-dimensional lattice of length L , the SLAC derivative reads

$$\partial_{xy}^{SLAC} = \begin{cases} 0 & \text{for } x = y \\ \frac{\pi}{L}(-1)^{x-y} \sin^{-1}\left(\frac{\pi}{La}(x-y)\right) & \text{for } x \neq y \end{cases}. \quad (4.37)$$

This is generalized to arbitrary dimensions in a straightforward way and leads to a non-local derivative. Boundary conditions for different lattice directions μ are set by the respective lattice side length L_μ :

$$\text{for } L_\mu \quad \begin{cases} \text{even} & \text{anti-periodic boundary conditions,} \\ \text{odd} & \text{periodic boundary conditions.} \end{cases}$$

The SLAC derivative was shown to be very efficient for supersymmetric quantum mechanics [123, 166], Wess-Zumino models [100] and the supersymmetric nonlinear sigma model [25]. It shows only small lattice artifacts and does not break the parity symmetry explicitly, which eliminates the need to fine tune the fermion mass parameter. Our aim is to use this derivative to reveal the basic features of the model in order to obtain a guideline for the discussion of the fermion-bag method.

The parity condensate is an order parameter for the parity symmetry. It is zero in the symmetric phase and becomes nonzero in the broken phase. However, in lattice simulations we work with finite volumes and the tunneling probability between the two ground states is hence nonzero. This leads to a vanishing of the parity condensate even in the broken phase. As a rough guideline for the phase boundary, we use the four-fermi term

$$\langle F \rangle = \frac{1}{2V} \sum_x (\langle \text{tr } M_{xx}^{-1} \text{tr } M_{xx}^{-1} \rangle - \langle \text{tr } M_{xx}^{-1} M_{xx}^{-1} \rangle), \quad (4.38)$$

which is shown in figure 31 (left panel). For small coupling, it takes small values. Going to larger coupling, $\langle F \rangle$ increases until a plateau is reached. Furthermore, it is not diminished if the lattice size is increased. The (phase-quenched) constraint

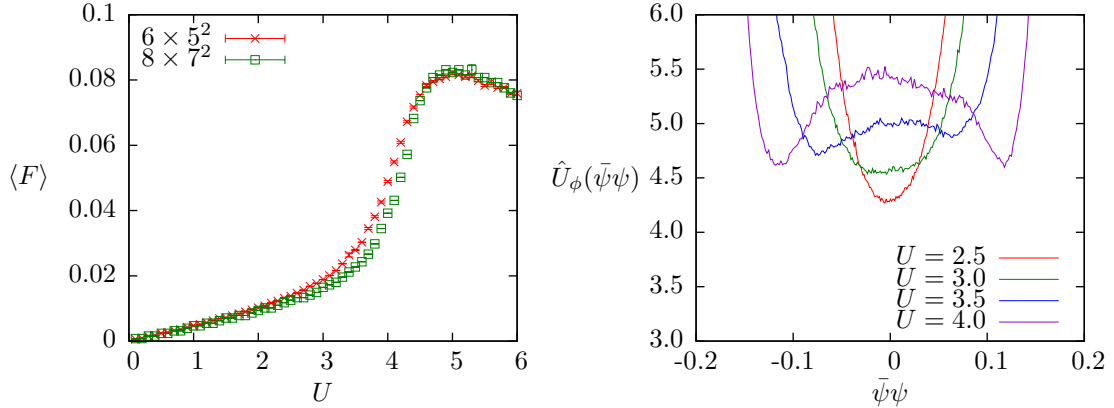


Figure 31: The average of the four-fermi term (left panel) shows a transition that is more pronounced for larger lattices. This is reflected by the constraint effective potential of the condensate for different couplings U on the 8×7^2 lattice (right panel). In particular, the two minima which correspond to the ground states in the broken phase are clearly visible for large coupling.

effective potential of the parity condensate

$$\hat{U}_\phi(\bar{\psi}\psi) = -\log \rho_\phi(\bar{\psi}\psi) \quad (4.39)$$

is depicted in figure 31 (right panel). The probability density ρ_ϕ is given by

$$\rho_\phi(X) = Z_\phi^{-1} \int \prod_z d\sigma_z \delta(X - \bar{\psi}\psi) e^{-S_{\text{eff}}}. \quad (4.40)$$

For small coupling, we find that $\hat{U}_\phi(\bar{\psi}\psi)$ shows only a single minimum. Going to larger coupling, the effective potential broadens and two minima appear, which correspond to the ground states of the model. This behaviour is compatible with a second order phase transition.

From previous studies we expect the appearance of massless fermions at the critical point. Therefore, we have computed the fermionic masses m_{Fa} from the scalar correlator $\langle \mathcal{O}(x) \bar{\mathcal{O}}(y) \rangle$ with source $\bar{\mathcal{O}}(y) = \bar{\psi}_y \psi_y$ and sink $\mathcal{O}(x) = \bar{\psi}_x \psi_x$. Thereby, a projection onto one of the ground states in the broken phase is not needed. We find that the masses are well above the cutoff value for the 6×5^2 lattice (see figure 32, left panel). For the larger 8×7^2 lattice however, the masses decrease significantly towards the critical point and a massless continuum limit

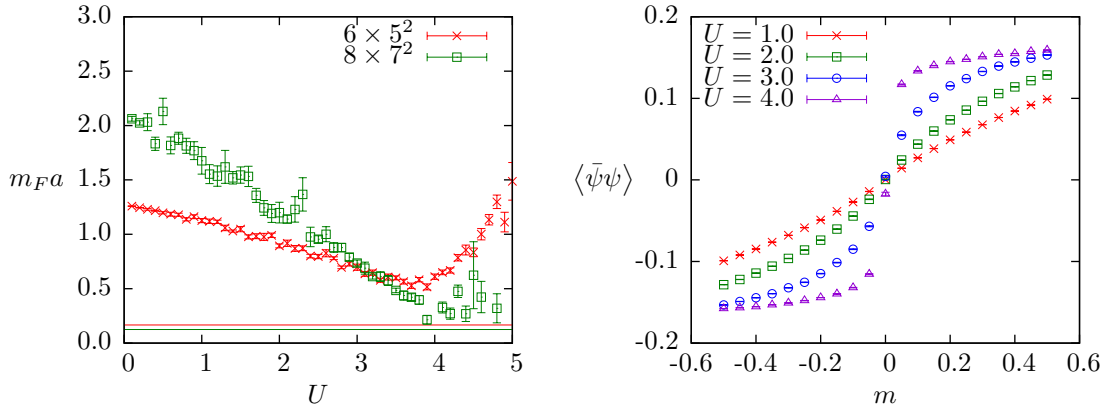


Figure 32: The left panel shows the fermionic mass in dependence of the coupling. The solid lines depict the cutoff mass. In the right panel, we show the behaviour of the parity condensate to a variation of the fermion mass parameter m on the 8×7^2 lattice. For small coupling, a continuous transition is observed, but for large coupling the behaviour grows more steep. In the infinite volume limit we expect a jump which corresponds to a first order phase transition.

is plausible.

We can disfavor one of the minima by the introduction of a fermionic mass term $m\bar{\psi}\psi$, which breaks the parity symmetry explicitly and rises the respective ground state energy. In figure 32 (right panel), we depict the parity condensate for different values of the fermion mass parameter m . We find a smooth transition between positive and negative values of the condensate, but it becomes increasingly steep for large coupling. The fermionic mass behaves like a relevant operator. If it is zero and $U = U_c$, then the theory flows along the critical line. If it is chosen nonzero however, a display of the amplification property of the RG flow is provided. For a finite lattice, fluctuations are integrated out only until a lower cutoff: the behaviour is continuous. In the infinite volume limit however, the lower cutoff goes to zero and even a small deviation leads to a large change of the macroscopic physics: the steep behaviour becomes a jump. It is a signal of a first order phase transition.

The applicability of the MCMC method is challenged by the complex weight of the effective action (4.33). In figure 33 (left panel) we show the average absolute phase $\langle |\phi| \rangle$ of the fermion determinant in dependence of the coupling constant. We see that phase fluctuations are particularly pronounced in the vicinity of the critical point. Furthermore, $\langle |\phi| \rangle$ increases significantly with the lattice volume.

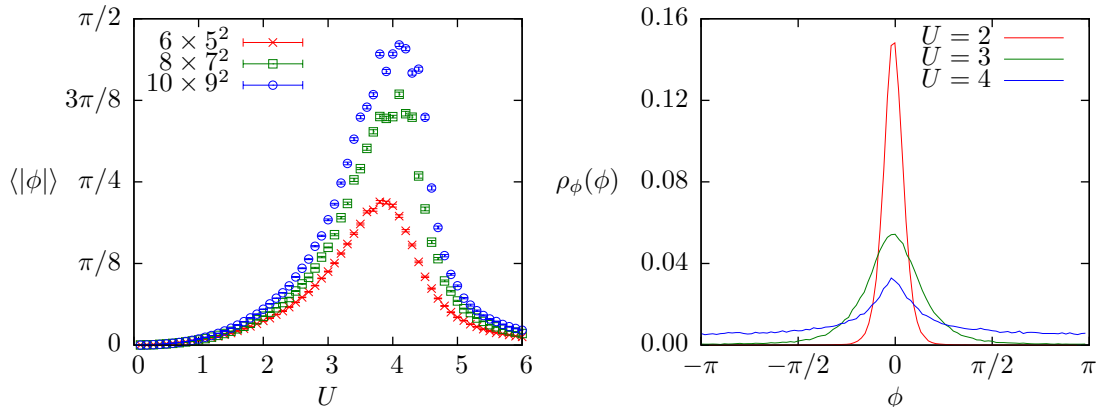


Figure 33: Shown is the average absolute phase of the fermion determinant for various lattice sizes depending on the coupling (left panel) and the distribution $\rho_\phi(\phi)$ of the phase on the 8×7^2 lattice for different couplings (right panel).

The distribution $\rho_\phi(\phi)$ (see figure 33, right panel),

$$\rho_\phi(X) = Z_\phi^{-1} \int \prod_z d\sigma_z \delta(X - \phi) e^{-S_{\text{eff}}} \quad (4.41)$$

is sharp for small coupling $U = 2.0$ but becomes flat for $U = 4.0$, revealing that the phase varies strongly. Since we need to simulate the model in the vicinity of the critical point in order to compute the continuum limit, this is a severe problem. It is clear that simulations at large volumes will be extremely hard to perform.

In the next chapter, we will evaluate the fluctuations of the phase in the fermion-bag approach and discuss whether this formulation is able to provide a solution to the complex phase problem.

4.4.3 The fermion-bag method

The idea of the fermion-bag formulation in the one-flavor Gross-Neveu model is analogous to the supersymmetric nonlinear Sigma model. However, integrating out the Dirac fermions yields the determinant of the fermion-matrix instead of the Pfaffian. We start with the action (4.30) and note that again the four-fermi

interaction does not mix degrees of freedom at different lattice sites,

$$\sum_x (\bar{\psi}_x \psi_x)^2 = 2 \sum_x \bar{\psi}_x^0 \psi_x^0 \bar{\psi}_x^1 \psi_x^1. \quad (4.42)$$

We expand the interaction and due to the Grassmann nature of the fermions only the constant and linear term survive. The partition sum reads:

$$Z = \int \prod_z d\bar{\psi}_z d\psi_z (1 + 2U \bar{\psi}_z^0 \psi_z^0 \bar{\psi}_z^1 \psi_z^1) \exp\left\{-\sum_{u,v} \bar{\psi}_u M_{uv} \psi_v\right\}. \quad (4.43)$$

Here, u and v collect the $2V$ lattice and spinor indices to allow for a shorter notation. The interaction term is rewritten by the introduction of a new field variable $k_x \in \{0, 1\}$ for every lattice site x , which will later be interpreted as the fermion-bag,

$$Z = \sum_{\{k\}} \int \prod_z d\bar{\psi}_z d\psi_z (2U \bar{\psi}_z^0 \psi_z^0 \bar{\psi}_z^1 \psi_z^1)^{k_z} \prod_u \left(1 - \bar{\psi}_u \sum_v M_{uv} \psi_v\right). \quad (4.44)$$

For a fixed configuration of $\{k\}$, only one term survives the integration. It includes every fermionic degree of freedom exactly once:

$$Z = \sum_{\{k\}} \int \prod_z d\bar{\psi}_z^1 d\psi_z^1 d\bar{\psi}_z^0 d\psi_z^0 (2U)^{k_z} \sum_{v_0, v_1, \dots} \psi_{v_0}^0 \bar{\psi}_0^0 \dots \psi_x^0 \bar{\psi}_x^0 \psi_x^1 \bar{\psi}_x^1 \dots \psi_{v_{V-1}}^1 \bar{\psi}_{V-1}^1 M_{0v_0} \dots 1 \dots M_{0v_{V-1}}. \quad (4.45)$$

The lattice sites z with $k_z = 0$ provide an element of M to the product, whereas the lattice sites with $k_z = 1$ do not contribute. For the product to be nonzero, all v_i must be different from each other. Since a reordering of the indices is antisymmetric, we identify the product as the determinant of the fermion-matrix

M with rows and columns corresponding to lattice sites with $k_z = 1$ dropped:

$$Z = \sum_{\{k\}} \int \prod_z d\bar{\psi}_z^1 d\psi_z^1 d\bar{\psi}_z^0 d\psi_z^0 (2U)^{k_z} \psi_0^0 \bar{\psi}_0^0 \dots \psi_x^0 \bar{\psi}_x^0 \psi_x^1 \bar{\psi}_x^1 \dots \psi_{V-1}^1 \bar{\psi}_{V-1}^1 \underbrace{\sum_{v_0, v_1, \dots} \epsilon_{v_0 v_1 \dots} M_{0v_0} \dots 1 \dots M_{0v_{V-1}}}_{\det M[k]}. \quad (4.46)$$

The final form for the partition sum is hence

$$Z = \sum_{\{k\}} \prod_x (2U)^{k_x} \det M[k]. \quad (4.47)$$

We will use the ultra-local Wilson derivative from equation (3.30) to discretize the fermionic action and the determinant $\det M[k]$ can thus be written as a product of the determinants for the fermion-bags B_i ,

$$\det M[k] = \prod_i \det M[B_i]. \quad (4.48)$$

Analogous to the previous chapter, it is possible to construct a dual fermion-bag formulation which nets the duality relation

$$\det M[k] = \det M \det M^{-1}[k], \quad (4.49)$$

where $M^{-1}[k]$ is the matrix of propagators between the lattice sites x with $k_x = 1$. Of course, the matrix of propagators is in general not sparse and the determinant does not break up into separate factors for each fermion-bag.

Ignoring the fermionic contribution of the determinant, the quenched partition sum for the fermion-bags takes an analogous form to the equation (4.15) and we can expect a similar behaviour to figure 24. In particular, we again want to address the question whether the fermion-bag formulation shows an improved scaling behaviour of the simulation time when one approaches the continuum limit in the full model.

4.4.4 Wilson fermions

The Markov chain is constructed using a local Metropolis algorithm. Please note that in contrast to the nonlinear Sigma model, the fermion-matrix M does not depend on any bosonic or gauge degrees of freedom and the inverse thus only needs to be computed once. For the lattice sizes considered here, we will compute all matrix elements exactly. The acceptance probability for the site x takes the form

$$p_{\text{acc}} = (2U)^{1-2k_x} \frac{\prod_i \det M[B'_i]}{\prod_j \det M[B_j]} \quad (4.50)$$

for the regular fermion-bag formulation and

$$p_{\text{acc}} = (2U)^{1-2k_x} \frac{\det M^{-1}[k']}{\det M^{-1}[k]} \quad (4.51)$$

for the dual formulation. As before, it is clear that the performance of the algorithm depends crucially on the size of the fermion-bags. We start with a test run, where the bare fermion mass m is set to zero. For different coupling U , we measure the simulation time of both fermion-bag formulations, see figure 34 (left panel). We find that the runtime of the regular algorithm correlates well with

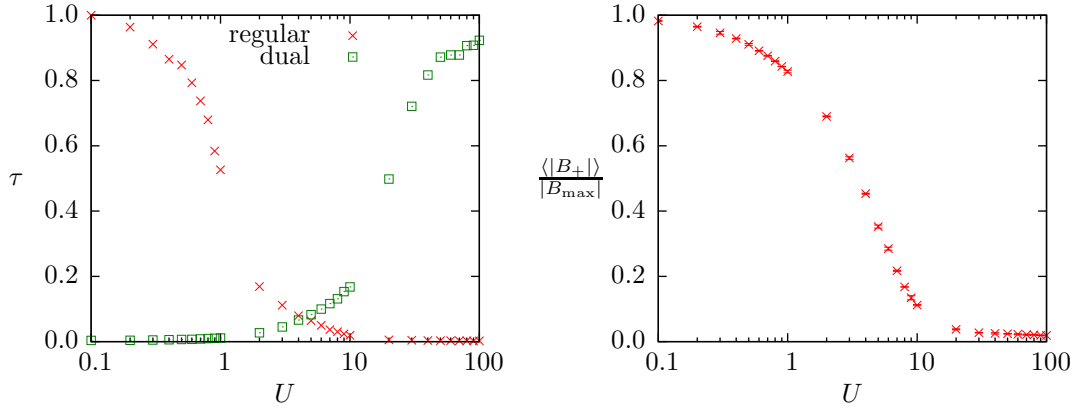


Figure 34: The simulation time τ for the regular and dual fermion-bag formulation on a 4^3 lattice is shown in the left panel. The bare fermion mass set to zero and τ is normalized such that the largest time recorded is equal to 1. The right panel shows the average size of the largest fermion-bag which correlates well with the performance of the regular method.

the size of the largest fermion-bag that is depicted in the right panel of figure

34. The plot shows superior performance of the dual updater for small couplings, where fermion-bags are large, and faster execution of the regular algorithm for large couplings and small fermion-bags.

In order to approach the continuum limit, the parameters U and κ need to be fine tuned such that the microscopic action lies on the critical line. We identify this point by a sequence of simulations starting in the broken regime $U > U_c$ and gradually lowering the coupling towards the critical point. For each coupling U , different values of the Hopping parameter κ are simulated and the critical $\kappa_c = \kappa_c(U)$ is determined from the constraint effective potential $\hat{U}_\phi(\bar{\psi}\psi)$ of the parity condensate. In figure **35** (left panel) we show the potential for three different values of κ and it is evident that the critical value corresponds to the potential with minima of equal height. In this case, both ground states have the

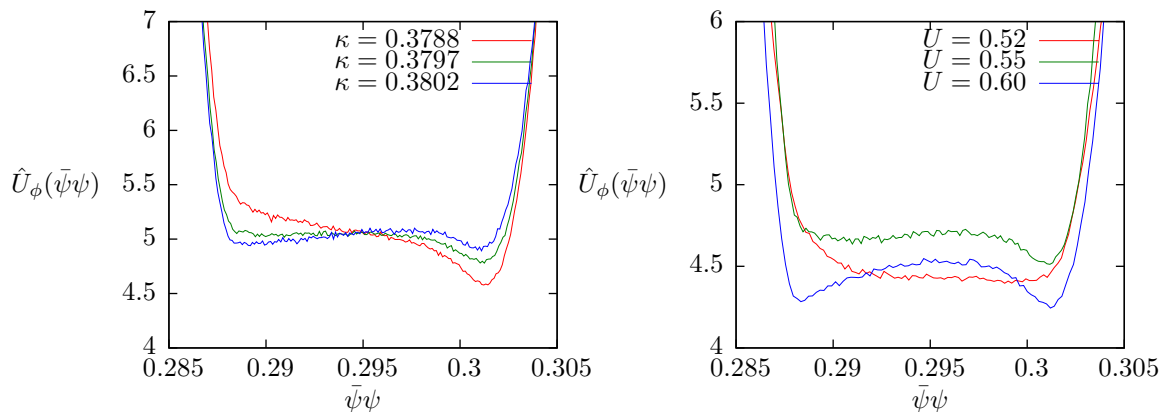


Figure 35: Shown is the constraint effective potential $\hat{U}_\phi(\bar{\psi}\psi)$ of the parity condensate in the vicinity of the critical Hopping parameter on a 24×6^2 lattice with $U = 0.55$ (left panel) and for different coupling parameters U approaching the critical point U_c on a 32×8^2 lattice (right panel).

same energy and none is favored over the other. The critical point U_c is reached if the curvature of the potential vanishes (see figure **35**, right panel). In contrast to the nonlinear Sigma model, the size of the largest bag depends only weakly on the Hopping parameter. Furthermore, we find a distinct behaviour in the vicinity of κ_c , shown in figure **36** (left panel). It is reminiscent of the parity condensate (see figure **36**, right panel). The fermion-bag method is most useful if we simulate the model either in the regime of small couplings, where the dual algorithm is fast, or in the regime of large coupling, where the regular algorithm is efficient.

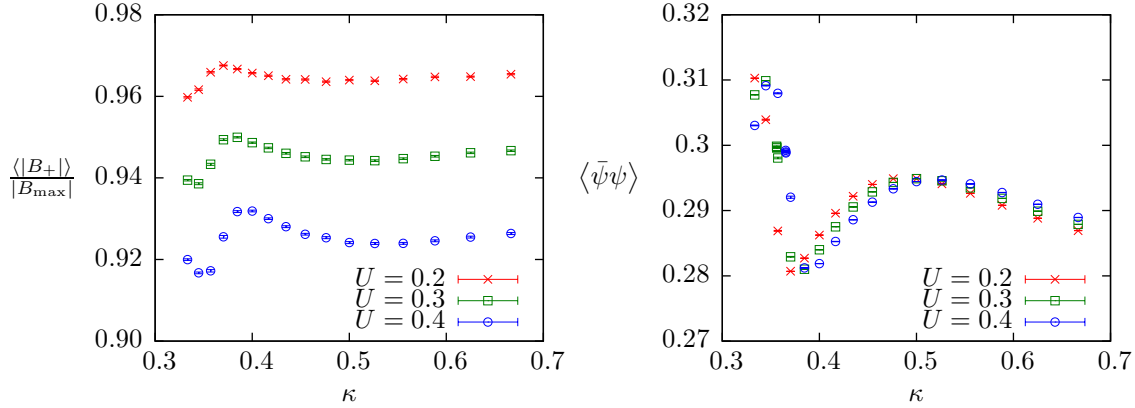


Figure 36: The size of the largest bag varies weakly with the Hopping parameter (left panel) and shows a distinct behaviour at the critical κ_c which is also visible for the parity condensate (right panel). This results were obtained on a 16×4^2 lattice.

We are most interested to simulate in the vicinity of the critical coupling. By simulating different ensembles, we find that the value for U_c depends on the lattice proportions. In the following, we choose a lattice that is larger in the temporal direction: $L_{\text{temporal}} = 4L_{\text{spatial}}$. The critical coupling is small and thus the dual updater is used for these simulations. The performance of the algorithm depends on the size of the dual bag $|B_d|$. In figure 37 we depict the average size of the largest bag (left panel) and of the dual bag (right panel) in the vicinity of the critical coupling U_c for different lattice sizes. Even though the dual fermion-bag

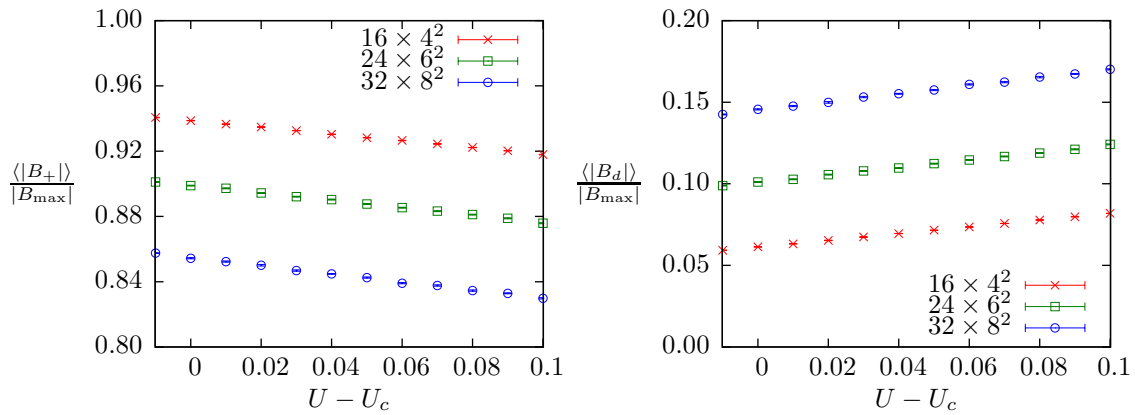


Figure 37: We show the size of the largest bag (left panel) and the size of the dual bag (right panel) in the vicinity of the critical coupling U_c for different lattice sizes.

formulation provides a massive speedup compared to the conventional method, it is evident that the dual bag grows with the lattice volume and the scaling behaviour of the simulation time is hence not improved. In contrast, the size of the largest bag decreases for larger lattices. However, based on the lattice sizes used here, it is not possible to conclude whether the regular fermion-bag algorithm is superior for large lattices.

It is still of great interest to evaluate the distribution of the phase of the fermion determinant. We compare our results for the absolute value $\langle|\phi|\rangle$ using the fermion-bag and bosonized formulation in figure 38. We find that the complex

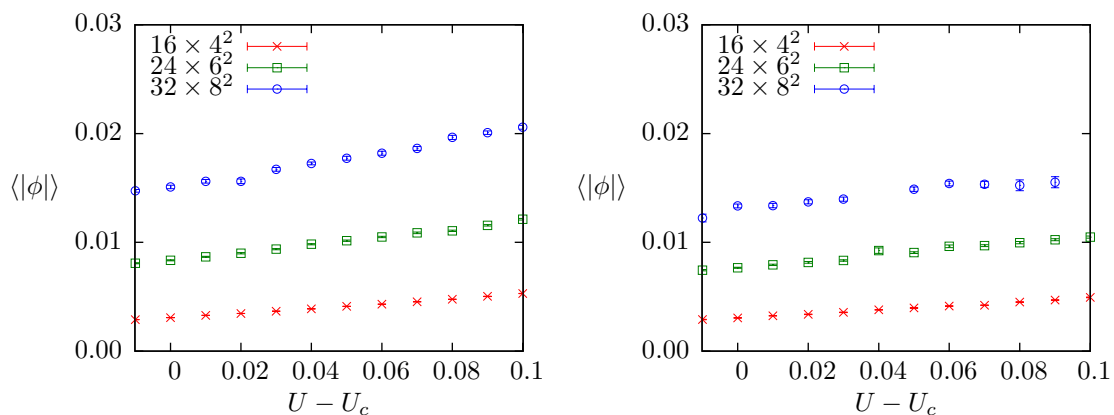


Figure 38: We show the average absolute phase of the fermion determinant for the fermion-bag method (left panel) and the auxiliary field method (right panel) for various lattice sizes.

phase problem is far less severe for the Wilson derivative compared to the SLAC results in figure 33. However, this behaviour may be analogous to the nonlinear Sigma model, where the milder sign problem is attributed to lattice artifacts. Following this reasoning, the SLAC derivative shows stronger sign fluctuations simply because the discretization is closer to the continuum limit. Indeed, going to larger lattices, it is revealed that $\langle|\phi|\rangle$ gets larger and the distribution $\rho_\phi(\phi)$, which is shown in figure 39 grows broader. The complex phase problem thus becomes worse towards the continuum limit. Comparing the fluctuations for the fermion-bag and auxiliary field method, we find that the former performs even slightly worse than the latter. However, since fluctuations of the phase are very mild, this small difference is of no practical significance.

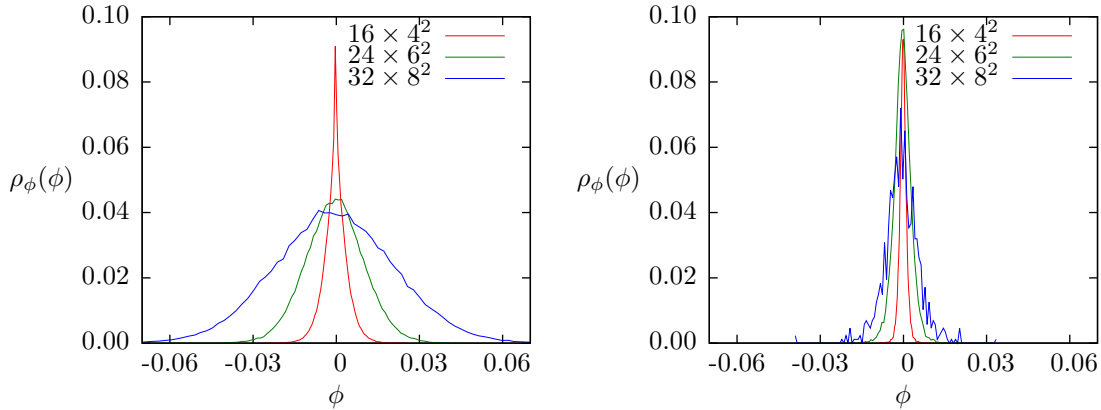


Figure 39: The distribution of the phase at U_c for different lattice sizes is depicted for the fermion-bag method (left panel) and the auxiliary field method (right panel).

4.5 Conclusion

In this chapter we have studied the applicability of the fermion-bag method to the sign problem. This problem invalidates the Monte Carlo method. In general, a treatment by brute force, using the reweighting technique, leads to an exponential increase of the simulation time towards the continuum limit and is not feasible. We have shown that this is true for the nonlinear $O(3)$ Sigma model and the one-flavor Gross-Neveu model. To assess the fermion-bag method for these models, we have investigated the scaling behaviour of the simulation time and the fluctuations of the Pfaffian sign for the former and the phase of the fermion determinant for the latter model respectively.

In the case of the supersymmetric NLSM we have demonstrated that it is possible to rewrite the partition sum using the fermion-bag method such that the resulting discretized formulation is suitable for numerical evaluation. Alas, we find that the size of the largest fermion-bag, which governs the runtime of the algorithm, scales linearly with the lattice volume. Hence we do not see an improvement of the simulation time scaling in comparison to the conventional discretization, which uses a partial bosonization of the four-fermi interaction. However, we have seen that the fluctuations of the Pfaffian sign are significantly reduced, which provides a substantial performance increase. This improvement is especially prevalent for large volumes, which are needed in order to approach the continuum limit. We thus conclude that the fermion-bag discretization is superior

to the bosonized formulation. Whereas we did not use advanced techniques to treat the fermion determinant here, i.e. using pseudofermions, there is no general problem that would prevent this. We expect that using the formulation presented in this chapter, it is possible to push lattice sizes for this model well beyond what was accessible previously. Based on these large lattice volumes, one will be able to directly ascertain the restoration of supersymmetry in the continuum limit.

For the one-flavor Gross-Neveu model, we started with a simulation using the non-local SLAC derivative in order to quickly identify the basic behaviour without the need for fine tuning. This analysis revealed massive fluctuations of the phase of the fermion determinant. Thus, we derived an alternative discretization using the fermion-bag method and Wilson fermions. Ultralocal derivatives like the Wilson derivative lead to a sparse fermion matrix, which is beneficial for algorithms that depend on fast matrix-vector multiplications, e.g. conjugate-gradient solvers. It further allows to split up the fermion determinant in the regular fermion-bag method: instead of computing the determinant of the full matrix, one computes the product of fermion-bag determinants. However, in our simulations we have found that the dual fermion-bag algorithm is substantially faster than the regular fermion-bag algorithm or the conventional approach, even though it does not profit from the ultralocal derivative. Going to larger lattices, the size of the dual bag grows and the simulation time scaling is thus not improved. It is possible that the regular algorithm becomes more efficient at a certain lattice size, but this is not covered by the simulations conducted here.

Regarding the complex phase problem, we find that it is greatly reduced for Wilson fermions, both in the fermion-bag formulation and the auxiliary field approach. The difference between both methods is very small and no practical significance can be attributed to it.

The great difference in phase fluctuations for the SLAC and Wilson fermions is quite interesting. Following an argument analogous to the nonlinear Sigma model, one could presume that the SLAC derivative provides a discretization that is far closer to the continuum limit and thus shows a stronger sign problem. This perspective is supported by the observation that the complex phase problem for Wilson fermions gets worse for larger lattices. Yet a final conclusion can not be achieved by the present study without a means to compare lattice artifacts.

5 Summary and Outlook

All quantum field theories discussed in this thesis share an important property: they interact strongly. Thus, perturbation theory is not applicable. Instead, we have used lattice techniques to study their non-perturbative behaviour. Markov Chain Monte Carlo simulation is an incredibly powerful tool to analyze quantum field theories on space-time lattices. Yet, every project portrayed here presented an unusual challenge, pushing investigations toward the boundaries of applicability of this method.

The main result of chapter [2](#) consists of the *full flow diagrams* for the non-linear $O(N)$ Sigma model in two and three dimensions. This type of information is usually not accessed in lattice simulations. Rather, one directly measures renormalized correlation functions without resorting to the full effective action Γ . Nevertheless, a combination of blockspin transformations and the demon method was shown to be able to compute the renormalization group flow. It is however unavoidable to truncate the effective action. For the asymptotically free model in two dimensions we have shown that such a truncation leads to considerable uncertainties, including the appearance of artificial fixed points. In order to complete our method, we have successfully applied a novel *optimization scheme*, based on the evaluation of correlation functions in truncated ensembles. Thereby, systematic errors were mitigated significantly. Finally, we have shown that for our best truncation, including all possible operators up to fourth order in the momenta, *asymptotic safety* is fulfilled in the three-dimensional NLSM.

In chapter [3](#) we have concerned ourselves with the supersymmetric nonlinear $O(3)$ Sigma model. Unfortunately, every discretization of space-time breaks supersymmetry and thus allows the renormalization of susy-breaking operators. If these operators diverge in the continuum limit, *supersymmetry is not restored* and the lattice method fails. Here, we have presented extensive numerical investigations of the aforementioned model. Using stereographic projection of the fields, $O(3)$ symmetry stays intact even for finite lattice spacing, whereas supersymmetry and chiral symmetry are broken. However, both are seemingly restored in the continuum limit by fine tuning of a single parameter. Thus, the lattice method yields the correct continuum limit for this theory.

Yet, one problem remains: the path integral weight is not positive. Since

Monte Carlo simulations rest on a probabilistic interpretation of the weight, their application is not straightforward. Although a loophole is given by the reweighting trick, it leads to an *exponential increase of simulation time* for large lattices. Thus, the Monte Carlo method still fails. In chapter [4](#), we have used the fermion-bag approach to treat the sign problem for the supersymmetric nonlinear O(3) Sigma model and the one-flavor irreducible Gross-Neveu model. While an improvement of simulation time scaling is not achieved for the former model, sign fluctuations are considerably reduced. We conclude that this formulation allows to study much larger lattices than previously possible. The second model suffers from a complex phase problem. Whereas SLAC fermions show wild phase fluctuations, they are greatly reduced for Wilson fermions. No further improvement is achieved by the fermion-bag method for this model.

Based on these investigations, our general conclusion is clear. Markov Chain Monte Carlo simulations and the lattice method are very well suited to study strongly-interacting quantum field theories. They provide a powerful tool that is prepared to tackle future challenges. Out of these, we emphasize two particular problems that are related to the present thesis.

Triviality of ϕ^4 theory The nonlinear O(N) Sigma model may be obtained as a limit of the linear O(N) Sigma model

$$S = \sum_x \left\{ -\kappa \sum_{\mu=0}^D (\phi_x \cdot \phi_{x+\hat{\mu}} + \phi_x \cdot \phi_{x-\hat{\mu}}) + \phi_x \cdot \phi_x + \lambda (\phi_x \cdot \phi_x - 1)^2 \right\} \quad (5.1)$$

by taking $\lambda \rightarrow \infty$. If the number of fields N is equal to 1, this limit reduces to the well-known Ising model, i.e. $\phi \in \{1, -1\}$. The action [\(5.1\)](#) is equivalent to

$$S = \sum_x \left\{ \frac{1}{2} \sum_{\mu=0}^D (\partial_\mu \hat{\phi}_x)^2 + \frac{m^2}{2} \hat{\phi}_x^2 + \frac{g}{4!} \hat{\phi}_x^4 \right\}, \quad (5.2)$$

with rescaled fields $\hat{\phi}_x = \sqrt{2\kappa} \phi_x$ and couplings $m^2 = (1 - 2\lambda)/\kappa - 2D$, $g = 6\lambda/\kappa^2$. This formulation is known as ϕ^4 theory. For $D > 4$, it was rigorously proven that it is trivial, i.e. all correlation functions are identical to the correlation functions of a generalized free field [\[167, 168\]](#). It is still an open question whether this

is true for $D = 4$ as well. In four dimensions, ϕ^4 theory possesses two phases, separated by a second-order phase transition at $\kappa_c(\lambda)$. For $\kappa < \kappa_c$ the model is in the symmetric phase and $O(N)$ symmetry is intact. For $\kappa > \kappa_c$, $O(N)$ symmetry is broken spontaneously and $N - 1$ Goldstone bosons appear. They correspond to the tangential directions of the field. Using high-temperature expansion and RG equations, triviality bounds for this model were calculated in [169–171]. It is expected that the critical exponents take their mean-field values. Furthermore, the renormalized ϕ^4 coupling vanishes in the continuum limit. However, since it vanishes only logarithmically, prohibitively large lattices are needed. Recently, one has simulated the Ising-limit using highly efficient worm algorithms [172–174]. Unfortunately, progress is still limited as one is forced to rely on a connection to perturbation theory in order to extrapolate to the continuum limit. The application of the MCRG demon method to this problem could be a very interesting prospect. Using the full flow diagram, one is able to characterize fixed points of the RG flow and the corresponding critical exponents, providing a complementary perspective to the question at hand.

Asymptotic Safety of Quantum Einstein Gravity We have demonstrated that the $D = 3$ nonlinear $O(N)$ Sigma model is asymptotically safe. Of course, this model can only be regarded as a toy model for another question of far greater physical relevance: is general relativity asymptotically safe? Several attempts to answer this question have been undertaken using functional renormalization group calculations [175–179]. Although a non-Gaussian UV fixed point was identified, one ought to treat these results with care since they are based on a truncation of the effective action. Thus, complementary results, e.g. using the MCRG demon method, are highly anticipated. However, in order to apply the latter approach, a formulation of general relativity based on numerical simulations is required. Fortunately, such a formulation exists. It is given by causal dynamical triangulation (CDT) [180, 181]⁹. Thereby, non-perturbative quantum gravity is defined as a sum over space-time geometries. Since the method is independent of any preferred background metric, a definition of a correlation length or an

⁹Incidentally, the authors of [181] note that the Wilson-Fisher fixed point of three-dimensional scalar theory is different from the presumed fixed point of general relativity since the former is an infrared fixed point. However, we have argued in chapter 2 that it actually is an ultraviolet fixed point and asymptotic safety is realized.

analogue to blockspin transformations is unclear. One approach might be to consider matter-coupled quantum gravity, where correlators of matter fields are used. In the absence of matter however, no similar formulation, e.g. of a graviton propagator, is currently available. Furthermore, while real-space renormalization group transformations exist for dynamical triangulations [182, 183], they do not respect the causal structure that is inherent in CDT. An approximation for the effective action may be obtained by a comparison to the mini-superspace approach [184]. However, in order to obtain the full flow diagram, a technique like the demon method is needed. Preliminary results suggest that the latter is indeed applicable to triangulations [185]. Thus, an implementation of the MCRG demon method seems feasible, given that a suitable RG transformation is found.

6 Bibliography

- [1] PESKIN, M. E., AND SCHROEDER, D. V. *An Introduction to quantum field theory*. Addison-Wesley, 1995.
- [2] ZEE, A. *Quantum field theory in a nutshell*. Princeton University Press, 2003.
- [3] BRAUN, J. Fermion Interactions and Universal Behavior in Strongly Interacting Theories. *J.Phys. G39* (2012), 033001, arXiv:1108.4449.
- [4] BERGES, J., TETRADIS, N., AND WETTERICH, C. Non-perturbative renormalization flow in quantum field theory and statistical physics. *Physics Reports 363*, 4-6 (2002), 223 – 386.
- [5] WIPF, A. Statistical approach to quantum field theory. *Lect. Notes Phys. 864* (2013).
- [6] MONTVAY, I., AND MÜNSTER, G. *Quantum Fields on a Lattice*. Cambridge University Press, 1994.
- [7] GATtringer, C., AND LANG, C. B. *Quantum Chromodynamics on the Lattice: An Introductory Presentation*. Springer, 2009.
- [8] BERINGER, J., ET AL. Review of Particle Physics (RPP). *Phys.Rev. D86* (2012), 010001.
- [9] AAD, G., ET AL. Observation of a new particle in the search for the Standard Model Higgs boson with the ATLAS detector at the LHC. *Phys.Lett. B716* (2012), 1–29, arXiv:1207.7214.
- [10] CHATRCHYAN, S., ET AL. Observation of a new boson at a mass of 125 GeV with the CMS experiment at the LHC. *Phys.Lett. B716* (2012), 30–61, arXiv:1207.7235.
- [11] WILCZEK, F. Origins of Mass. *Central Eur.J.Phys. 10* (2012), 1021–1037, arXiv:1206.7114.
- [12] GROSS, D., AND WILCZEK, F. Asymptotically Free Gauge Theories. 1. *Phys.Rev. D8* (1973), 3633–3652.

- [13] GROSS, D., AND WILCZEK, F. Asymptotically Free Gauge Theories. 2. *Phys.Rev. D9* (1974), 980–993.
- [14] KOLB, E. W., AND TURNER, M. S. The Early Universe. *Front.Phys. 69* (1990), 1–547.
- [15] DIRAC, P. A. M. The quantum theory of the electron. *Proceedings of the Royal Society of London. Series A 117*, 778 (1928), 610–624.
- [16] CLINE, J. M. Baryogenesis. arXiv:hep-ph/0609145.
- [17] ANDRESEN, G., ET AL. Trapped antihydrogen. *Nature 468* (2010), 673–676.
- [18] ANDRESEN, G., ET AL. Confinement of antihydrogen for 1000 seconds. *Nature Phys. 7* (2011), 558–564, arXiv:1104.4982.
- [19] CASADEI, D. Searches for cosmic antimatter. arXiv:astro-ph/0405417.
- [20] SAKHAROV, A. Violation of CP Invariance, c Asymmetry, and Baryon Asymmetry of the Universe. *Pisma Zh.Eksp.Teor.Fiz. 5* (1967), 32–35.
- [21] WU, C., AMBLER, E., HAYWARD, R., HOPPES, D., AND HUDSON, R. Experimental Test of Parity Conservation in Beta Decay. *Phys.Rev. 105* (1957), 1413–1414.
- [22] KOBAYASHI, M., AND MASKAWA, T. CP Violation in the Renormalizable Theory of Weak Interaction. *Prog.Theor.Phys. 49* (1973), 652–657.
- [23] WELLEGEHAUSEN, B. H., KÖRNER, D., AND WIPF, A. Asymptotic safety on the lattice: The Nonlinear O(N) Sigma Model. arXiv:1402.1851.
- [24] KOERNER, D., WELLEGEHAUSEN, B. H., AND WIPF, A. MCRG Flow for the nonlinear Sigma Model. In *PoS(LATTICE 2013)052*, arXiv:1310.8202.
- [25] FLORE, R., KOERNER, D., WIPF, A., AND WOZAR, C. Supersymmetric Nonlinear O(3) Sigma Model on the Lattice. *JHEP 1211* (2012), 159, arXiv:1207.6947.

- [26] WELLEGEHAUSEN, B. H., KOERNER, D., AND WIPF, A. Finetuning the continuum limit in low-dimensional supersymmetric theories. In *PoS(Lattice 2013)484*, arXiv:1310.6210.
- [27] WILSON, K., AND KOGUT, J. B. The Renormalization group and the epsilon expansion. *Phys.Rept.* *12* (1974), 75–200.
- [28] WILSON, K. G. The Renormalization Group: Critical Phenomena and the Kondo Problem. *Rev. Mod. Phys.* *47* (1975), 773.
- [29] CAMPOSTRINI, M., HASENBUSCH, M., PELISSETTO, A., ROSSI, P., AND VICARI, E. Critical exponents and equation of state of the three-dimensional Heisenberg universality class. *Phys. Rev. B* *65* (2002), 144520, arXiv:cond-mat/0110336.
- [30] STANLEY, H. E. Scaling, universality, and renormalization: Three pillars of modern critical phenomena. *Rev.Mod.Phys.* *71* (1999), S358–S366.
- [31] ZINN-JUSTIN, J. Quantum field theory and critical phenomena. *Int.Ser.Monogr.Phys.* *113* (2002), 1–1054.
- [32] HAWKING, S., AND ISRAEL, W., Eds. *General Relativity, an Einstein Centenary Survey*. Cambridge University Press, Cambridge, 1979.
- [33] NIEDERMAIER, M., AND REUTER, M. The asymptotic safety scenario in quantum gravity. *Living Reviews in Relativity* *9*, 5 (2006).
- [34] REUTER, M., AND SAUERESSIG, F. Renormalization group flow of quantum gravity in the Einstein-Hilbert truncation. *Phys. Rev. D* *65* (Feb 2002), 065016.
- [35] BENEDETTI, D., MACHADO, P. F., AND SAUERESSIG, F. Asymptotic safety in higher-derivative gravity. *Mod.Phys.Lett. A* *24* (2009), 2233–2241, arXiv:0901.2984.
- [36] LITIM, D. F. Renormalisation group and the Planck scale. *Phil.Trans.Roy.Soc.Lond. A* *369* (2011), 2759–2778, arXiv:1102.4624.

- [37] KOPIETZ, P., BARTOSCH, L., AND SCHUTZ, F. Introduction to the functional renormalization group. *Lect.Notes Phys.* 798 (2010), 1–380.
- [38] METZNER, W., SALMHOFER, M., HONERKAMP, C., MEDEN, V., AND SCHONHAMMER, K. Functional renormalization group approach to correlated fermion systems. *Rev.Mod.Phys.* 84 (2012), 299, arXiv:1105.5289.
- [39] POLONYI, J. Lectures on the functional renormalization group method. *Central Eur.J.Phys.* 1 (2003), 1–71, arXiv:hep-th/0110026.
- [40] BAGNULS, C., AND BERVILLIER, C. Exact renormalization group equations. An Introductory review. *Phys.Rept.* 348 (2001), 91, arXiv:hep-th/0002034.
- [41] LÜSCHER, M., WEISZ, P., AND WOLFF, U. A numerical method to compute the running coupling in asymptotically free theories. *Nucl. Phys. B* 359, 1 (1991), 221–243.
- [42] TRÖSTER, A. Wilson’s momentum shell renormalization group from Fourier Monte Carlo simulations. *Computer Physics Communications* 182, 9 (2011), 1837–1841.
- [43] MERMIN, N. D., AND WAGNER, H. Absence of Ferromagnetism or Antiferromagnetism in One- or Two-Dimensional Isotropic Heisenberg Models. *Phys. Rev. Lett.* 17, 22 (Nov 1966), 1133–1136.
- [44] A.M., AND POLYAKOV. Interaction of goldstone particles in two dimensions. Applications to ferromagnets and massive Yang-Mills fields. *Physics Letters B* 59, 1 (1975), 79–81.
- [45] BRÉZIN, E., AND ZINN-JUSTIN, J. Renormalization of the Nonlinear σ Model in $2 + \epsilon$ Dimensions - Application to the Heisenberg Ferromagnets. *Phys. Rev. Lett.* 36 (Mar 1976), 691–694.
- [46] BARDEEN, W. A., LEE, B. W., AND SHROCK, R. E. Phase transition in the nonlinear σ model in a $(2 + \epsilon)$ -dimensional continuum. *Phys. Rev. D* 14 (Aug 1976), 985–1005.

- [47] I.YA, AND AREF'EVA. Phase transition in the three-dimensional chiral field. *Annals of Physics* 117, 2 (1979), 393–406.
- [48] CODELLO, A., AND PERCACCI, R. Fixed points of nonlinear sigma models in $d > 2$. *Physics Letters B* 672, 3 (2009), 280–283.
- [49] FLORE, R., WIPF, A., AND ZANUSSO, O. Functional renormalization group of the non-linear sigma model and the O(N) universality class. *Phys. Rev. D* 87 (2013), 065019, arXiv:1207.4499.
- [50] BUTERA, P., AND COMI, M. n -vector spin models on the simple-cubic and the body-centered-cubic lattices: A study of the critical behavior of the susceptibility and of the correlation length by high-temperature series extended to order β^{21} . *Phys. Rev. B* 56 (Oct 1997), 8212–8240.
- [51] BOCK, W., AND KUTI, J. The shape of the renormalized trajectory in the two-dimensional O(N) non-linear sigma model. *Physics Letters B* 367, 1–4 (1996), 242–248.
- [52] ANTONENKO, S., AND SOKOLOV, A. Critical exponents for 3-D O(n) - symmetric model with $n > 3$. *Phys. Rev. E* 51 (1995), 1894–1898, arXiv:hep-th/9803264.
- [53] CHEN, K., FERRENBURG, A. M., AND LANDAU, D. Static critical behavior of three-dimensional classical Heisenberg models: A high-resolution Monte Carlo study. *Phys. Rev. B* 48 (1993), 3249–3256.
- [54] CAMPOSTRINI, M., HASENBUSCH, M., PELISSETTO, A., AND VICARI, E. The Critical exponents of the superfluid transition in He-4. *Phys. Rev. B* 74 (2006), 144506, arXiv:cond-mat/0605083.
- [55] GASSER, J., AND LEUTWYLER, H. Chiral perturbation theory to one loop. *Annals of Physics* 158 (Nov. 1984), 142–210.
- [56] KADANOFF, L. P. Scaling laws for ising models near t_c . *Physics* 2 (1966), 263.

- [57] CATTERALL, S., DEL DEBBIO, L., GIEDT, J., AND KEEGAN, L. MCRG Minimal Walking Technicolor. *Phys. Rev. D* **85** (2012), 094501, arXiv:1108.3794.
- [58] SHENKER, S. H., AND TOBOCHNIK, J. Monte Carlo renormalization-group analysis of the classical Heisenberg model in two dimensions. *Phys. Rev. B* **22** (Nov 1980), 4462–4472.
- [59] HASENFRATZ, A., HASENFRATZ, P., HELLER, U., AND KARSCH, F. Improved Monte Carlo renormalization group methods. *Physics Letters B* **140**, 1–2 (1984), 76–82.
- [60] HASENFRATZ, A., AND MARGARITIS, A. The beta function of the two-dimensional nonlinear Sigma model. *Phys.Lett. B* **148** (1984), 129–132.
- [61] MA, S.-K. Renormalization Group by Monte Carlo Methods. *Phys. Rev. Lett.* **37** (Aug 1976), 461–464.
- [62] LANG, C. On the Continuum Limit of $D = 4$ Lattice ϕ^4 Theory. *Nucl.Phys. B* **265** (1986), 630.
- [63] HIRSCH, J. E., AND SHENKER, S. H. Block-spin renormalization group in the large-N limit. *Phys. Rev. B* **27** (Feb 1983), 1736–1744.
- [64] CREUTZ, M., GOCKSCH, A., OGILVIE, M., AND OKAWA, M. Micro-canonical Renormalization Group. *Phys. Rev. Lett.* **53** (1984), 875–877.
- [65] HASENBUSCH, M., PINN, K., AND WIECZERKOWSKI, C. Canonical demon Monte Carlo renormalization group. *Nucl. Phys.Proc.Suppl.* **42** (1995), 808, arXiv:hep-lat/9411043.
- [66] WOZAR, C., KASTNER, T., WELLEGEHAUSEN, B. H., WIPF, A., AND HEINZL, T. Inverse Monte-Carlo and Demon Methods for Effective Polyakov Loop Models of SU(N)-YM. In *PoS(Lattice 2008)257*, arXiv:0808.4046.
- [67] GOTTLÖB, A., HASENBUSCH, M., AND PINN, K. Iterating block spin transformations of the O(3) nonlinear sigma model. *Phys.Rev. D* **54** (1996), 1736–1747, arXiv:hep-lat/9601014.

- [68] BOHR, O., SCHAEFER, B., AND WAMBACH, J. Renormalization group flow equations and the phase transition in $O(N)$ models. *Int.J.Mod.Phys. A16* (2001), 3823–3852, arXiv:hep-ph/0007098.
- [69] ZINN-JUSTIN, J. *Quantum Field Theory and Critical Phenomena*, 3 ed. Clarendon Press, 1996.
- [70] BALLESTEROS, H., FERNÁNDEZ, L., MARTÍN-MAYOR, V., AND SUDUPE, A. M. Finite size effects on measures of critical exponents in $d = 3$ $O(N)$ models. *Physics Letters B* 387, 1 (1996), 125–131.
- [71] PELISSETTO, A., AND VICARI, E. Critical phenomena and renormalization group theory. *Physics Reports* 368, 6 (2002), 549–727.
- [72] OKABE, Y., AND OKU, M. $1/n$ Expansion Up to Order $1/n^2$. 3. Critical Exponents γ and ν for $d=3$. *Prog.Theor.Phys.* 60 (1978), 1287–1297.
- [73] FRITZSCH, H., GELL-MANN, M., AND LEUTWYLER, H. Advantages of the Color Octet Gluon Picture. *Phys. Lett. B* 47 (1973), 365–368.
- [74] CLOWE, D., BRADAC, M., GONZALEZ, A. H., MARKEVITCH, M., RANDALL, S. W., ET AL. A direct empirical proof of the existence of dark matter. *Astrophys.J.* 648 (2006), L109–L113, arXiv:astro-ph/0608407.
- [75] ARKANI-HAMED, N., FINKBEINER, D. P., SLATYER, T. R., AND WEINER, N. A Theory of Dark Matter. *Phys. Rev. D* 79 (2009), 015014.
- [76] KIM, J. E., AND CAROSI, G. Axions and the strong CP problem. *Rev. Mod. Phys.* 82 (Mar 2010), 557–601, arXiv:0807.3125.
- [77] WEINBERG, S. Implications of Dynamical Symmetry Breaking. *Phys.Rev. D* 13 (1976), 974–996.
- [78] HILLER, G., AND SCHMALTZ, M. Solving the strong CP problem with supersymmetry. *Phys. Lett. B* 514 (2001), 263–268, arXiv:hep-ph/0105254.
- [79] HAAG, R., LOPUSZANSKI, J. T., AND SOHNIUS, M. All possible generators of supersymmetries of the S-matrix. *Nuclear Physics B* 88, 2 (1975), 257 – 274.

- [80] MARTIN, S. P. A Supersymmetry primer. arXiv:hep-ph/9709356.
- [81] SOHNIUS, M. F. Introducing supersymmetry. *Physics Reports* 128, 2-3 (1985), 39 – 204.
- [82] WEINBERG, S. *The Quantum Theory of Fields, Volume 3 Supersymmetry*. Cambridge University Press, 2000.
- [83] KALKA, H., AND SOFF, G. *Supersymmetrie*. Teubner Verlag, 1997.
- [84] NOVIKOV, V. A., SHIFMAN, M. A., VAINSHTEIN, A. I., AND ZAKHAROV, V. I. Two-Dimensional Sigma Models: Modeling Nonperturbative Effects of Quantum Chromodynamics. *Phys. Rept.* 116 (1984), 103.
- [85] DONDI, P. H., AND NICOLAI, H. Lattice supersymmetry. *Nuovo Cim. A41* (1977), 1.
- [86] MONTVAY, I. Tuning to N=2 supersymmetry in the SU(2) adjoint Higgs-Yukawa model. *Nucl. Phys. B445* (1995), 399–428, arXiv:hep-lat/9503009.
- [87] DEMMOUCHE, K. AND FARCHIONI, F. AND FERLING, A. AND MONTVAY, I. AND MUENSTER, G. AND OTHERS. Simulation of 4d N=1 supersymmetric Yang-Mills theory with Symanzik improved gauge action and stout smearing. *Eur.Phys.J. C69* (2010), 147–157, arXiv:1003.2073.
- [88] CATTERALL, S., KAPLAN, D. B., AND UNSAL, M. Exact lattice supersymmetry. *Phys. Rept.* 484 (2009), 71–130, arXiv:0903.4881.
- [89] CATTERALL, S., AND GHADAB, S. Lattice sigma models with exact supersymmetry. *JHEP* 05 (2004), 044.
- [90] CATTERALL, S., AND GHADAB, S. Twisted supersymmetric sigma model on the lattice. *JHEP* 10 (2006), 063.
- [91] WITTEN, E. A Supersymmetric Form of the Nonlinear Sigma Model in Two- Dimensions. *Phys. Rev. D16* (1977), 2991.
- [92] DI VECCHIA, P., AND FERRARA, S. Classical Solutions in Two-Dimensional Supersymmetric Field Theories. *Nucl. Phys. B130* (1977), 93.

- [93] SHANKAR, R., AND WITTEN, E. S matrix of the supersymmetric nonlinear σ model. *Phys. Rev. D* 17, 8 (1978), 2134–2143.
- [94] ALVAREZ, O. Dynamical symmetry breakdown in the supersymmetric nonlinear σ model. *Phys. Rev. D* 17, 4 (Feb 1978), 1123–1130.
- [95] EVANS, J. M., AND HOLLOWOOD, T. J. The Exact mass gap of the supersymmetric CP^{n-1} sigma model. *Phys. Lett. B* 343 (1995), 198–206, arXiv:hep-th/9409142.
- [96] EVANS, J. M., AND HOLLOWOOD, T. J. The Exact mass gap of the supersymmetric $O(N)$ sigma model. *Phys. Lett. B* 343 (1995), 189–197, arXiv:hep-th/9409141.
- [97] ZUMINO, B. Supersymmetry and Kähler Manifolds. *Phys. Lett. B* 87 (1979), 203.
- [98] HUBBARD, J. Calculation of partition functions. *Phys. Rev. Lett.* 3 (1959), 77–80.
- [99] WITTEN, E. Constraints on Supersymmetry Breaking. *Nucl. Phys. B* 202 (1982), 253.
- [100] KÄSTNER, T., BERGNER, G., UHLMANN, S., WIPF, A., AND WOZAR, C. Two-Dimensional Wess-Zumino Models at Intermediate Couplings. *Phys. Rev. D* 78 (2008), 095001.
- [101] BERGNER, G., MONTVAY, I., MÜNSTER, G., ÖZUGUREL, U. D., AND SANDBRINK, D. Towards the spectrum of low-lying particles in supersymmetric Yang-Mills theory. *JHEP* 1311 (2013), 061, arXiv:1304.2168.
- [102] DONINI, A., GUAGNELLI, M., HERNANDEZ, P., AND VLADIKAS, A. Towards N=1 Super-Yang-Mills on the lattice. *Nucl. Phys. B* 523 (1998), 529–552, arXiv:hep-lat/9710065.
- [103] MÜNSTER, G., AND STÜWE, H. The mass of the adjoint pion in N=1 supersymmetric Yang-Mills theory. arXiv:1402.6616.

- [104] CLARK, M. A., AND KENNEDY, A. D. Accelerating dynamical fermion computations using the rational hybrid Monte Carlo (RHMC) algorithm with multiple pseudofermion fields. *Phys. Rev. Lett.* *98* (2007), 051601, arXiv:hep-lat/0608015.
- [105] DEGRAND, T. A., AND ROSSI, P. Conditioning techniques for dynamical fermions. *Comput.Phys.Commun.* *60* (1990), 211–214.
- [106] OYANAGI, Y. An incomplete LDU decomposition of lattice fermions and its application to conjugate residual methods. *Comput.Phys.Commun.* *42*, 3 (1986), 333 – 343.
- [107] PEARDON, M. J. Accelerating the hybrid Monte Carlo algorithm with ILU preconditioning. arXiv:hep-lat/0011080.
- [108] TROYER, M., AND WIESE, U.-J. Computational complexity and fundamental limitations to fermionic quantum Monte Carlo simulations. *Phys.Rev.Lett.* *94* (2005), 170201, arXiv:cond-mat/0408370.
- [109] JUNG, C. Progress in Algorithms and Numerical Techniques. *to appear in PoS(Lattice 2013)*.
- [110] GUPTA, S. QCD at finite density. In *PoS(Lattice 2010)007*.
- [111] KANAYA, K. Finite Temperature QCD on the Lattice - 2010. In *PoS(Lattice 2010)012*.
- [112] DE FORCRAND, P. Simulating QCD at finite density. In *PoS(Lattice 2009)010*, arXiv:1005.0539.
- [113] LEVKOVA, L. QCD at Nonzero Temperature and Density. In *PoS(Lattice 2011)011*.
- [114] MUKHERJEE, S. Fluctuations, correlations: from lattice QCD to heavy ion collisions. In *PoS(Lattice 2011)013*.
- [115] SCHAEFER, S. Status and challenges of simulations with dynamical fermions. In *PoS(Lattice 2012)001*, arXiv:1211.5069.

- [116] AARTS, G. Developments in lattice QCD for matter at high temperature and density. arXiv:1312.0968.
- [117] HENELIUS, P., AND SANDVIK, A. W. The sign problem in Monte Carlo simulations of frustrated quantum spin systems. arXiv:cond-mat/0001351.
- [118] NYFELER, M., JIANG, F.-J., KÄMPFER, F., AND WIESE, U.-J. Nested cluster algorithm for frustrated quantum antiferromagnets. *Phys. Rev. Lett.* *100* (Jun 2008), 247206.
- [119] CUBROVIC, M., ZAAENEN, J., AND SCHALM, K. String Theory, Quantum Phase Transitions and the Emergent Fermi-Liquid. *Science* *325* (2009), 439–444, arXiv:0904.1993.
- [120] SANDVIK, A. W. Ground states of a frustrated quantum spin chain with long-range interactions. *Phys. Rev. Lett.* *104* (Mar 2010), 137204.
- [121] BECCARIA, M., CAMPOSTRINI, M., AND FEO, A. Supersymmetry breaking in two-dimensions: The Lattice $N = 1$ Wess-Zumino model. *Phys.Rev. D69* (2004), 095010, arXiv:hep-lat/0402007.
- [122] KANAMORI, I., SUGINO, F., AND SUZUKI, H. Observing dynamical supersymmetry breaking with euclidean lattice simulations. *Prog.Theor.Phys.* *119* (2008), 797–827, arXiv:0711.2132.
- [123] WOZAR, C., AND WIPF, A. Supersymmetry Breaking in Low Dimensional Models. *Annals Phys.* *327* (2012), 774–807, arXiv:1107.3324.
- [124] BAUMGARTNER, D., STEINHAEUER, K., AND WENGER, U. Supersymmetry breaking on the lattice: the $N=1$ Wess-Zumino model. In *PoS(Lattice 2011)253*, arXiv:1111.6042.
- [125] BAUMGARTNER, D., STEINHAEUER, K., AND WENGER, U. Spontaneous supersymmetry breaking in the 2d $N=1$ Wess-Zumino model. In *PoS(Lattice 2012)043*, arXiv:1311.5089.
- [126] HART, A., LAINE, M., AND PHILIPSEN, O. Testing imaginary vs. real chemical potential in finite-temperature QCD. *Physics Letters B* *505*, 1-4 (2001), 141 – 148.

- [127] DE FORCRAND, P., AND PHILIPSEN, O. The QCD phase diagram for small densities from imaginary chemical potential. *Nuclear Physics B* 642, 1-2 (2002), 290–306.
- [128] ALFORD, M., KAPUSTIN, A., AND WILCZEK, F. Imaginary chemical potential and finite fermion density on the lattice. *Phys. Rev. D* 59 (Jan 1999), 054502.
- [129] ALLTON, C. R., EJIRI, S., HANDS, S. J., KACZMAREK, O., KARSCH, F., LAERMANN, E., SCHMIDT, C., AND SCORZATO, L. QCD thermal phase transition in the presence of a small chemical potential. *Phys. Rev. D* 66 (Oct 2002), 074507.
- [130] DANZER, J., AND GATTRINGER, C. Properties of canonical determinants and a test of fugacity expansion for finite density lattice QCD with Wilson fermions. *Phys.Rev. D* 86 (2012), 014502, arXiv:1204.1020.
- [131] GREENSITE, J., AND SPLITTORFF, K. Mean field theory of effective spin models as a baryon fugacity expansion. *Phys.Rev. D* 86 (2012), 074501, arXiv:1206.1159.
- [132] GRÜNWARD, E., MERCADO, Y. D., AND GATTRINGER, C. Taylor- and fugacity expansion for the effective $Z(3)$ spin model of QCD at finite density. arXiv:1403.2086.
- [133] FODOR, Z., AND KATZ, S. A New method to study lattice QCD at finite temperature and chemical potential. *Phys.Lett. B* 534 (2002), 87–92, arXiv:hep-lat/0104001.
- [134] BARBOUR, I. M., MORRISON, S. E., KLEPFISH, E. G., KOGUT, J. B., AND LOMBARDO, M.-P. Results on finite density QCD. *Nucl.Phys.Proc.Suppl.* 60A (1998), 220–234, arXiv:hep-lat/9705042.
- [135] FODOR, Z., KATZ, S. D., AND SCHMIDT, C. The Density of states method at non-zero chemical potential. *JHEP* 0703 (2007), 121, arXiv:hep-lat/0701022.

- [136] LANGFELD, K., LUCINI, B., AND RAGO, A. The density of states in gauge theories. *Phys.Rev.Lett.* 109 (2012), 111601, arXiv:1204.3243.
- [137] GREENSITE, J., MYERS, J. C., AND SPLITTORFF, K. The density in the density of states method. *JHEP* 1310 (2013), 192, arXiv:1308.6712.
- [138] EJIRI, S. Phase structure of hot dense QCD by a histogram method. *Eur.Phys.J. A*49 (2013), 86, arXiv:1306.0295.
- [139] SIXTY, D. Simulating full QCD at nonzero density using the complex Langevin equation. *Phys.Lett.* B729 (2014), 108–111, arXiv:1307.7748.
- [140] AARTS, G., GIUDICE, P., SEILER, E., AND SEILER, E. Localised distributions and criteria for correctness in complex Langevin dynamics. *Annals Phys.* 337 (2013), 238–260, arXiv:1306.3075.
- [141] AARTS, G., BONGIOVANNI, L., SEILER, E., SIXTY, D., AND STAMATESCU, I.-O. Controlling complex Langevin dynamics at finite density. *Eur.Phys.J. A*49 (2013), 89, arXiv:1303.6425.
- [142] WENGER, U. Efficient simulation of relativistic fermions via vertex models. *Phys.Rev.* D80 (2009), 071503, arXiv:0812.3565.
- [143] WOLFF, U. Simulating the All-Order Hopping Expansion. II. Wilson Fermions. *Nucl.Phys.* B814 (2009), 549–572, arXiv:0812.0677.
- [144] MERCADO, Y. D., EVERTZ, H. G., AND GATTRINGER, C. The QCD phase diagram according to the center group. *Phys.Rev.Lett.* 106 (2011), 222001, arXiv:1102.3096.
- [145] MERCADO, Y. D., AND GATTRINGER, C. Monte Carlo simulation of the SU(3) spin model with chemical potential in a flux representation. *Nucl.Phys.* B862 (2012), 737–750, arXiv:1204.6074.
- [146] GATTRINGER, C. New developments for dual methods in lattice field theory at non-zero density. In *PoS(Lattice 2013)002*, arXiv:1401.7788.
- [147] CHANDRASEKHARAN, S. A New computational approach to lattice quantum field theories. In *PoS(Lattice 2008)003*, arXiv:0810.2419.

- [148] CHANDRASEKHARAN, S. The Fermion bag approach to lattice field theories. *Phys.Rev. D82* (2010), 025007, arXiv:0910.5736.
- [149] CHANDRASEKHARAN, S., AND LI, A. Fermion bags, duality and the three dimensional massless lattice Thirring model. *Phys.Rev.Lett. 108* (2012), 140404, arXiv:1111.7204.
- [150] CHANDRASEKHARAN, S., AND LI, A. The generalized fermion-bag approach. In *PoS(Lattice 2011)058*, arXiv:1111.5276.
- [151] CHANDRASEKHARAN, S., AND LI, A. Fermion bag solutions to some sign problems in four-fermion field theories. *Phys.Rev. D85* (2012), 091502, arXiv:1202.6572.
- [152] CHANDRASEKHARAN, S. Fermion Bag Approach to Fermion Sign Problems. *Eur.Phys.J. A49* (2013), 90, arXiv:1304.4900.
- [153] CHANDRASEKHARAN, S., AND LI, A. Fermion bag approach to the sign problem in strongly coupled lattice QED with Wilson fermions. *JHEP 1101* (2011), 018, arXiv:1008.5146.
- [154] CHANDRASEKHARAN, S., AND WIESE, U.-J. Partition Functions of Strongly Correlated Electron Systems as 'Fermionants'. arXiv:1108.2461.
- [155] MERTENS, S., AND MOORE, C. The complexity of the fermionant, and immanants of constant width. arXiv:1110.1821.
- [156] CHANDRASEKHARAN, S., AND LI, A. Quantum critical behavior in three dimensional lattice Gross-Neveu models. *Phys.Rev. D88* (2013), 021701, arXiv:1304.7761.
- [157] STEINHAUER, K., AND WENGER, U. Loop formulation of the supersymmetric nonlinear O(N) sigma model. In *PoS(Lattice 2013)092*, arXiv:1311.5403.
- [158] SCHAMBACH, M. Graphische Entwicklung der Zustandssumme für das supersymmetrische nichtlineare σ -Modell in (1+0) D. Bachelor thesis, 2013.

- [159] RUBTSOV, A. N., SAVKIN, V. V., AND LICHTENSTEIN, A. I. Continuous-time quantum monte carlo method for fermions. *Phys. Rev. B* 72 (Jul 2005), 035122.
- [160] GULL, E., MILLIS, A. J., LICHTENSTEIN, A. I., RUBTSOV, A. N., TROYER, M., AND WERNER, P. Continuous-time monte carlo methods for quantum impurity models. *Rev. Mod. Phys.* 83 (May 2011), 349–404.
- [161] WIMMER, M. Algorithm 923: Efficient Numerical Computation of the Pfaffian for Dense and Banded Skew-Symmetric Matrices. *ACM Trans. Math. Softw.* 38, 4 (2012), 30:1–30:17.
- [162] THRON, C., DONG, S., LIU, K., AND YING, H. Pade - Z(2) estimator of determinants. *Phys.Rev. D* 57 (1998), 1642–1653, arXiv:hep-lat/9707001.
- [163] REISZ, T. The Gross-Neveu model and QCDs chiral phase transition. arXiv:hep-lat/9712017.
- [164] REISZ, T. Chiral symmetry restoration of QCD and the Gross-Neveu model. *Nucl.Phys.Proc.Suppl.* 73 (1999), 462–464, arXiv:hep-lat/9808025.
- [165] HOFLING, F., NOWAK, C., AND WETTERICH, C. Phase transition and critical behavior of the D = 3 Gross-Neveu model. *Phys.Rev. B* 66 (2002), 205111, arXiv:cond-mat/0203588.
- [166] BERGNER, G., KÄSTNER, T., UHLMANN, S., AND WIPF, A. Low-dimensional supersymmetric lattice models. *Annals Phys.* 323 (2008), 946–988, arXiv:0705.2212.
- [167] AIZENMAN, M. Proof of the Triviality of ϕ^4 in D-Dimensions Field Theory and Some Mean Field Features of Ising Models for $D > 4$. *Phys.Rev.Lett.* 47 (1981), 1–4.
- [168] FROHLICH, J. On the Triviality of Lambda ϕ^4 in D-Dimensions Theories and the Approach to the Critical Point in $D \geq$ Four-Dimensions. *Nucl.Phys. B* 200 (1982), 281–296.

- [169] LUSCHER, M., AND WEISZ, P. Scaling Laws and Triviality Bounds in the Lattice ϕ^4 Theory. 1. One Component Model in the Symmetric Phase. *Nucl.Phys. B290* (1987), 25.
- [170] LUSCHER, M., AND WEISZ, P. Scaling Laws and Triviality Bounds in the Lattice ϕ^4 Theory. 2. One Component Model in the Phase with Spontaneous Symmetry Breaking. *Nucl.Phys. B295* (1988), 65.
- [171] LUSCHER, M., AND WEISZ, P. Scaling Laws and Triviality Bounds in the Lattice ϕ^4 Theory. 3. N Component Model. *Nucl.Phys. B318* (1989), 705.
- [172] WOLFF, U. Precision check on triviality of ϕ^4 theory by a new simulation method. *Phys.Rev. D79* (2009), 105002, arXiv:0902.3100.
- [173] WEISZ, P., AND WOLFF, U. Triviality of ϕ_4^4 theory: small volume expansion and new data. *Nucl.Phys. B846* (2011), 316–337, arXiv:1012.0404.
- [174] HOGERVORST, M., AND WOLFF, U. Finite size scaling and triviality of ϕ^4 theory on an antiperiodic torus. *Nucl.Phys. B855* (2012), 885–900, arXiv:1109.6186.
- [175] REUTER, M. Nonperturbative evolution equation for quantum gravity. *Phys.Rev. D57* (1998), 971–985, arXiv:hep-th/9605030.
- [176] CODELLO, A., PERCACCI, R., AND RAHMEDE, C. Investigating the Ultraviolet Properties of Gravity with a Wilsonian Renormalization Group Equation. *Annals Phys. 324* (2009), 414–469, arXiv:0805.2909.
- [177] RECHENBERGER, S., AND SAUERESSIG, F. A functional renormalization group equation for foliated spacetimes. *JHEP 1303* (2013), 010, arXiv:1212.5114.
- [178] EICHHORN, A., AND KOSLOWSKI, T. Continuum limit in matrix models for quantum gravity from the Functional Renormalization Group. *Phys.Rev. D88* (2013), 084016, arXiv:1309.1690.
- [179] CHRISTIANSEN, N., KNORR, B., PAWLOWSKI, J. M., AND RODIGAST, A. Global Flows in Quantum Gravity. arXiv:1403.1232.

- [180] AMBJORN, J., GOERLICH, A., JURKIEWICZ, J., AND LOLL, R. Quantum Gravity via Causal Dynamical Triangulations. arXiv:1302.2173.
- [181] AMBJORN, J., GOERLICH, A., JURKIEWICZ, J., AND LOLL, R. Nonperturbative Quantum Gravity. *Phys.Rept.* 519 (2012), 127–210, arXiv:1203.3591.
- [182] THORLEIFSSON, G., AND CATTERALL, S. A real space renormalization group for random surfaces. *Nucl.Phys. B461* (1996), 350–370, arXiv:hep-lat/9510003.
- [183] HENSON, J. Coarse graining dynamical triangulations: A New scheme. *Class.Quant.Grav.* 26 (2009), 175019, arXiv:0907.5602.
- [184] AMBJORN, J., GIZBERT-STUDNICKI, J., GOERLICH, A., AND JURKIEWICZ, J. The effective action in 4-dim CDT. The transfer matrix approach. arXiv:1403.5940.
- [185] WELLEGEHAUSEN, B. personal communication.

A Basic symbols and conventions

Throughout this thesis, natural units $\hbar = 1 = c$ are used. Unless noted otherwise, x and y are used to indicate lattice points. For spinor components, α and β are typically used and field species or “flavors” are denoted with i and j . Einstein’s summation convention

$$\phi_x \phi_x \equiv \sum_x \phi_x \phi_x \quad (\text{A.1})$$

is implied, i.e. indices that appear twice are to be summed over. For space-time indices μ, ν the summation rule

$$\partial_\mu \partial^\mu = \eta_{\mu\nu} \partial_\mu \partial_\nu \equiv \sum_{\mu=0}^{D-1} \sum_{\nu=0}^{D-1} \eta_{\mu\nu} \partial_\mu \partial_\nu, \quad (\text{A.2})$$

with space-time dimension D holds. The metric tensor $\eta_{\mu\nu}$ has signature $(-1, 1, \dots)$ (“mostly plus”) in Minkowski space and $(1, 1, \dots)$ in Euclidean space. Thus, the line element in Minkowski space reads

$$ds^2 = \eta_{\mu\nu} dx^\mu dx^\nu = -(dx^0)^2 + \sum_{a=1}^{D-1} (dx^a)^2. \quad (\text{A.3})$$

Kronecker’s delta is defined by

$$\delta_{xy} = \begin{cases} 1 & \text{if } x = y \\ 0 & \text{else.} \end{cases} \quad (\text{A.4})$$

Regarding Fourier-transformation, a convention is chosen where the normalization is split. For a Lebesgue-integrable function $f(x)$, the Fourier transform $\mathcal{F}(f)$ is given by

$$\mathcal{F}(f) \equiv f(p) = \frac{1}{\sqrt{2\pi}} \int_{-\infty}^{\infty} dx e^{-ipx} f(x) \quad (\text{A.5})$$

and the inverse transform corresponds to

$$\mathcal{F}^{-1}(\mathcal{F}(f)) \equiv f(x) = \frac{1}{\sqrt{2\pi}} \int_{-\infty}^{\infty} dp e^{ipx} f(p). \quad (\text{A.6})$$

As usual,

$$\int_{-\infty}^{\infty} dx e^{-ipx} = 2\pi\delta(p) \quad (\text{A.7})$$

holds, where $\delta(x - y)$ is Dirac's delta.

B Lattice definitions

Quantum field theories in D dimensions are discretized on a hypercubic space-time lattice

$$\left\{ x = (x_0, \dots, x_{D-1}) \mid x_\mu = an_\mu, n_\mu = 0, \dots, L_\mu - 1 \right\}, \quad (\text{B.1})$$

with lattice spacing a and lengths L_μ . The total number of points is $V = \prod_\mu L_\mu$ and the physical volume thus $\prod_\mu aL_\mu$. A vector with norm 1,

$$\hat{\mu}_\nu = \begin{cases} 1 & \text{if } \mu = \nu \\ 0 & \text{else,} \end{cases} \quad (\text{B.2})$$

is used to denote directions on the lattice. After discretization, fields are defined on lattice sites: $\phi(x) \rightarrow \phi_x$. Using generalized boundary conditions

$$\phi_{x+a\hat{\mu}L_\mu} = e^{2\pi i\theta_\mu} \phi_x, \quad (\text{B.3})$$

the special cases of periodic (anti-periodic) boundary conditions is obtained for $\theta_\mu = 0$ ($\theta_\mu = \frac{1}{2}$). The momenta are constrained to the Brillouin zone of the dual lattice

$$\left\{ p = (p_0, \dots, p_{D-1}) \mid p_\mu = \frac{2\pi}{aL_\mu}(k_\mu + \theta_\mu), k_\mu = -\frac{L_\mu}{2} - 1, \dots, \frac{L_\mu}{2} \right\} \quad (\text{B.4})$$

and the plain waves $e^{ip_\mu n_\mu a}$ conform to [\(B.3\)](#). It is evident that

$$\frac{1}{L_\mu} \sum_{k_\mu=-L_\mu/2+1}^{L_\mu/2} e^{i\frac{2\pi}{L_\mu} k_\mu n_\mu} = \frac{1}{L_\mu} \sum_{k_\mu=0}^{L_\mu-1} e^{i\frac{2\pi}{L_\mu} k_\mu n_\mu} = \delta_{n_\mu 0}, \quad (\text{B.5})$$

such that lattice Fourier transformation may be defined by

$$\mathcal{F}(\phi) = \frac{1}{\sqrt{V}} \sum_x \phi_x e^{-ipx} \quad (\text{B.6})$$

$$\mathcal{F}^{-1}(\mathcal{F}(\phi)) \equiv \phi_x = \frac{1}{\sqrt{V}} \sum_p f_p e^{ipx}. \quad (\text{B.7})$$

Danksagung

Zuvorderst bedanke ich mich bei Prof. Andreas Wipf, der mir die Möglichkeit zur Promotion gegeben hat. Während dieser Zeit war er nicht nur wichtiger und stets erreichbarer Ansprechpartner, sondern hat persönlich zur freundlichen und stimulierenden Atmosphäre am TPI beigetragen.

Weiterhin danke ich dem Graduiertenkolleg 1523 für die finanzielle Absicherung während meiner Promotionszeit. Ein besonders herzlicher Dank gebührt unserer Sekretärin Lisann Schmidt, die jederzeit mit Rat und Tat auszuweichen weiß. Auch für die Möglichkeit zur Präsentation meiner Arbeit auf verschiedenen Konferenzen bin ich dankbar.

Meine Gedanken und Ideen, Forschungsblockaden und Fehlschläge konnte ich mit einigen Kollegen teilen. Ich danke Christian Wozar und Franziska Synatschke-Czerwonka, von denen ich viel gelernt habe. Raphael Flore, Marco Schäfer, Felix Karbstein und Luca Zambelli danke ich für zahlreiche Gespräche und Diskussionen abseits der Physik. Gleiches gilt für Björn Wellegehausen und Marianne Heilmann, denen ich darüber hinaus für die Korrektur von Teilen dieser Arbeit danke.

Ohne die Fürsorge und Unterstützung meiner Eltern und Großeltern hätte diese Arbeit nie zustande kommen können. Dem Vertrauen meiner Familie kann ich mir stets sicher sein. Schlussendlich bedanke ich mich bei meiner Partnerin Anita, deren Liebe und Lebensfreude mein größtes Glück bedeutet.

Ehrenwörtliche Erklärung

Ich erkläre hiermit ehrenwörtlich, dass ich die vorliegende Arbeit selbständig, ohne unzulässige Hilfe Dritter und ohne Benutzung anderer als der angegebenen Hilfsmittel und Literatur angefertigt habe. Die aus anderen Quellen direkt oder indirekt übernommenen Daten und Konzepte sind unter Angabe der Quelle gekennzeichnet. Auch die Ergebnisse, die in Zusammenarbeit mit den Mitgliedern des Lehrstuhles für Quantenfeldtheorie in Jena und anderen Kooperationen entstanden sind, sind in der Arbeit entsprechend benannt.

Weitere Personen waren an der inhaltlich-materiellen Erstellung der vorliegenden Arbeit nicht beteiligt. Insbesondere habe ich hierfür nicht die entgeltliche Hilfe von Vermittlungs- bzw. Beratungsdiensten (Promotionsberater oder andere Personen) in Anspruch genommen. Niemand hat von mir unmittelbar oder mittelbar geldwerte Leistungen für Arbeiten erhalten, die im Zusammenhang mit dem Inhalt der vorgelegten Dissertation stehen.

Die Arbeit wurde bisher weder im In- noch im Ausland in gleicher oder ähnlicher Form einer anderen Prüfungsbehörde vorgelegt.

Die geltende Promotionsordnung der Physikalisch-Astronomischen Fakultät ist mir bekannt.

Ich versichere ehrenwörtlich, dass ich nach bestem Wissen die reine Wahrheit gesagt und nichts verschwiegen habe.

Weimar, 28.08.2014